Tal Ben-Gera

Compressive Membrane Action in Immersed Tubes

A Finite Element Study

TU Delft

ARCADIS

Compressive Membrane Action in Immersed Tubes

A Finite Element Study

By

Tal Ben-Gera

in partial fulfilment of the requirements for the degree of

Master of Science

in Structural Engineering: Concrete Structures

at the Delft University of Technology,

to be defended publicly on Monday September 20, 2019 at 15:00

Supervisor:	ir. Coen van der Vliet,	Arcadis
Thesis committee:	Prof.dr.ir. J.G. Rots,	TU Delft
	Dr. ir. C.B.M. Blom,	TU Delft
	Ir. J.M. Houben	TU Delft

תזכור שהחיים הם כמו רכיבה על אופניים, אם קל לך – סימן שאתה בירידה. ולכן כמו שאתה מבין – קשה זה לא תמיד רע.

אבא

Acknowledgements

My special thanks go to my supervisor at Arcadis – Coen van der Vliet, whose supervision and mentorship made this research possible. Coen's systematic and deliberate approach to problem solving is a quality I hope to emulate in my future career as a structural engineer.

To my main university supervisor, Kees Blom, not only for suggesting this topic as a thesis opportunity, but for his help and guidance along the way.

I also wish to thank committee member Jan Rots, whose expertise in the finite element method proved valuable for the execution of this thesis project.

To my friends here in Delft: Our mutual away-from-home experiences have brought us close together through the years. The difficulties and joys of living abroad are shared best with those experiencing it as well. Though I have been living in a country far from home with a different language and culture for three years, our homemade dinners, late-night Fiesta Macumbas, and trips around the Netherlands made this experience one that I will remember fondly for the rest of my life.

To my family: spending the last three years in the Netherlands meant missing birthdays, holidays, and weekly yom-shishi dinners. While modern luxuries like voice and video calling made the 5,800 km that separate Delft and Closter seem walkable in a single afternoon, nothing can replace a Saturday morning bike ride with Abba, a home-cooked meal from Imma, or catching up with my brothers over a cup of tea on the family deck. My experience here in Delft wouldn't have been possible with your love and support.

Lastly a special thanks to Aoife, whose optimism and cheery attitude always put a smile on my face.

This thesis marks the culmination of three years of graduate studies in Delft. The journey has been exciting, arduous, and ultimately rewarding. I emerge not only with an engineering degree from a prestigious university, but also with a refined perspective on what it means to follow your dreams, persevere through difficult times, and most importantly – to believe in yourself.

Table of Contents

1 Abstract

Tunnels are vital to the interconnectivity of the Dutch transportation network. Many underwater tunnels in the Netherlands are built using the immersed tube method, where precast concrete segments of the immersed tube are individually sunk into place and connected to form the tunnel structure. As in any tunnel, immersed tubes suffer from the risk of fire occurring within a tube, which may cause significant damage to the concrete, compromising the safety of the tunnel's occupants and forcing expensive repair projects (1). The safety of tunnels and the avoidance of fire situations have been the focus of substantial research interest in recent decades due to several notable examples of tunnel fire disasters, including most notably in Mont Blanc tunnel [discussed further in Section 2.3.1].

In 2000, a concrete mixture called 'ROK' is adopted as the concrete of choice in Dutch tunnels. This concrete mixture is determined to be resistant to spalling and is therefore an ideal mixture for tunnel design. Tunnels built after the study conducted in 2000 were built primarily with ROK concrete since it was not required to prove the mixture's insensitivity to spalling prior to building. As a result, several tunnels were built in the Netherlands using ROK concrete without fire testing. In 2014, doubts were raised as to the non-spalling property of the ROK mixture. A fire test attempting to confirm the results of the Rijkswaterstaat experiment showed significant spalling in the ROK concrete (2). This result raised concerns over the safety of tunnels built using ROK concrete. Since then, significant emphasis has been placed on retrofitting existing concrete lined tunnels susceptible to spalling, most notably through the use of non-spalling classified concrete, increased concrete cover, polypropylene (PP) fiber infused concrete mixtures, and the use of fire-protective insulation for concrete mixtures at risk of spalling (3).

An additional strategy to mitigate spalling risks is by discovering a hidden safety margin in the concrete tunnel called compressive membrane action (CMA). CMA is a phenomenon whereby significant deformations and cracking in concrete sections lead to the development of arch-shaped internal compressive struts. The requirements for CMA to occur in a structure are elaborated upon in Section 2.2. It is hypothesized that immersed tubes in the Netherlands meet the requirements for CMA. It is therefore necessary to investigate the boundary conditions necessary for the development of CMA and to explore the hidden margin of safety it can provide.

Recent developments in computing technology have paved the way for finite element methods to be utilized by engineers to develop and verify designs (4). Therefore, in this thesis project, a finite element model is developed to investigate both the potential for CMA to provide additional strength in case of fire in an immersed tube and the factors which may limit its development. Several boundary conditions are considered and isolated in order to determine the conditions necessary for the development of CMA. These boundary conditions are adjusted in order to quantify the contribution of each boundary condition. While decisions regarding the safety of tunnels in the Netherlands should not be made based on the results of this thesis project alone, this thesis offers an insight into the benefits of CMA and in which specific tunnels it can be expected.

2 Literature Review

2.1 Spalling

Spalling is a phenomenon whereby medium to large sections of concrete are suddenly and violently detached from the main structure during its service life. It has been well established that the heating of confined concrete to high temperatures cause internal stresses which result in spalling. Due to its sudden and violent nature, spalling quickly degrades concrete structures. Its presence indicates an imminent threat of collapse.

Spalling is a difficult phenomenon to study given that reproducing spalling failures in a laboratory is a nearly impossible task. Over the last century, several theories have been developed by researchers to explain the cause of spalling. A summary of the spalling mechanisms is summarized below (5).

2.1.1 Moisture Clog Theory

The moisture clog theory postulates that when concrete is heated, steam pressure in pores rises to the surface. Moisture is therefore drawn into the inner colder regions, causing the steam to condense. The fully saturated layer of concrete forms and restricts the further movement of steam. High pressures develop at the interface between the moisture and the clog and the steam moving inwards. Spalling occurs when this pressure exceeds the tensile strength of the concrete (6). The mechanism is shown in Figure 1.

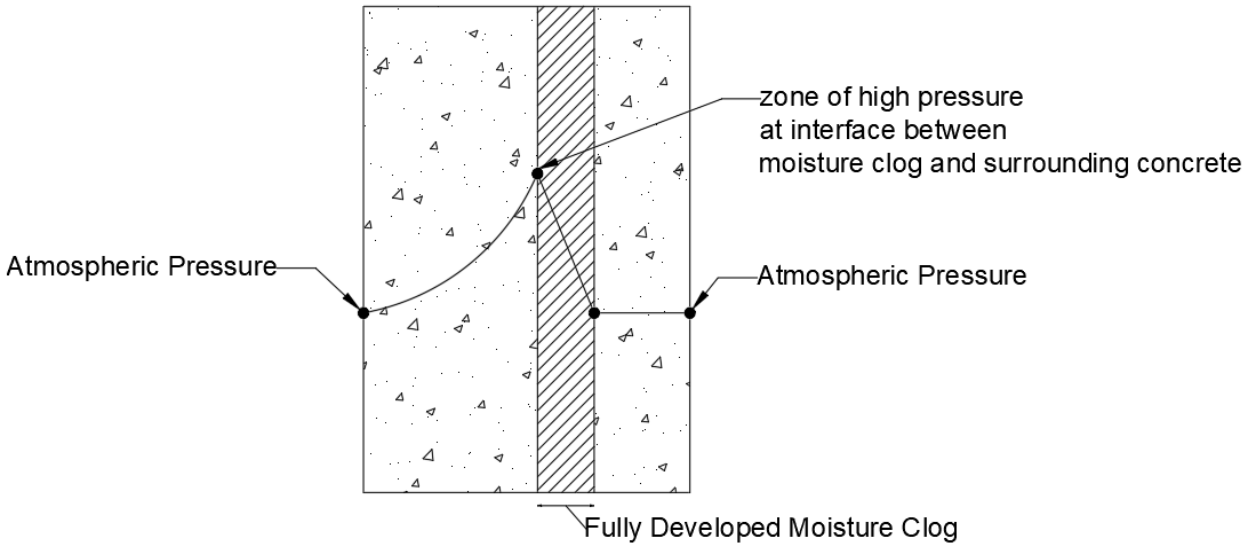

Figure 1: The mechanism of spalling according to the moisture clog theory

2.1.2 Hydraulic Spalling Theory

According to the hydraulic spalling theory, spalling is caused by the hydraulic fracture of a saturated pore (7). The thermal expansion of water is higher than the available volume in the pore. If 32% of a pore is filled with water before the fire, the water will fully saturate the pore at high temperatures due to the thermal expansion of the water within the pore.

2.1.3 Spalling due to Frictional Forces

The flow of vapor in concrete will create wall friction, will result in tensile stresses in the capillary system (8). By assuming that all moisture must be expelled during heating, the research concluded that friction is the probable cause for spalling in concrete exposed to fire.

Spalling is not yet a fully understood phenomenon. The theories described above are a selected few of several such attempts to explain its cause. Almost all theories highlight the importance of the moisture content inside of the concrete. Furthermore, as this project concerns the results of spalling rather than the cause, the specific spalling mechanism is not necessarily of importance.

To prevent the spalling behavior in concrete tunnels in the Netherlands, Ministry of Infrastructure and Water Management (Rijkswaterstaat) commissioned an experiment to determine a suitable fire curve to predict fire temperatures and an appropriate concrete mix to meet spalling requirements (9). The experiment concluded that concrete of the type ROK 1.2 is resistant to spalling for 120 minutes. Therefore, tunnels built after the conclusion of the experiment are designed using ROK 1.2 as the concrete mix of choice. ROK 1.2 is a mix which must meet the following requirements:

- Strength class C28/35 or lower (by using siliceous aggregates)
- Maximum cement content: 340 kg/m3 CEM III (blast furnace slag cement)
- Maximum compressive stress at the exposed surface: 10 N/mm²2
- Maximum compressive cube strength: 45 N/mm²2
- No filler material like fly ash, limestone powder etc.

Recent studies which attempted to confirm the findings of the experiment have raised concerns that ROK 1.2 is not fully resistant to spalling, as the original experiment suggests. An experiment conducted in 2014 tested a reinforced concrete slab exposed to fire conditions similar to the fire curves developed by Rijkswaterstaat (2). The slab is heated by a controlled flame from below and temperature sensors were placed on the reinforcement to measure the temperature over time. The sensors recorded the following data, as seen in Figure 2 below.

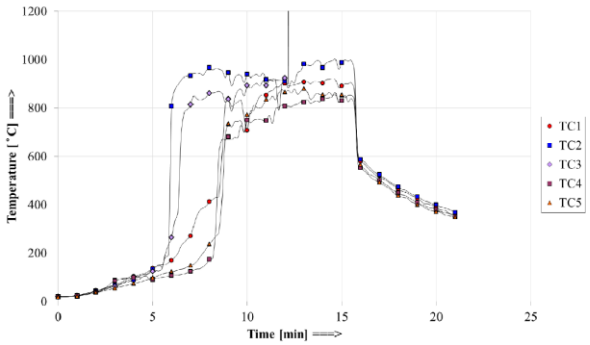

Figure 2: Temperature data from reinforcement in reinforced concrete slab exposed to fire

The slope of the temperature curve is indicative of the thermal conductivity of the material. The first five minutes show a gradual rise in temperature, which suggests that the concrete cover

is still intact. The sudden increase in slope in the temperature at 7 minutes in Figure 2 demonstrates that the concrete cover is compromised, thus directly exposing the reinforcement to the flames.

The differences in the slopes of the lines are indicative of the differences in thermal conductivity of concrete and steel. It can therefore be concluded that certain sections of concrete began spalling at 7 minutes, which falls far short of the 120-minute threshold set by Rijkswaterstaat. This experiment raised major concerns regarding the fire safety of currently used concrete tunnels in the Netherlands and is the main driving force behind this thesis project.

2.1.4 Spalling Rate

To effectively model the spalled concrete, it is necessary to obtain information regarding the spalling rate. The spalling rate is the measure of the depth of concrete which is lost to spalling per unit time. In 2017, a comprehensive study was conducted by Efectis in the Netherlands to assess the fire safety of concrete tunnels. As part of the study, the researchers measured the concrete temperature at different depths by making use of the Rijkswaterstaat fire curve and a concrete mix similar to that of ROK 1.2. Furthermore, the concrete was compressed to a stress of 10mpa to simulate the working condition of the concrete in a tunnel. The results of the test are shown below in Figure 9 (10).

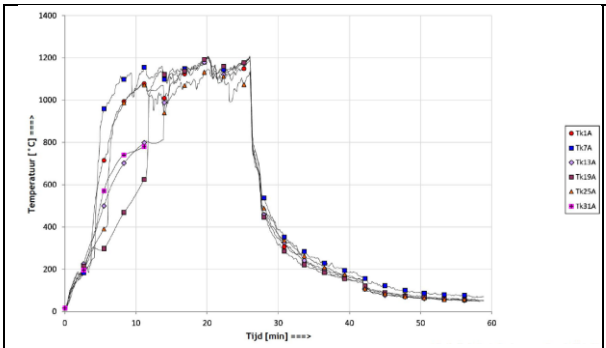

Figure 3: Temperature of concrete at surface

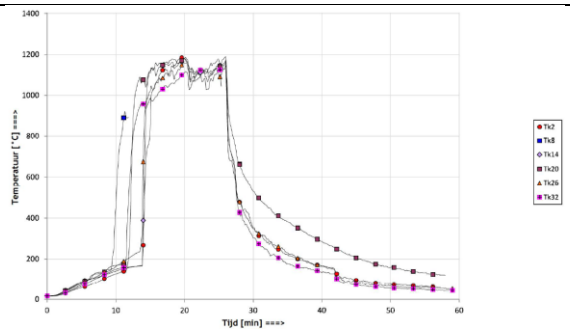

Figure 4: Temperature of concrete 35mm deep

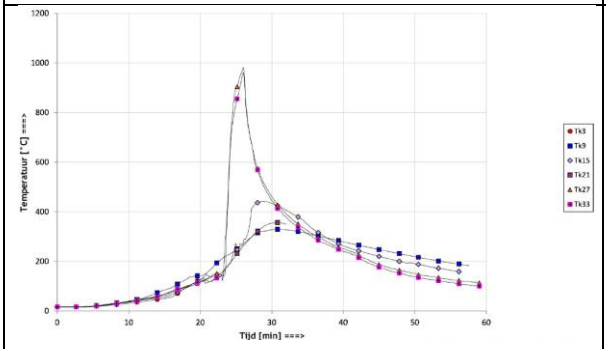

Figure 5: Temperature of concrete 70mm deep

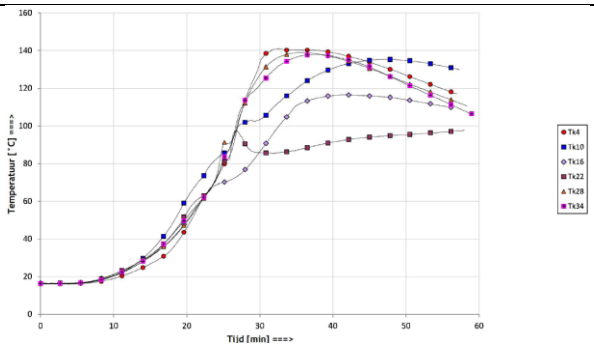

Figure 6: Temperature of concrete 100mm deep

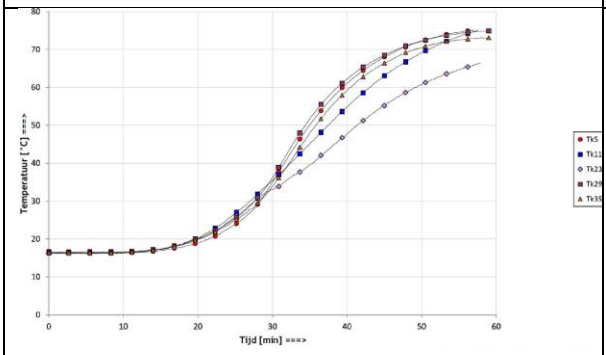

Figure 7: Concrete temperature 150mm deep

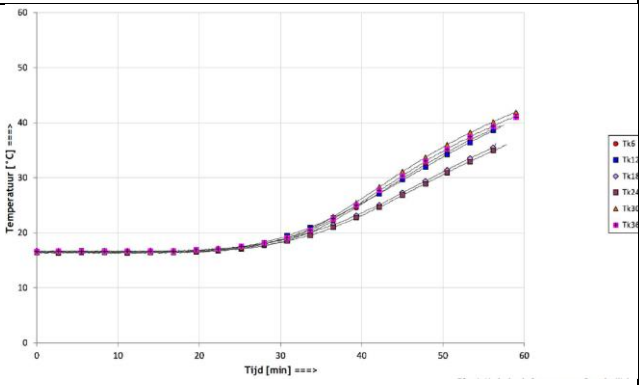

Figure 8: Concrete temperature 200mm deep

Figure 9: Spalling depth of concrete using Rijkswaterstaat fire curve (10)

Figure 3 through Figure 8 show a variation of the concrete temperature over time. As the depth of the thermocouples increases, it is evident that the temperature increase occurs later and later. By assuming a temperature at which concrete spalls (200°C), these values are used in the thesis project to estimate the spalling profile of the tunnel structure. Furthermore, the Efectis experiments indicated a spalling depth of 70 mm in 12 min, starting after 10 min. This research data is used as part of the parametric study to study the tunnel structure at different time intervals during the fire.

2.2 CMA

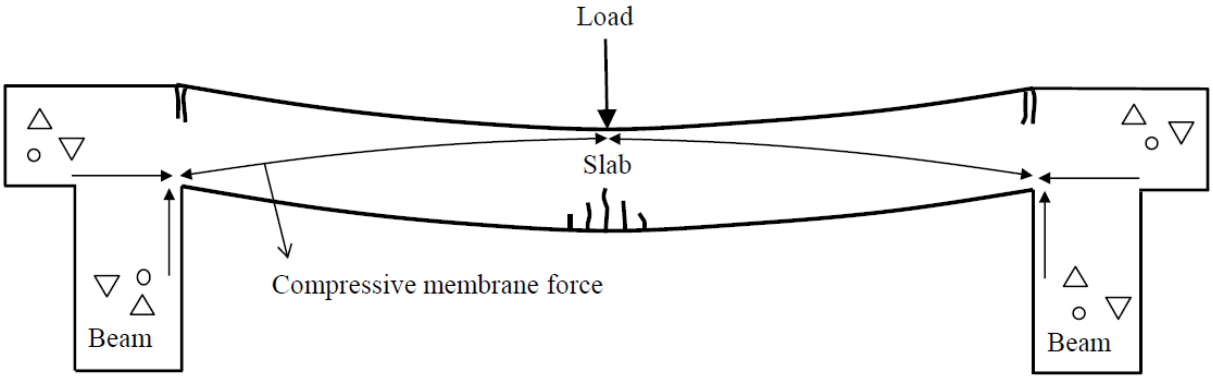

Figure 10: Mechanical representation of CMA

Compressive Membrane Action (CMA) is a term commonly used to describe the arching of internal forces in a laterally restrained concrete structure subjected to substantial loading and deformation. The phenomenon garnered substantial academic interest after destructive load tests were performed on a dental hospital in South Africa. During the load tests, failure was observed at levels 3-4 times what was predicted using traditional mechanics. It was concluded by the research team that CMA was the cause for the increased strength of the slab (11). CMA increases strength capacity by redistributing the external loads from above into arch shaped internal forces in the upper slab of the tunnel. Though the research team identified the previously unknown phenomenon, they were unable to non-destructively quantify its effect largely due to the limited processing power of computers at the time.

Recent developments in computing power have allowed for the use of nonlinear finite element modeling (NLFEA) to further study the effects of CMA. The finite element method is a powerful design tool that allow engineers to non-destructively study the behavior of proposed or

existing structures. Several programs have been developed to assist in the modeling process. In this thesis project, DIANA is used to model the tunnel structure exposed to fire conditions. CMA can be seen in computer simulations when the compressive stresses are shown to be located at the point of load application and at the bottom section of the slab at the lateral supports, as shown in Figure 11 below.

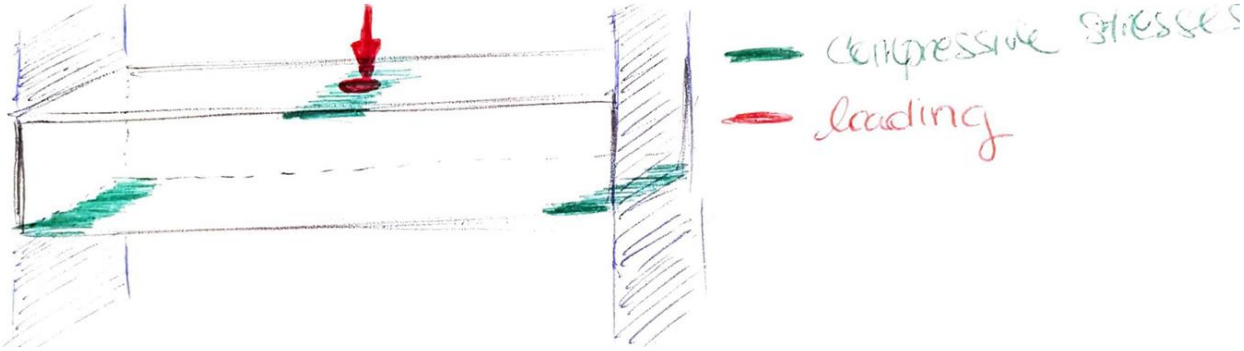

Figure 11: CMA action in laterally restrained slabs

The non-linearity associated with the influence of CMA on the tunnel structure can be divided in two categories: material and geometric. A summary of the sources of nonlinearity can be seen in Table 1.

Table 1: Summary of the sources of nonlinearity

	Material Nonlinearity	Geometric Nonlinearity
Concrete	-Cracking -Temperature effects on mechanical properties	-Changing of loads due to deflections (negligible in this project) -Rewriting of equilibrium equations due to significant deflections (negligible in this project)
Steel	-Temperature effects on mechanical properties -Yielding of steel	N/A

The geometric non-linearity arises from the necessity to rewrite the equilibrium equations due to considerable deflections caused by the reduction of the cross-section due to spalling.

Furthermore, the deflected shape changes the loading scheme, as shown in the Figure 12 below. Figure 12 represents the loading scheme since the tunnel ceiling is subjected to a semi-fluid loading in the form of soil from above. While the geometric nonlinearities associated with the concrete are important to note, their effects are negligible and will therefore not be taken into consideration in this project. On the other hand, the material non-linearity stems from concrete cracking and both steel and concrete's mechanical properties' dependency on temperature. While the geometric nonlinearity is neglected due to its minimal contribution, the material nonlinearities are expected to significantly influence the results of the model and will therefore be included.

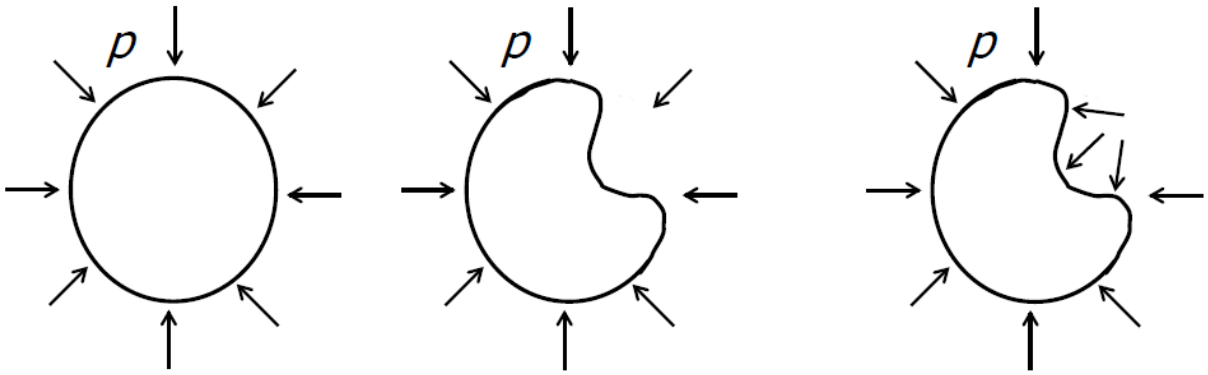

Figure 12: Hydrostatic Loading of Deformed Structure

It is important to note that structural designers do not take CMA into account when designing structures in Europe. Therefore, it can be postulated that the current strength capacity of certain European structures which meet the requirements for CMA is higher than the designed strength.

Much of the research on CMA has been done in the field of reinforced concrete slabs. It is proposed in this thesis project that the factors influencing CMA in a reinforced concrete slab are similar to those in an immersed tube structure. In reinforced concrete slabs, the main contributing factors which influence the effect of CMA are as follows (12):

- In-plane stiffness of the surrounding slab area (lateral restraint)
- Bending stiffness of the edges
- Position of the load

Amir also describes the following key aspects of CMA (12):

- CMA can only occur once cracks have developed due to the redistribution of forces
- CMA cann**ot** occur in materials that exhibit similar behaviors in tension and compression
- The presence of reinforcement is not necessary for CMA to occur in concrete slabs

In this thesis project, the Immersed Tube Method is used as the construction method of the tunnel. The tunnel contains several elements which are joined underwater to form the structure. The cross section is rectangular shaped as seen in Figure 13. This method of building tunnels is discussed further in the Section called Immersed Tube .

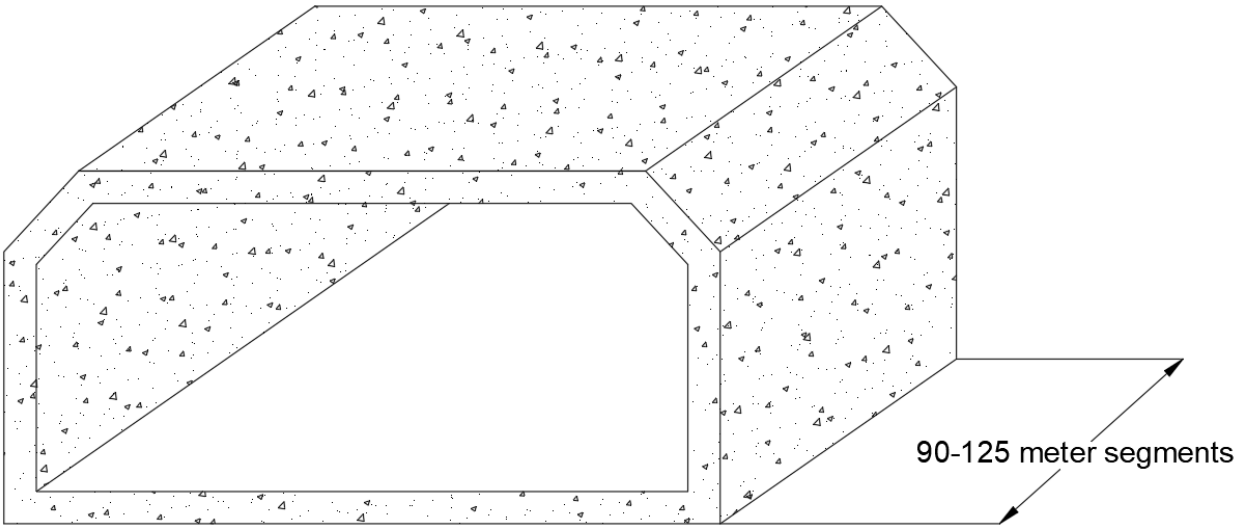

Figure 13: One section of tunnel

Since much of the literature concerning CMA concerns reinforced concrete slabs, there is limited research into the effect of CMA on concrete tunnels. Therefore, in this thesis project, the tunnel structure is investigated by modeling the tunnel ceiling as a two-way reinforced concrete slab. In the lateral direction, the sidewalls and roof slabs of the tunnel will provide the lateral stiffness. In the longitudinal direction, either concrete or a joint connecting two sections of tunnel will provide the lateral stiffness, depending on the distance of the cross-section being examined to the nearest joint. The fire situation inside the tunnel will induce spalling and imposed deformations.

2.3 Fire

2.3.1 Risk of tunnel fires

Immersed tubes are constantly at risk of fire development. One such example of the catastrophic nature of tunnel fires occurred in the Mont Blanc Tunnel in northern Italy in 1999. Figure 14 shows the aftermath of the fire, with spalling of the concrete clearly visible.

Figure 14: Result of the fire in the Mont Blanc Tunnel in 1999

While the exact source of ignition is still debated, the result was an intense fire which burned for over 53 hours, filling the enclosed volume with poisonous smoke and intense heat. 39 people were killed as a result and the tunnel was closed for 3 years during reconstruction.

Tragedies such as this one have spurred an increased awareness of the dangers of tunnel fires and enhanced safety regulations during the design process.

2.3.2 Fire Physics

A fire can be described as the rapid oxidation of a material, during which heat, light, and other byproducts are released (13). Its development relies on the presence of oxygen, fuel, and heat in what is commonly referred to as the fire triangle, shown in Figure 15.

Figure 15: Fire triangle showing the necessary parts of a fire [image source: Wikipedia]

The fuel and oxygen must react at a sufficiently high temperature, and the product of the reaction is heat. If the heat and oxygen level remain sufficiently high, the reaction can continue. Before the fuel and the oxygen combine in a reaction known as combustion, the fuel source must be converted to its gaseous form if it is in a different phase of matter. This process, known as decomposition, takes place as a result of heat. Fuels in a liquid state are decomposed much more quickly than fuels in solid form. A material is considered to be inflammable if it produces inflammable gases as a result of decomposition. Once a material is ignited, heat begins to spread.

Heat can spread through conduction, convection, and radiation, as seen in Figure 16.

- Conduction is the heat transfer through direct contact and therefore molecular collisions. When the temperatures of objects are different, their respective molecules collide with different kinetic energies. The transfer of heat will cease once the kinetic energies of both materials, and therefore their temperatures, are the same.
- Convection is the transfer of heat through bulk movements in fluids or gases. In the case of fires, the heat is carried through smoke.
- Radiation is characterized as heat transfer in the form of electromagnetic waves. As the temperature of matter rises, the electromagnetic waves which it gives off increase in frequency, thus intensifying the radiation. The sun's transfer of heat to the Earth is an example of radiation heating.

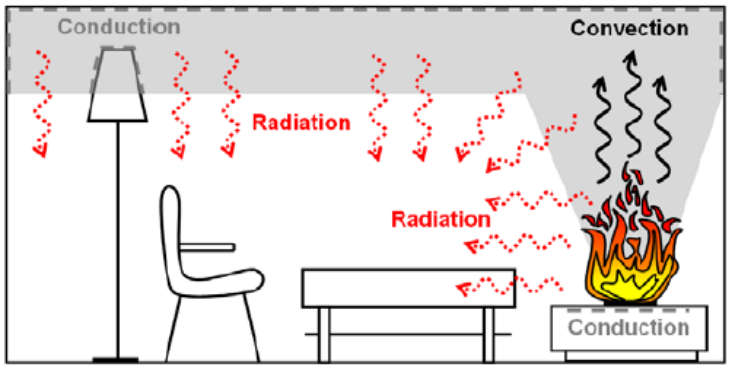

Figure 16: The three methods of heat transfer

In the case of a tunnel fire, all 3 methods of heat transfer are working to heat up the tunnel's concrete lining.

Fires can be categorized by those that achieve flashover and those that do not. Flashover occurs when combustible materials reach a sufficiently high temperature and auto-ignite. The progression of a fire that achieves flashover can be broken up into 4 distinct phases: growth phase, flashover, fire phase, and decay phase.

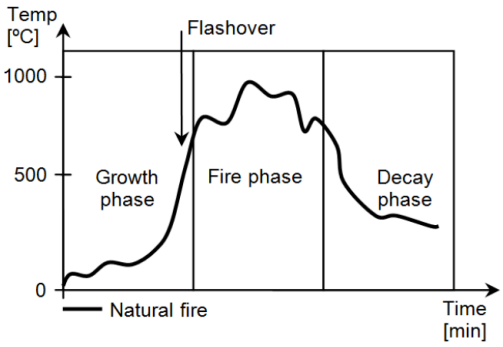

Figure 17: Development of a fire that achieves flashover

Growth phase: the growth phase begins with ignition. The ignition of a fire within a concrete rail tunnel is commonly caused by vehicle accidents, whereby fuel leakages come into contact with hot surfaces which causes ignition, or by electrical malfunctions. The growth rate depends on a variety of factors including (14):

- Materials being oxidized, since the rate of oxidation depends heavily on the material's chemistry

- Proximity of inflammable materials. Materials in close proximity allow for more rapid fire spreading
- The presence of ventilation systems
- Available oxygen
- Fire protection measures such as sprinkler systems or human action

Flashover: a flashover occurs when the temperature in the smoke layer is high enough (500-600°C) for radiation to ignite all inflammable materials directly below and within the space. Flashover is characterized by a relatively short but intense temperature rise. In a rail tunnel, it is mainly the train carriage which is at risk of flashover. The time required for flashover to occur depends heavily on the combustibility of the materials used to construct the carriage. In 2012, a full-scale passenger rail tunnel fire test was conducted in Sweden to measure the temperatures and record the flashover times. It was concluded that flashover occurs approximately 13 minutes after ignition for carriages constructed unprotected combustible materials and 119 minutes for carriages constructed of noncombustible materials (15). Furthermore, temperature readings were recorded 29cm from the roof, with results shown in Figure 18 below.

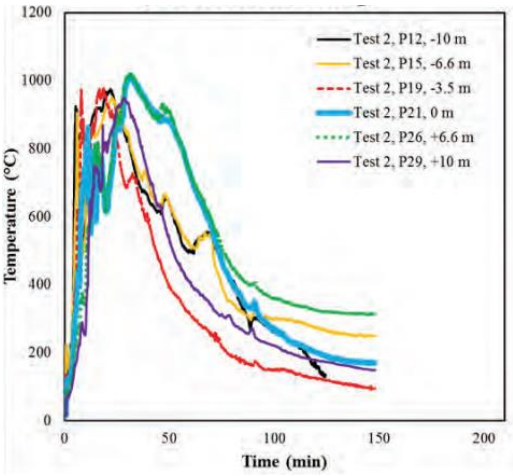

Figure 18: Temperature readings 29cm below ceiling in full-scale passenger train fire test (15)

Fire phase: at this phase, flashover has occurred and all inflammable materials are currently giving off heat. The duration of this phase depends mainly on the amount of combustible material

that is available to burn. The fire phase typically continues until 80% of the fuel source has been used.

Decay phase: at this phase, the temperature gradually drops as the fuel source begins to run out. At the end of the decay phase, the fuel source runs out and the fire burns itself out.

In terms of tunnel safety, the fire phase is of the most importance, as this phase contains the highest temperatures and therefore contributes most to the spalling and eventual structural failure of the tunnel.

2.3.3 Fire Protection

A tunnel's enclosed nature makes the occupants' ability to escape and battling the fire by emergency services more difficult. In addition, closing a tunnel for repairs or reconstruction bears a high societal cost due to tunnels' importance in transportation networks. Therefore, heavy fire safety regulations are imposed on structural engineers during the design process. While many such regulations exist to reduce the risk of ignition and assist in the ability of occupants to escape, this thesis will focus mainly on tunnels which lack certain protective measures that are typically put in place. Such measures are used in practice to prevent the concrete lining of the tunnel from excessive heating.

Concrete exhibits loss of strength at approximately 400°C (16), as seen in Figure 19. Steel reinforcement begins to lose its tensile strength at approximately 300°C (17) . To prevent strength loss, structural elements are typically designed so that the maximum temperatures of concrete and reinforcement do not exceed 380°C and 250°C respectively.

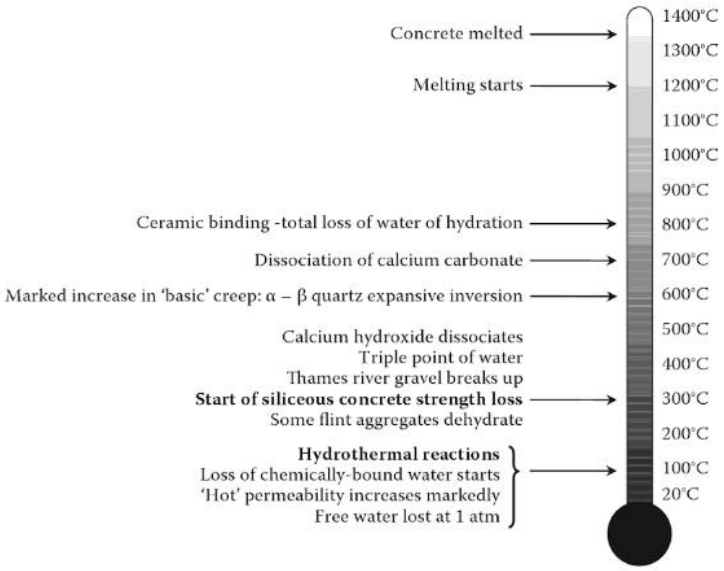

Figure 19: Temperature effects on concrete (16)

These temperature limits are achieved through the application of fire-protective spray-on material or as a board material which is applied to the underside of the tunnel. Before final approval of the design, a fire test is conducted on the panels which are representative of the final product. Thermocouples are placed on the concrete and steel to measure the temperature during the fire test.

2.4 Immersed Tube Tunnels

2.4.1 Introduction

Tunnels are underground passageways used to cross obstacles such as rivers or mountains. Tunnels have been used since ancient times, but modern design and construction methods have allowed for tunnels to become a safe and cost-effective option. If a tunnel is chosen as the most favorable option to cross a particular obstruction such as a river or a mountain, several construction methods are available, such as:

- *Shield driven* – construction of tunnels by use of a boring machine. The machine provides a temporary support structure until a permanent supporting material, such as reinforced concrete, can be put in place.

- *New Australian tunneling method (N.A.T.M.)* – makes use of the surrounding rock structure to stabilize the tunnel during construction
- *Drill and Blast Method* – utilizes explosives to blast through rock formations. This was a popular method before the invention of the tunnel boring machine
- ***Immersed Tube Method*** – precast elements are sunk into place and connected with water-tight joints. In this thesis project, the structural analysis of the cross-section is conducted on a tunnel using this method.

2.4.2 Construction Method

The immersed tube method involves the prefabrication of elements at an off-site location, floating the elements to the site, and sinking them to their desired location. During the prefabrication process, the sea floor is simultaneously dredged to create room for the elements (17) shows the floating of the elements to the site. Once the elements are confirmed to be in the proper location above their future permanent location, they are sunk using ballast (shown in Figure 21). The joints are constructed in a two-step process. The first step involves draining the water between the bulkheads, thus putting the pre-installed gaskets under pressure. An omega seal is then installed to secure the joint (18). A protective layer, shown in orange in Figure 23, is placed over the tunnel to protect the structure from the environment of the river.

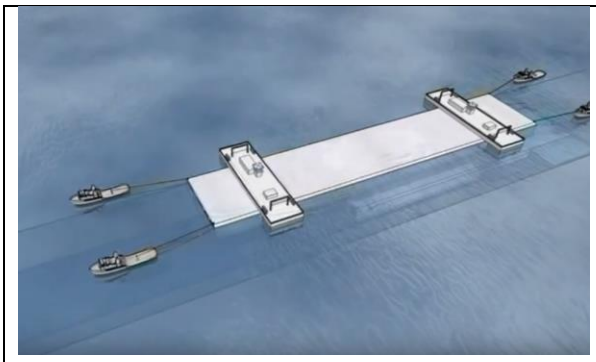

Figure 20: Prefabricated elements are floated to the site

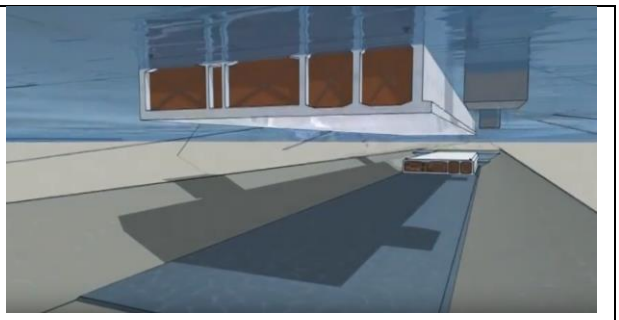

Figure 21: The prefabricated elements are sunk to the riverbed using ballast

Figure 22: The water between the two segments is pumped out to create a watertight seal

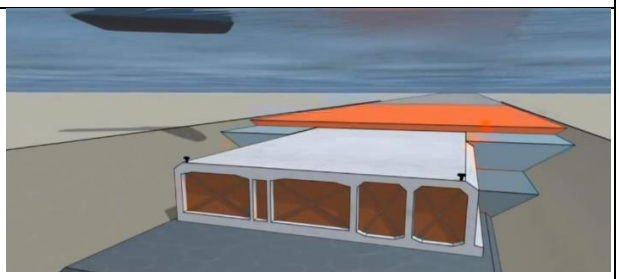

Figure 23: A protective layer (shown in orange) is placed above the tunnel

**Figure 20,Figure 21,Figure 22,Figure 23 from The Fehmarnbelt tunnel project*

A significant advantage of the immersed tube method is its relatively shallow nature compared to its counterparts. The tunnel's shallow nature is due to the absence of boring during the construction. When using a boring machine to tunnel, it is necessary to excavate deeper to ensure stability during the construction process. This results in a longer and more expensive tunnel. The differences between the tunnels can be seen in Figure 24 below.

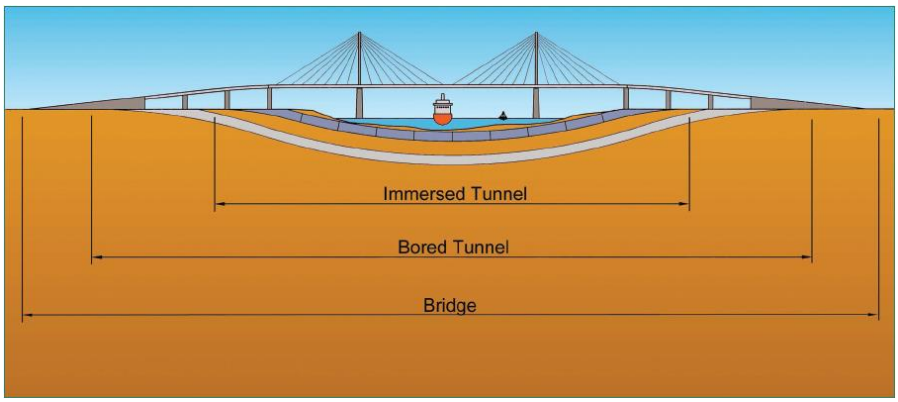

Figure 24: Comparison between different structures to cross a river

2.4.3 Fire Protective Measures of Concrete Lined Tunnels

Several fire protection measures are taken in the construction of immersed tubes. These include:

- systems designed to prevent ignition, such as the monitoring and restriction of certain hazardous materials
- systems that limit fire growth, such as ventilation and sprinkler systems
- access for emergency services to more effectively combat the fire
- application of fire-resistant material on the surface of the concrete to prevent the temperature induced deterioration of mechanical properties of the structure
- addition of additives such as polypropylene fibers to concrete to prevent spalling (19)

3 Goals of the Thesis Project

It is well established that fire negatively impacts concrete performance (20). However, it is currently unclear how fire affects the ability of CMA to provide additional bearing capacity to immersed tube roof slabs. In order to better understand the impact of fire on the development of CMA in an immersed tube, three independent research questions are addressed. The first research question of this thesis project is: **How does thermal degradation of concrete's compressive strength affect the formation of CMA in an immersed tube roof slab subjected to fire?** This question will subsequently be referred to as 'Question 1' in this thesis report.

Another phenomenon known to occur in concrete structures subjected to fires is spalling: the phenomenon whereby medium to large sections of concrete are suddenly and violently detached from the main structure. Spalling therefore results in a loss of structural material and a reduced cross section. It is theorized that the cross-section reduction due to spalling may inhibit the formation of CMA and therefore negate its contribution to the roof slab's ultimate bearing capacity. Therefore, the second research question of this thesis project is: **How does spalling influence the formation of CMA and the ultimate bearing capacity of an immersed tube?** This question will subsequently be referred to as 'Question 2' in this thesis report.

The final goal of this thesis project is to quantify the effect of lateral stiffness on the development of CMA in the roof slabs of immersed tubes. In an immersed tube, the surrounding soil is a major source of lateral stiffness. The formation of CMA may therefore be jeopardized by soil which is unable to provide the necessary lateral stiffness. To address the topic of lateral stiffness in immersed tubes, a sensitivity study is conducted to answer the final research question: **How does lateral stiffness affect the formation of CMA and the ultimate bearing capacity of the immersed tube roof slab?** This question is subsequently referred to as 'Question 3' in this thesis report.

Together, these three research questions can provide a foundation for researchers to further investigate the contribution of CMA to immersed tubes subjected to fires and the factors which may inhibit its formation. The goal of this thesis is therefore to provide a better understanding of the boundary conditions necessary for the development of CMA in immersed tube roof slabs and its potential benefit to the structure.

In Section 4, hand calculations are developed before a detailed description of the finite element model is presented in Section 5. The three questions of the thesis report are then investigated through the use of the finite element model, followed by a discussion of results and suggestions for further research.

4 Hand Calculations of the Model

The main tool used to investigate the questions of this thesis project is finite element modeling, a numerical method commonly used in structural analysis. While numerical methods are highly accurate and reliable, simple modeling choices can significantly influence results. It is therefore necessary to conduct basic hand calculations to establish a standard to which the results of the finite element model are compared. The ultimate bearing capacity, load at first crack formation, and the design load of an immersed tube are calculated. In these hand calculations, the geometry of the roof slab is taken from an immersed tube in the Netherlands, while the justification of material properties and reinforcement geometry chosen is described below.

4.1 Material Properties

The concrete used in this thesis project is typical of concrete used in immersed tubes in the Netherlands. It has a compressive strength of 27 MPa. The material properties of the reinforcement are mentioned in Section 5.2.1. As seen in elevation, the reinforcement layout of the roof slab utilized in this thesis project in the roof is seen below in Figure 25. The reinforcement layout is shown below and is based upon the reinforcement of a tunnel in the Netherlands.

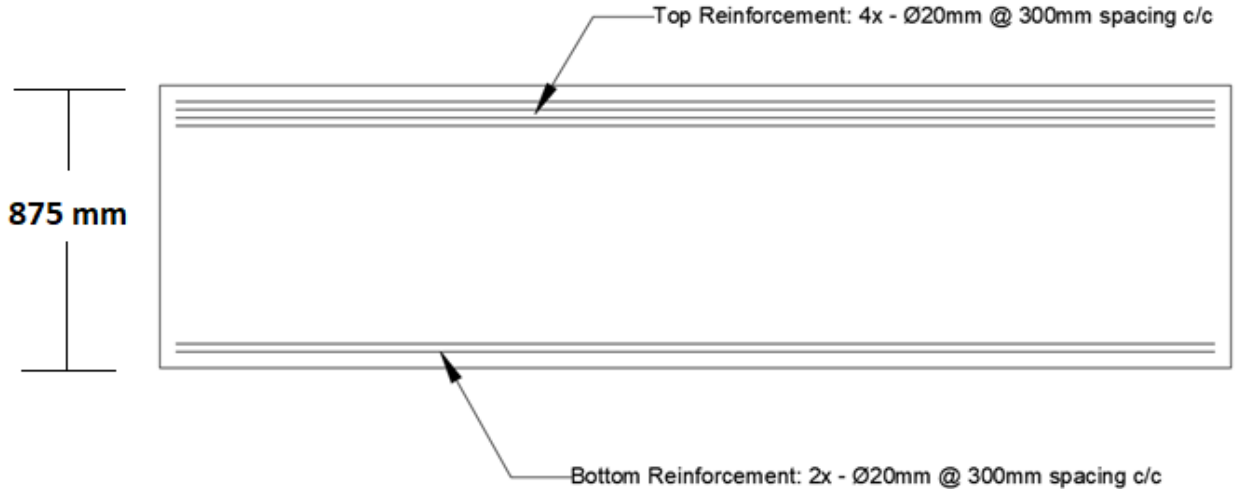

Figure 25: Bending reinforcement layout in roof slab of immersed tube.

The reinforcement as seen in Figure 25 can be simplified in terms of area of reinforcement per unit width of the roof slab. This simplification procedure can be seen below.

Bottom

$Area_{bottom} = 314\ mm^2 * 2 = 628 mm^2$

$Spacing_{bottom} = 300\ mm$

$$Reinforcement\ per\ unit\ width = \frac{628\ mm^2}{300\ mm} = 2.09\ \frac{mm^2}{mm}$$

Finding equivalent bar diameter

$\frac{\pi}{4} d^2 = 2.09 mm^2 \ \rightarrow d = \sqrt{\frac{2.09 mm^2 * 4}{\pi}} =$ **1.63 *mm* per mm of roof slab width**

Top

$Area_{top} = 314\ mm^2 * 4 = 1256\ mm^2$

$Spacing_{bottom} = 300\ mm$

$$Reinforcement\ per\ unit\ width = \frac{1256mm^2}{300mm} = 4.19\ \frac{mm^2}{mm}$$

Finding equivalent bar diameter

$$\frac{\pi}{4}d^2 = 4.19mm^2 \rightarrow d = \sqrt{\frac{4.19mm^2 * 4}{\pi}} = \mathbf{2.31}\boldsymbol{mm}\ \textbf{per mm of roof slab width}$$

Figure 26 shows the simplified cross-section. Of course, such a reinforcement is not possible in real-life and is used solely for DIANA to generate a stiffness matrix representative of real-world conditions. The unusual geometry is a result of several layers of reinforcement being consolidated into a single layer to simplify the calculation procedure. The height of the roof slab, 875 mm, is not to scale in the figure.

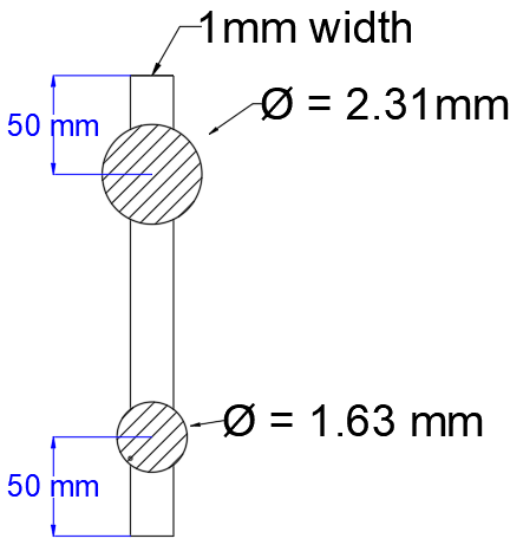

Figure 26: Simplified reinforcement layout

Additionally, to further simplify the procedure, the moment diagram of a fixed-fixed beam with UDL is taken into consideration when analyzing the roof slab's moment capacity at the ends and at midpoint. Specifically, only the top reinforcement is considered when determining the moment capacity at the ends due to the hogging moment and only the bottom reinforcement is considered when determining the moment capacity in the middle of the beam due to the sagging moment, as seen below in Figure 27.

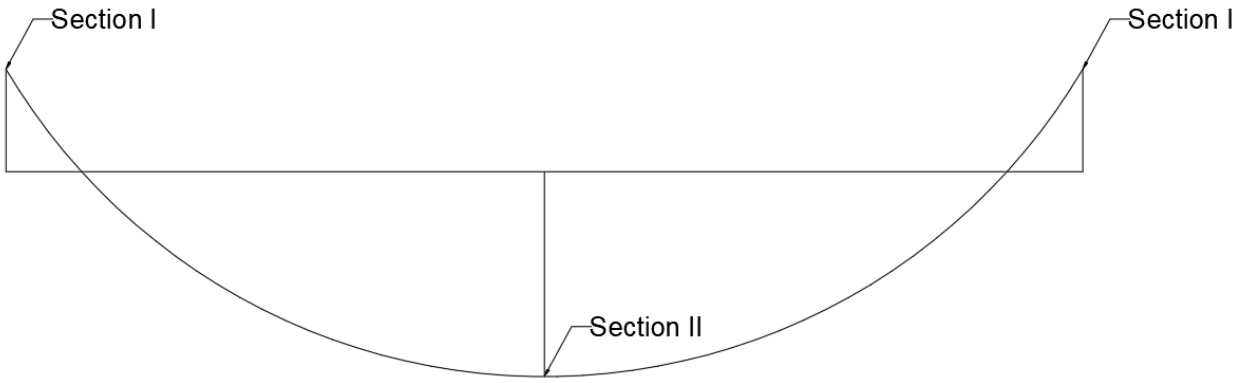

Figure 27: Moment diagram of fixed-fixed beam with section labelling

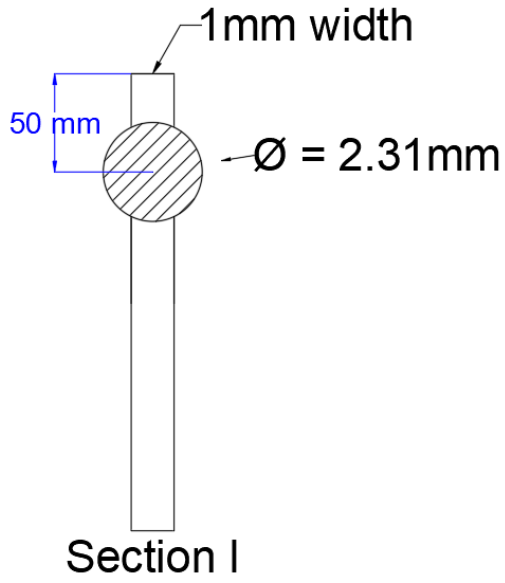

Figure 28: Simplified reinforcement Section 1

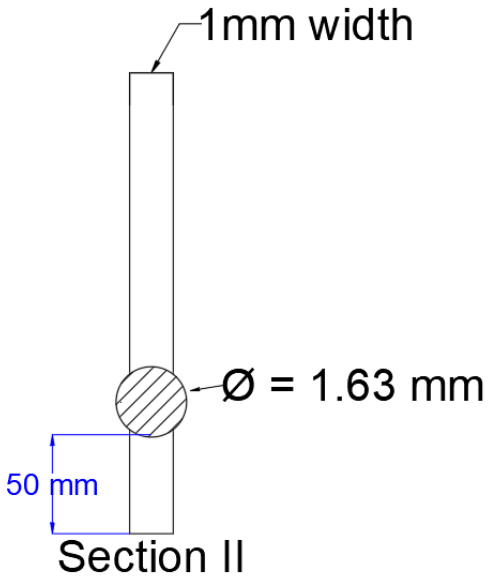

Figure 29: Simplified reinforcement Section II

4.2 Ultimate Bearing Capacity

A plastic analysis is conducted by considering the formation of three plastic hinges governing the overall behavior of the roof slab. These plastic hinges develop as the load increases. The formation and ultimate failure of the plastic hinges govern the overall load-bearing capacity of the roof slab. The plastic moments can then be calculated for Sections I and II through simple mechanics:

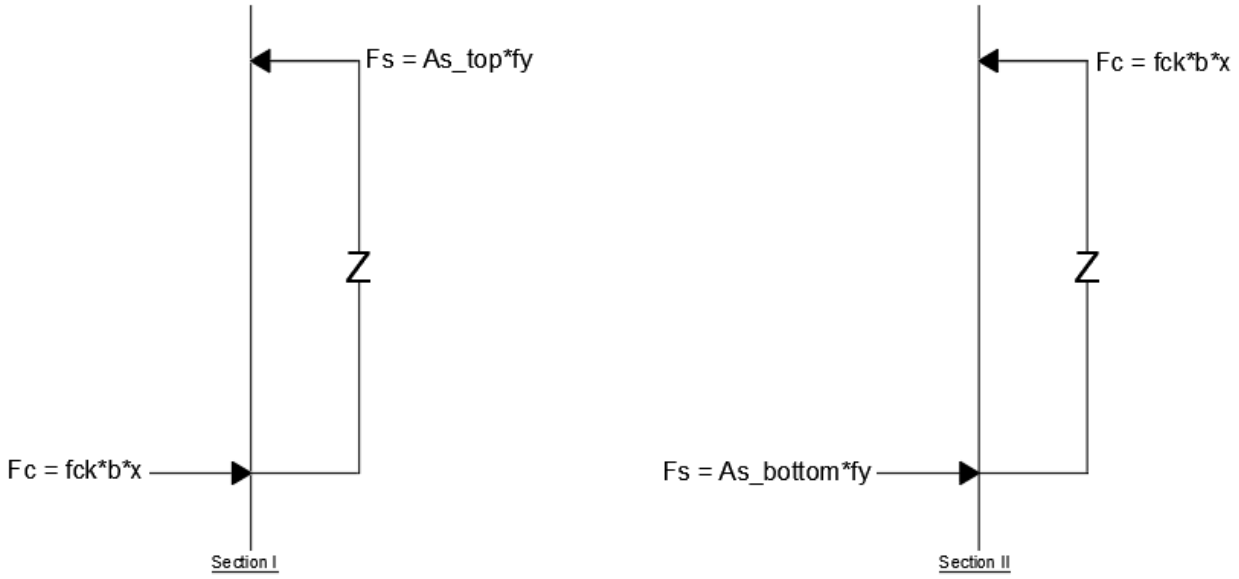

Figure 30: Forces associated with bending for Section I and Section II

Moment Capacity Section I

$$F_s = A_s * f_y = 4.19mm^2 * 400\frac{N}{mm^2} = 1672\ N$$

$$F_c = f_c * b * x = 27\frac{N}{mm^2} * 1mm * x\ mm = 27 * x$$

$$F_s = F_c \ \therefore\ x_{Section\ I} = 88mm$$

$$M_{p_{Section\ I}} = F_s * z = F_c * z = 1672\ N * \left(875mm - 50mm - \frac{88mm}{2}\right) = 1.3e6\ Nmm$$

Moment Capacity Section II

$$F_s = A_s * f_y = 2.09mm^2 * 400\frac{N}{mm^2} = 836\ N$$

$$F_c = f_c * b * x = 27\frac{N}{mm^2} * 1mm * x\ mm = 27 * x$$

$$F_s = F_c \ \therefore\ x_{Section\ I} = 44\ mm$$

$$M_{p_{Section\ II}} = F_s * z = F_c * z = 836\ N * \left(875mm - 50mm - \frac{44\ mm}{2}\right) = 6.71e5\ Nmm$$

Three plastic hinges are expected to form in the roof slab, as seen below. To approximate the ultimate bearing capacity of the section, the external work and internal work are equated.

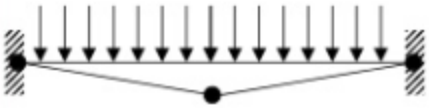

Calculation of External Work

$$F_{external} = w_{ult} * \left(\frac{1}{2} * \delta * \frac{L}{2} * 2\right) \quad where\ \delta = \frac{\theta * L}{2}\ \ by\ small\ angles$$

$$\therefore\ F_{external} = w_{ult} * \left(\frac{L^2 * \theta}{4}\right)$$

Calculation of Internal Work

$$F_{internal} = M_{p_I}\theta + M_{p_I}\theta + M_{p_{II}}2\theta$$

Setting internal work equal to external work [energy conservation]

$$F_{internal} = M_{p_I}\theta + M_{p_I}\theta + M_{p_{II}}2\theta = \ F_{external} = w_{ult} * \left(\frac{L^2 * \theta}{4}\right)$$

$$\therefore\ \ \boldsymbol{w_{ult} = 0.36\ \frac{N}{mm^2}}$$

The above hand calculations demonstrate that at 0.36 $\frac{N}{mm^2}$, three plastic hinges have been formed and the section cannot take withstand any more load without failure.

4.3 Formation of First Crack

The load at which first instance of cracking occurs is an important quantity to know due to the activation of the reinforcement. At this load, a change in stiffness can be expected in the roof slab.

$$\sigma_{crack} = \frac{M_{crack}c}{I} \quad ;where\ \ I = \frac{bh^3}{12} = \frac{1mm \cdot (875mm)^3}{12} = 5.6e7mm^4$$

$$and\ \ c = \frac{h}{2} = 437.5mm$$

$$M_{crack} = \frac{\sigma_{crack} \cdot I}{c} = \frac{3\frac{N}{mm^2} \cdot 5.6e7mm^4}{437.5mm} = 3.84e5\ N \cdot mm \quad \therefore\ \boldsymbol{q_{crack} = 0.21\ \frac{N}{mm^2}}$$

It is determined from the above calculations that the expected first crack will occur with a loading of 0.21 $\frac{N}{mm^2}$ and the expected ultimate load is 0.36 $\frac{N}{mm^2}$.

4.4 Design Load

The design load is approximated to be equivalent to the weight of the water and the soil above the roof slab of the immersed tube. A schematic drawing of a typical immersed tube in the Netherlands can be seen below in Figure 31.

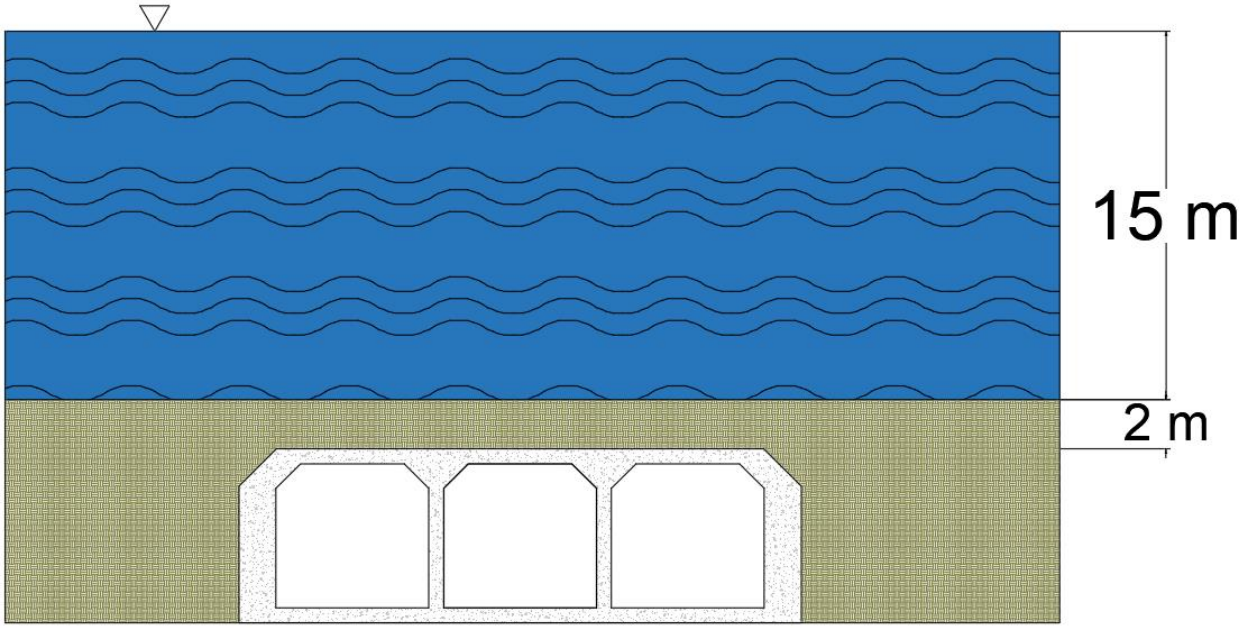

Figure 31: Typical cross-section of immersed tube in the Netherlands

By making use of sand with density ρ = 2040$\frac{kg}{m^3}$, the vertical force on the top of the roof slab is $q_{Design} = 0.19 \frac{N}{mm^2}$.

In this section, the expected load at first crack, the ultimate bearing capacity, and the design load are approximated through and calculations. These values are used as a reference when determining the accuracy of our finite element model.

5 The Finite Element Model

The finite element method is chosen as the method by which to conduct the structural analysis of a roof slab of a concrete-lined immersed tube under fire conditions. The finite element method is chosen due to its ability to provide insights into the structure's internal temperatures, stresses, and strains during the loading procedure. Furthermore, computer methods are a naturally non-destructive method of studying a structure's response to loading.

The finite element model used in this thesis project is a two-dimensional plane stress model, meaning that the normal stress perpendicular to the plane are equal to 0. In the immersed tube, the service load from above is the load of interest and any loading applied perpendicular to the cross-section of the tunnel can be considered negligible. Therefore, the model can be considered to be in a plane stress situation, significantly reducing its complexity. The model is given a unit depth of 1 mm to simplify calculation procedures.

The accuracy of a finite element model is highly dependent on the modeling considerations and assumptions made by the user. Simplifications reduce computing time, but also reduce accuracy. In this section of the report, the modeling procedure is discussed in detail.

5.1 Model Geometry

Several geometries of immersed tubes are implemented in the Netherlands. The number of tubes, the thickness of the walls, and other defining features are dependent on the expected traffic load and the subsequent structural requirements. Some cross-sections typical in the Netherlands are shown below.

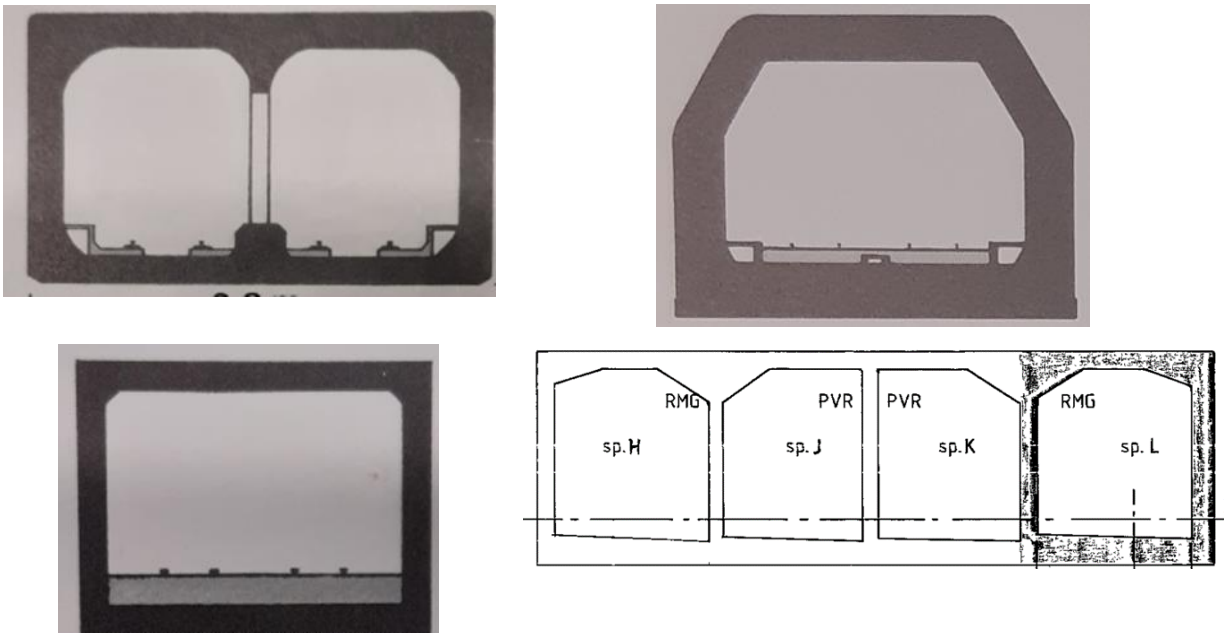

Figure 32: Typical Immersed Tube Cross Sections in the Netherlands

In this thesis, a cross-section with three tubes and thick walls is selected, as seen below in Figure 33. Compressive membrane action can be most expected in a middle tube and thus a cross-section with three inner tubes is selected. A cross-section of typical dimensions in the Netherlands is chosen for this study. The cross-section is shown below with the red rectangle showing the modeling area of interest.

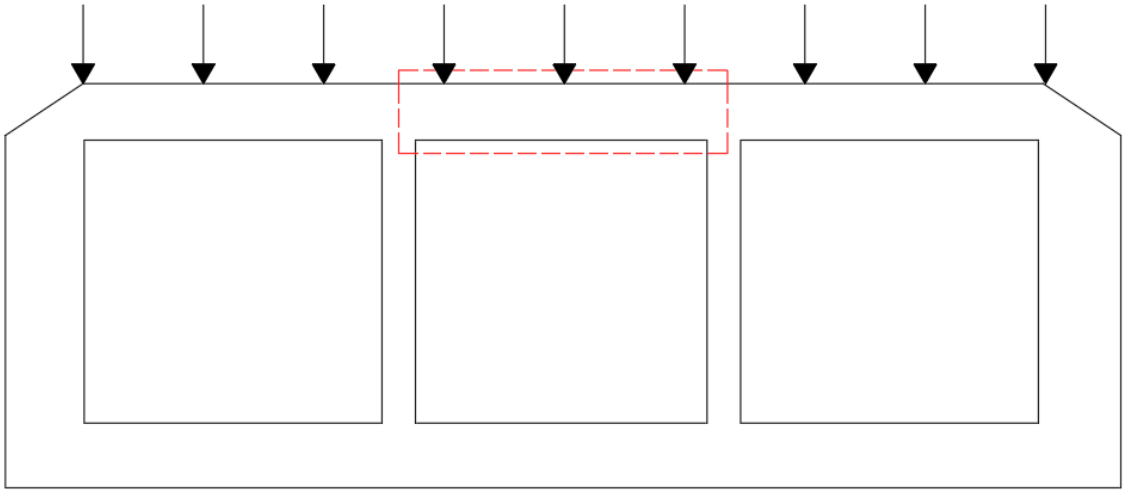

Figure 33: Typical immersed tube cross-section with the rectangle in red showing the area of interest

As mentioned above, only one side of the roof slab is modelled due to symmetry. The left side of red rectangle in the above figure is modelled in DIANA. By modeling only half of the roof slab, a great deal of computing time is saved. The modeling area of interest in shown below.

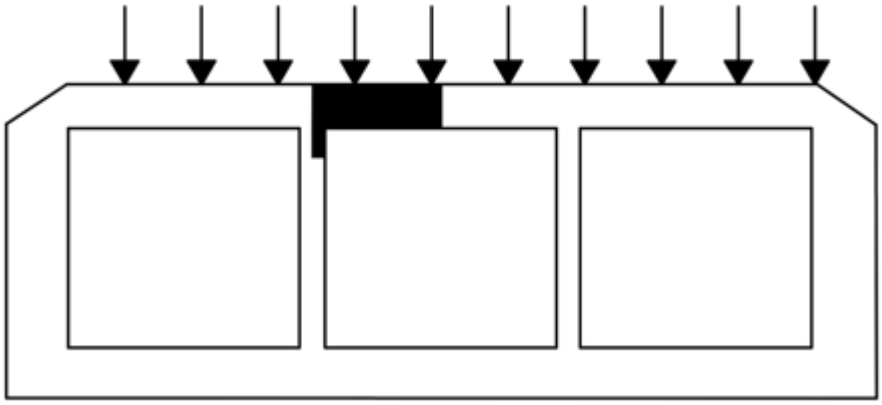

Figure 34: Modeling area of interest

The above figure represents the left-hand side of the roof slab. Additional concrete material (1375mm x 250mm) is present at the left side of the beam to model the rotational stiffness of the roof-to-wall connection. In effect, 250 mm and 500 mm of concrete are added in the horizontal and vertical directions respectively and are supported by fixed connections. A graphic representation of the model geometry is shown below.

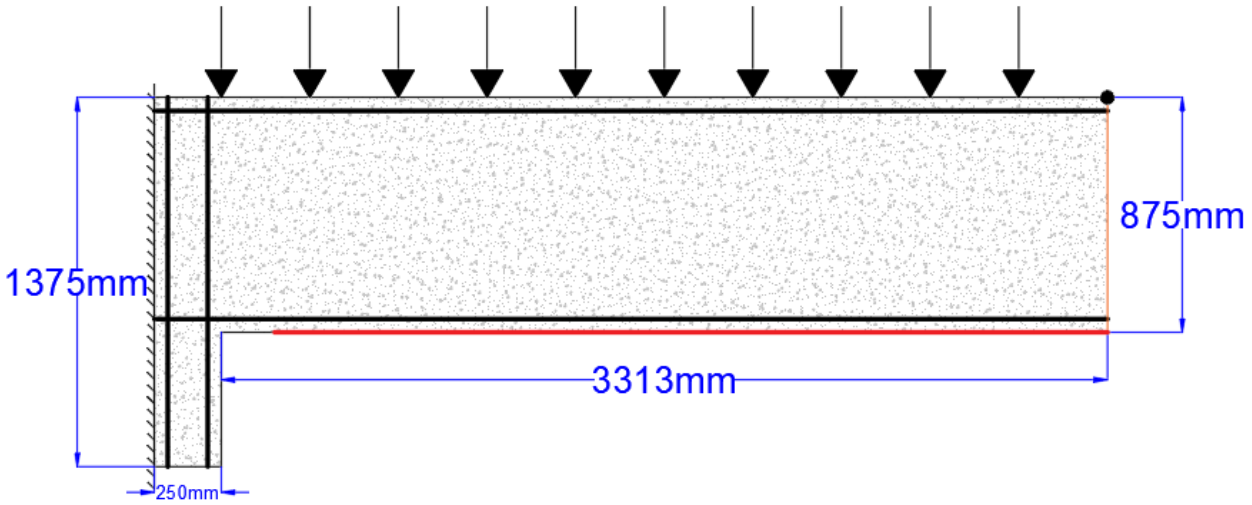

Figure 35: Representation of modeling area of interest

Reinforcement is shown with thick black lines. The reinforcement in the slab has 50 mm cover. A master-slave relation is established through the use of a tie connecting the lateral displacements of the upper-right-hand node of the model and the symmetry edge to ensure that the symmetry plane remains vertical throughout the loading procedure. The node which is used for the tie is shown in black in the upper-right-hand corner in the above figure and the 'slave' edge is shown in orange. Furthermore, the Tunnel-Specific fire which will eventually be applied to the structure is transferred to the concrete material through a thermal boundary at the bottom of the roof slab, represented by a thick red line. The thermal boundary is shifted to the right 100mm as to improve the convergence behavior of the model. In reality, the thermal effects at the corner could soften nodes which are responsible for the development of CMA.

5.1.1 Boundary Conditions

The finite element model shown in Figure 36. Includes a fixed-connection at the left-hand-side. The reinforcement, with concrete cover 50mm, is shown in green.

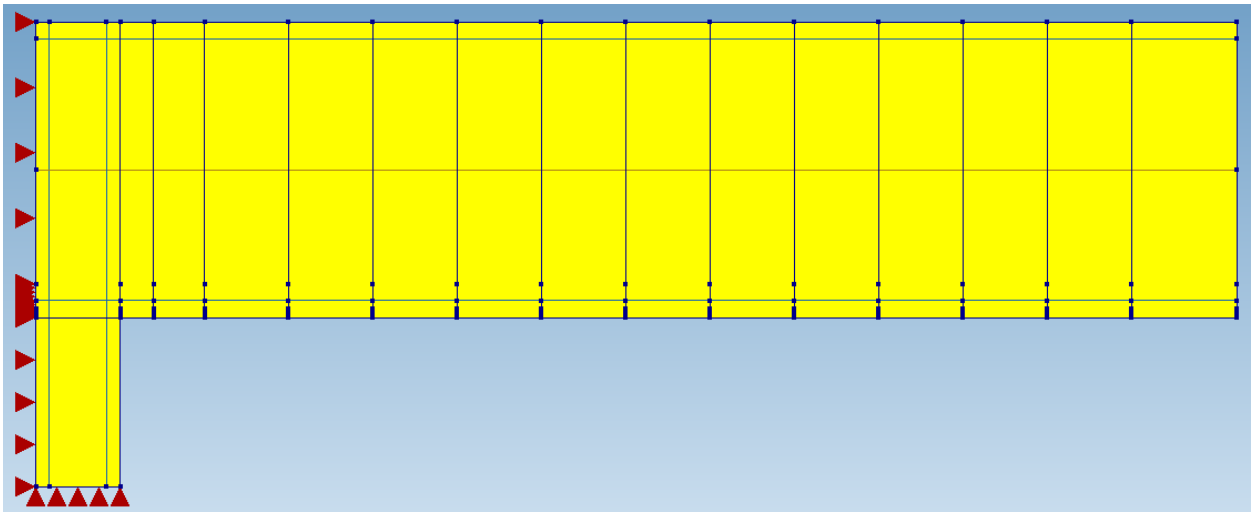

Figure 36:Finite element model representing a roof slab in an immersed tube

The loading can be seen below in Figure 37. The line has a value of 1 N/mm and is applied to the model in incremental load steps.

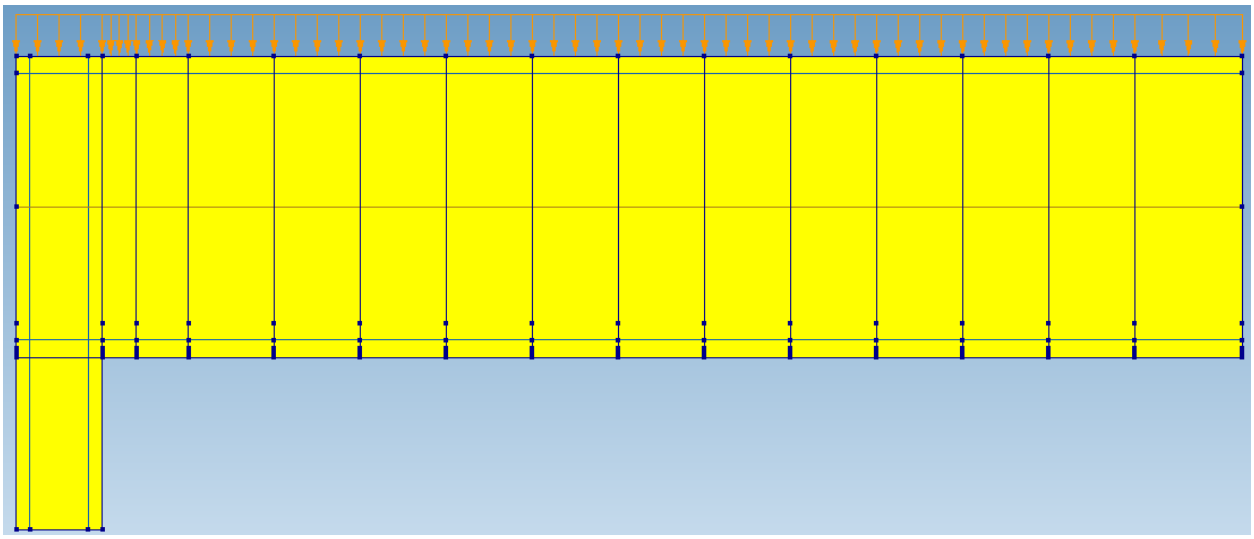

Figure 37: Loading of finite element model

The thermal boundary at which the fire curve is applied is shown in green below. The boundary exists along the bottom surface of the model. A gap of 100mm is left between the side and wall and the beginning of the boundary to prevent stress concentrations at the corner.

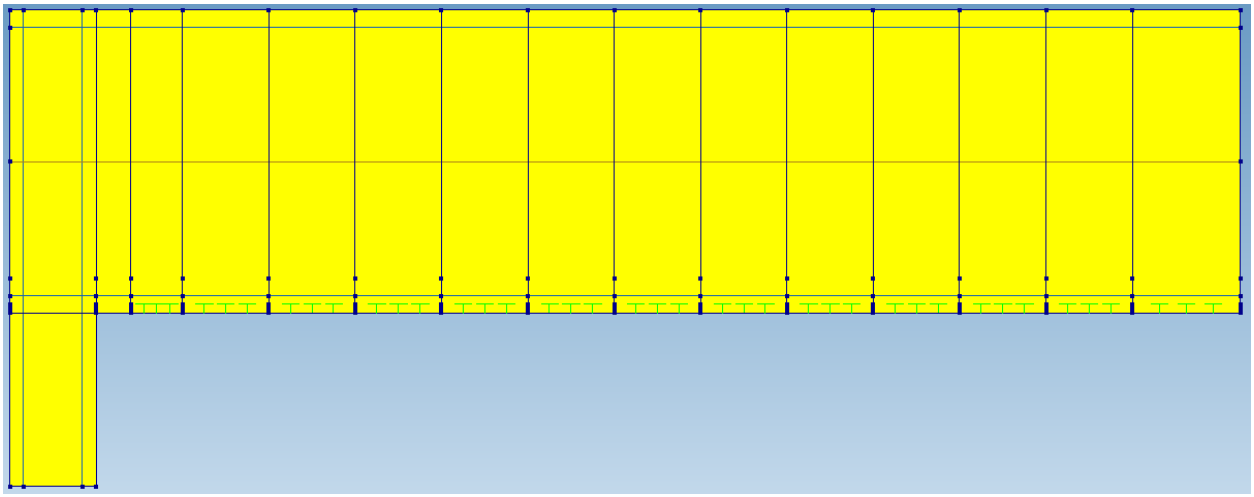

Figure 38: Thermal boundary of the finite element model

5.1.2 Calculation Procedure

Arc length control is used for the model in order to adequately capture the post-peak behavior of the load-displacement diagram. Two nodes are selected for the arc-length control procedure: one node in the vertical direction for bending and one in the lateral direction for crushing.

Physical and geometrical nonlinearity are considered. Physical nonlinearity accounts for cracking behavior and geometrical nonlinearity is necessary for the development of CMA. Geometrical nonlinearity is necessary due to the redistribution of internal forces after significant deformations. Equilibrium equations must therefore be recalculated with a significant change in geometry of the roof slab. Regular Newton-Raphson iteration procedure is used in the finite element model.

The complete specifications of the finite element calculation procedure can be found in 12.11.

5.1.3 Soil Pressure

The weight of the water and saturated soil will result in a lateral pressure on the structure. With dimensions shown in Figure 31, the expected lateral pressure is $\sigma = 0.345$ N/mm². With a roof slab height of 875mm, this pressure implies a force of 302 N/mm. This force can be considered negligible compared to the normal forces resulting from vertical loading. For that reason, the initial lateral stress resulting from soil and water are not considered in the finite element representation. The buildup of normal force during vertical loading which justifies neglecting initial lateral pressure can be seen in Section 12.4 Figure 95.

5.2 Material Models

5.2.1 Reinforcement

The reinforcement chosen for the model has a yield stress of 400 MPa and an elastic modulus of 200 GPa. The reinforcement is selected to be embedded. This means that the reinforcement does not have degrees of freedom of its own, but rather its displacements (and therefore stresses/strains) are tied directly to the displacements of the mother element (concrete).

5.2.2 Concrete

The ability to accurately estimate the degree of thermal degradation of concrete exposed to fire plays a key role in quantifying the effect that the fire has on the formation of CMA. Establishing accurate material properties is essential for the overall confidence that the user of a finite element software package can have in the results. Therefore, it is of critical importance to accurately define the temperature dependent material properties of concrete.

5.2.2.1 Mechanical Properties

The temperature dependent tensile and compressive strengths along with the temperature dependent elastic modulus of concrete are taken directly from NEN 1992-1-2, the EC document governing actions on structures exposed to fire. Temperature dependent mechanical properties are seen in Figure 110, Figure 111, and Figure 112 in Section 12.7.

5.2.2.2 Thermal Conductivity, Capacity, and Expansion

The conductivity and capacity ultimately determine the increase in temperature of the material during the fire exposure. It is the increase in temperature which leads to thermal degradation. Therefore, great care is taken in guaranteeing the accuracy these material properties.

The thermal expansion coefficient is defined as the strain experienced by a material per unit change in temperature and is described by the relationship $\alpha = \frac{\varepsilon}{\Delta T}$. The thermal strain is defined in NEN 1992-1-2 as follows:

$$\varepsilon_c(\theta) = -1{,}8 \times 10^{-4} + 9 \times 10^{-6}\theta + 2{,}3 \times 10^{-11}\theta^3 \quad \text{for } 20°C \leq \theta \leq 700°C$$
$$\varepsilon_c(\theta) = 14 \times 10^{-3} \quad \text{for } 700°C < \theta \leq 1200°C$$

To use the thermal strains defined in NEN 1992-1-2 in the DIANA software package, the values must be converted from temperature dependent strain to temperature dependent expansion coefficient. To do so, values of linear thermal strain are evaluated for different temperatures using the relation shown above. The difference in temperature ΔT is calculated as a reference from 20°C, the lower bound of the above relation. In that way, the coefficient of linear thermal expansion can be calculated for different temperatures. The result is seen in in Section 12.7. The thermal capacity and thermal conductivity are taken directly from NEN 1992-1-2 and are seen in Figure 114 and Figure 115 in Section 12.7 respectively.

5.2.2.3 Verification of Thermal Properties of Concrete

The ISO 834 fire curve is applied to the concrete structure in the finite element model through a flow boundary with an emissivity coefficient of 0.7, as defined in NEN 1992-1-2 Annex A. ISO 834 is the fire curve used in NEN 1992-1-2 and is therefore used to verify the temperature dependent thermal properties of concrete.

Contour probes are taken for a depth of 100 mm in the finite element model, beginning at the bottom surface of the concrete and extending upwards into the body of the structure. Figure 116 through Figure 119 in Section 12.7 show a close correlation between the temperature penetration expected from the EC and the temperature results from the finite element simulation. It can be expected that a mesh refinement and smaller step sizes in the finite element calculation would produce even more accurate results as compared to the FEA results depicted.

To quantify the error between NEN 1992-1-2 values and results from the DIANA analysis, fifty points are taken along the 100 mm contour probe. The percentage of error of each point is calculated by comparing the temperature of each point along the contour probe in the finite element model to the expected result in NEN 1992-1-2. The results are tabulated in Table 2.

Table 2: Summary of error between EC and finite element simulation

Time Exposed to ISO -834 Fire Curve	Average % error
30 min	7.62%
60 min	4.90%
90 min	3.72%
120 min	2.74%
Overall	**4.75%**

With an average overall error of 4.75%, it can be said confidently that the concrete thermal defined in the finite element model closely resembles the NEN 1992-1-2 model.

5.3 Meshing

It is desirable to produce a mesh which gives accurate results while being efficient in terms of computation time. Finer meshes give more accurate results while costing computing time. Meshes can be made to be fine in certain areas, where high stress concentrations and nonlinear phenomena can be expected, and coarse in other areas, where stress concentrations are not expected.

The meshing involved in this procedure must consider the significant thermal activity at the bottom of the concrete surface. The tunnel-specific fire curve is will only be applied to the bottom of the roof slab. Therefore, the mesh used for the analysis is fine at the bottom and gradually becomes coarser deeper in the structure. The mesh is made to have a finer element height of 12.5 mm and increased to coarser elements with height 129 mm at the top of the roof slab with a gradation smoothness of 1.0.

Furthermore, in accordance with internal force development associated with CMA, high stress concentrations are expected at the left-hand-side of the model due to the compressive strut. Therefore, the mesh has a fine width of 50 mm at the left-hand-side and gradually increases to 150 mm on the right-hand-side.

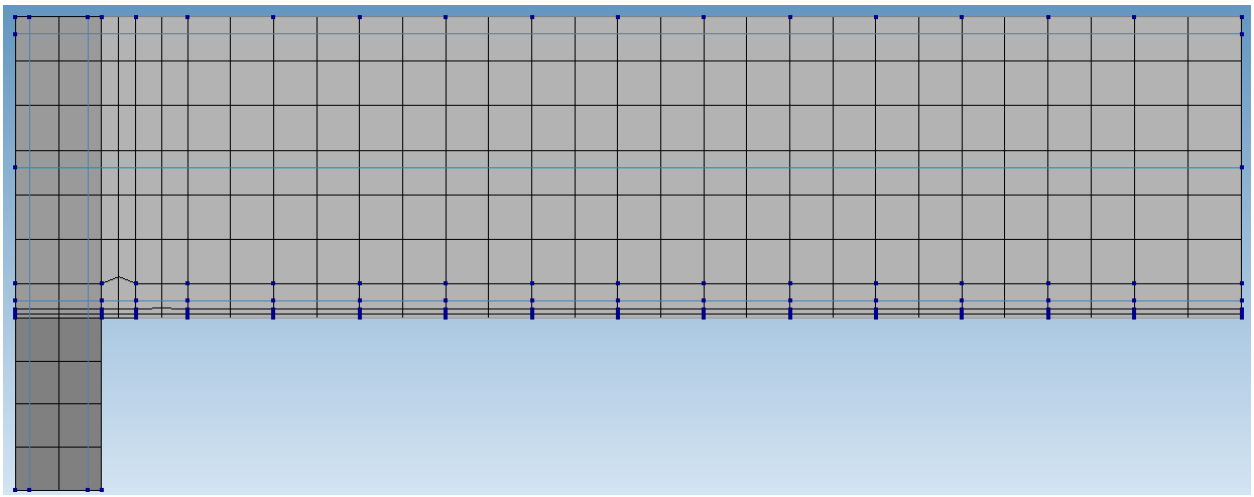

Figure 39: Meshing used throughout thesis project

5.4 Concrete Compression Curve

The constitutive model defines the stress-strain relationship of a material. It is a simplified representation of the true behavior of a material under loading. Several models are available in finite element software packages to simulate the compression domain of the stress-strain relationship of concrete. The model chosen is of great importance to the accuracy of the finite element analysis. Proper care is thus taken to define a material model which adequately approximates concrete's complex cracking, post-peak behavior, and strength.

To avoid the well-known 'stress locking' phenomenon and a subsequent overestimation of the ultimate bearing capacity of the structure, a total-strain based rotating crack model is chosen (21). Furthermore, a rotating crack model is implemented since the exact location of each concrete crack is unknown.

The temperature dependency of the stress-strain relationship of concrete is of particular importance to this thesis project due to the exposure of the concrete to fire conditions and the subsequent increase in its ductility and strength degradation with increased temperature. Therefore, the NEN 1992-1-2 compression curve built into DIANA is used. The NEN 1992-1-2 is a curve characterized by three independent parameters

- ε_{c1} – the strain associated with the point of maximum stress
- ε_{cu} – the maximum allowable strain
- f_c – the compressive strength of the concrete

These three parameters are each functions of temperature and are given in Section 12.10. The temperature dependent parameters are meant to model the reduction of strength and the increase in ductility with increasing temperature. Experimental results show this to be the case, as seen in the figure below (22).

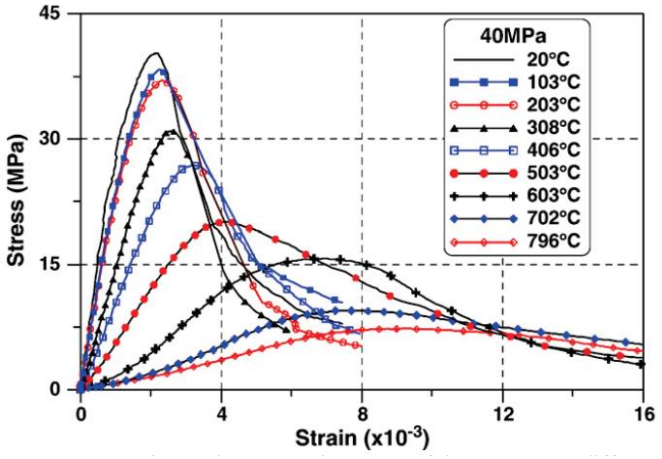

Figure 40: Concrete compression curve at elevated temperatures, experimental results

While the NEN 1992-1-2 curve is temperature dependent, it is also mesh dependent. In mesh dependent curves, the softening behavior is specified for localizing phenomena such as cracking or crushing in terms of strain without accounting for the mesh size. This results in different softening behaviors for different elements based on their respective sizes. Therefore, the crack-band width, which is a function of the element size, has a significant influence on the post-peak stress strain diagram in the NEN 1992-1-2 compression curve. Results in the finite element analysis are therefore highly dependent on the mesh size when using the NEN 1992-1-2. Contrarily, the parabolic curve is a mesh independent curve. This means that the crack-band width, and therefore the element size, is considered when defining the softening behavior of each element.

Although the NEN 1992-1-2 compression curve is mesh dependent, the necessity of a temperature dependent compression curve requires its use in this thesis project. To overcome the mesh dependency associated with the NEN 1992-1-2 compression curve, the curve is adjusted to fit the mesh described in Section 5.2.2.3 by using the mesh-independent Parabolic curve. The two curves are seen below for comparison.

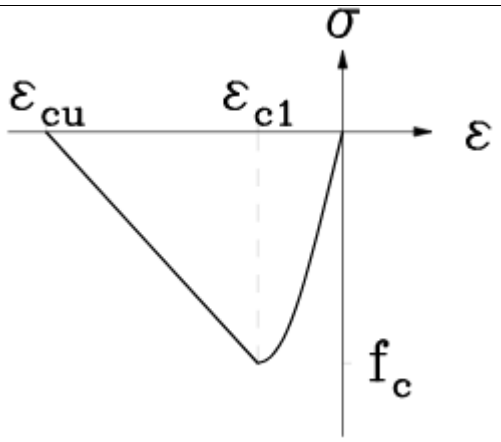

Figure 41: NEN 1992-1-2 compression curve

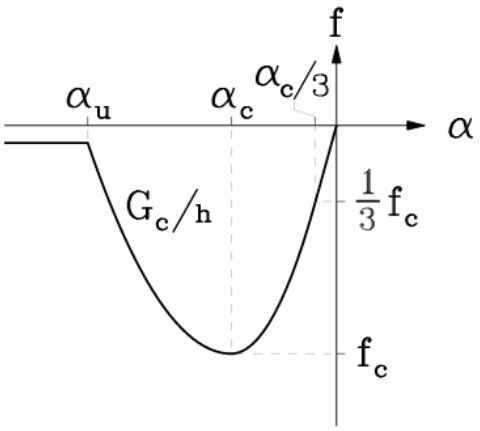

Figure 42: Parabolic Compression Curve

The calibration of the NEN 1992-1-2 compression curve is based on experimental data and on the mesh independent Parabolic compression curve. The goal is to create a suitable compression curve by adjusting the NEN 1992-1-2 compression curve to fit the mesh used in the finite element model. In that way, the NEN 1992-1-2 compression curve is temperature dependent and appropriate for the mesh sized used in the finite element model.

The calibration of NEN 1992-1-2 begins by defining the Parabolic curve. The Parabolic compression curve is fully described by: (23)

- $\alpha_{c/3}$ – the strain at which one third of the compressive strength is reached

$$\alpha_{c/3} = -\frac{1}{3}\frac{f_c}{E}$$

- α_c – the strain at which the maximum compressive strength is reached

$$\alpha_c = -\frac{5}{3}\frac{f_c}{E} = 5\ \alpha_{c/3}$$

- α_u – the strain at which the material is completely softened in compression

$$\alpha_u = \min\left(\alpha_c - \frac{3}{2}\frac{G_c}{h\ f_c}, 2.5\alpha_c\right)$$

The Parabolic curve is then defined by the following set of equations:

$$f = \begin{cases} -f_c \ \frac{1}{3} \ \frac{\alpha_j}{\alpha_{c/3}} & \text{if } \alpha_{c/3} < \alpha_j \leq 0 \\ -f_c \ \frac{1}{3} \left(1 + 4\left(\frac{\alpha_j - \alpha_{c/3}}{\alpha_c - \alpha_{c/3}}\right) - 2\left(\frac{\alpha_j - \alpha_{c/3}}{\alpha_c - \alpha_{c/3}}\right)^2\right) & \text{if } \alpha_c < \alpha_j \leq \alpha_{c/3} \\ -f_c \left(1 - \left(\frac{\alpha_j - \alpha_c}{\alpha_u - \alpha_c}\right)^2\right) & \text{if } \alpha_u < \alpha_j \leq \alpha_c \\ 0 & \text{if } \alpha_j \leq \alpha_u \end{cases}$$

Previous literature suggests that the ultimate strain of a 100 mm cube of concrete under uniaxial compression at 20°C is 7‰ (24). By adjusting the fracture energy G_c in the Parabolic curve, it is possible to create a Parabolic curve which meets that criterion. The defined Parabolic curve therefore matches results shown in experimental data. The adjustment of G_c and the resulting Parabolic compression curve can be seen in Section 12.1.

The Parabolic curve can now be used to calibrate the NEN 1992-1-2 curve. The calibration of the NEN 1992-1-2 to the Parabolic curve begins with the definition of the NEN 1992-1-2 curve for the domain [0, $\varepsilon_{c1,\Theta}$), which is fully described by the compressive strength $f_{c,\Theta}$ and the strain at maximum stress $\varepsilon_{c1,\Theta}$. $\varepsilon_{c1,\Theta}$ is taken as 0.0025, as stated in the EC. The curve for ε for the post-peak behavior, domain [0, $\varepsilon_{c1,\Theta}$], is defined below:

$$\frac{3\varepsilon f_{c,\theta}}{\varepsilon_{c1,\theta}\left(2 + \left(\frac{\varepsilon}{\varepsilon_{c1,\theta}}\right)^3\right)}$$

The post-peak behavior is defined by a straight line extending from the compressive strength associated with $\varepsilon_{c1,\Theta}$ down to the ε-axis. The point on the ε-axis with which the descending branch of the compression curve intersects is defined as ε_{cu} and represents the strain at which complete strength loss occurs. The calibration of NEN 1992-1-2 to the Parabolic curve and to experimental results is achieved by adjusting the value of ε_{cu} to create an NEN 1992-1-2 compression curve whose area under the curve is equivalent to that of the Parabolic curve. By equating the area of the NEN 1992-1-2 curve to the Parabolic curve, the energy associated with cracking and crushing are

made to be similar. The resulting ultimate strain ε_{cu} of the NEN 1992-1-2 compression curve is 0.0085. This calculation can be seen in detail in Section 12.1.

The NEN 1992-1-2 is now calibrated in terms of mesh size and experimental uniaxial compression results for a temperature of 20°C. To consider the temperature dependency ε_{c1} and ε_{cu}, a linear interpolation method is used between the calculated strains at 20°C (ε_{c1} = 0.003 and ε_{cu} = 0.0085) and the values for ε_{c1} and ε_{cu} at 1200°C in the EC (ε_{c1} = 0.025 and ε_{cu} = 0.0475). Consideration was also given to scaling the values of ε_{c1} and ε_{u} based on the increase of the two strains in the EC with temperature, but the value of ε_{c1} increases so rapidly between temperatures of 200-600°C as to overtake the value of ε_{cu}, resulting in a non-sensical post-peak behavior. Therefore, the linear interpolation method is implemented.

The compressive strength reduction is taken directly from EC and matches the values given in Table 5. The linearly interpolated values of ε_{c1} and ε_{cu} are given in Section 12.10 while graphical representations of the values are given below.

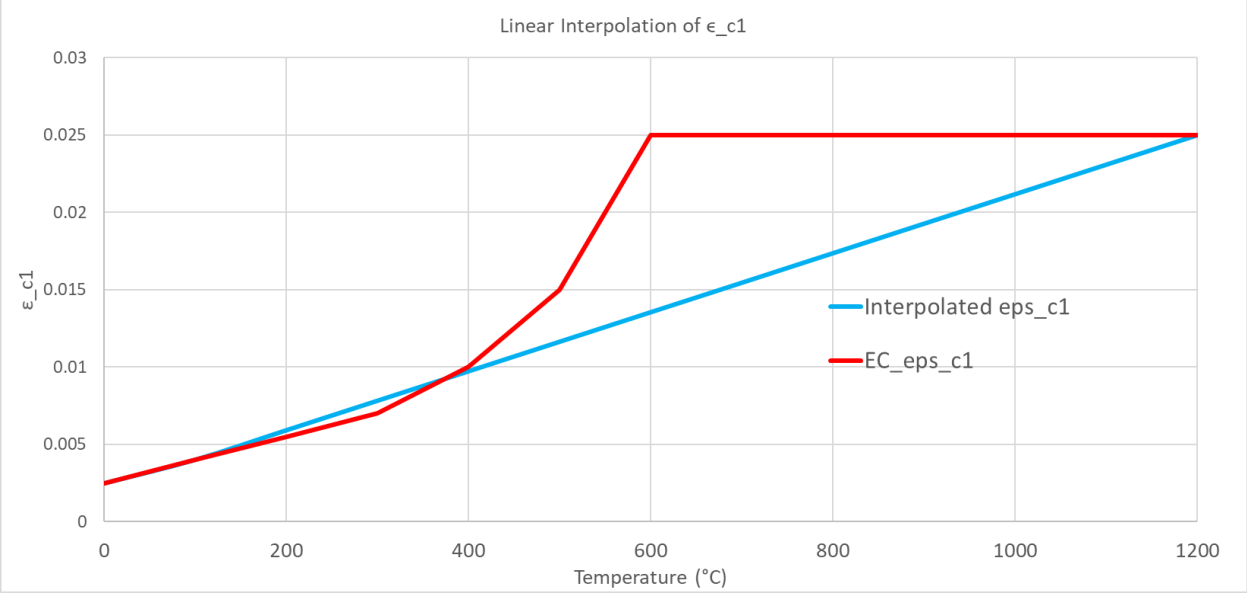

Figure 43: Interpolated values of ε_{c1}

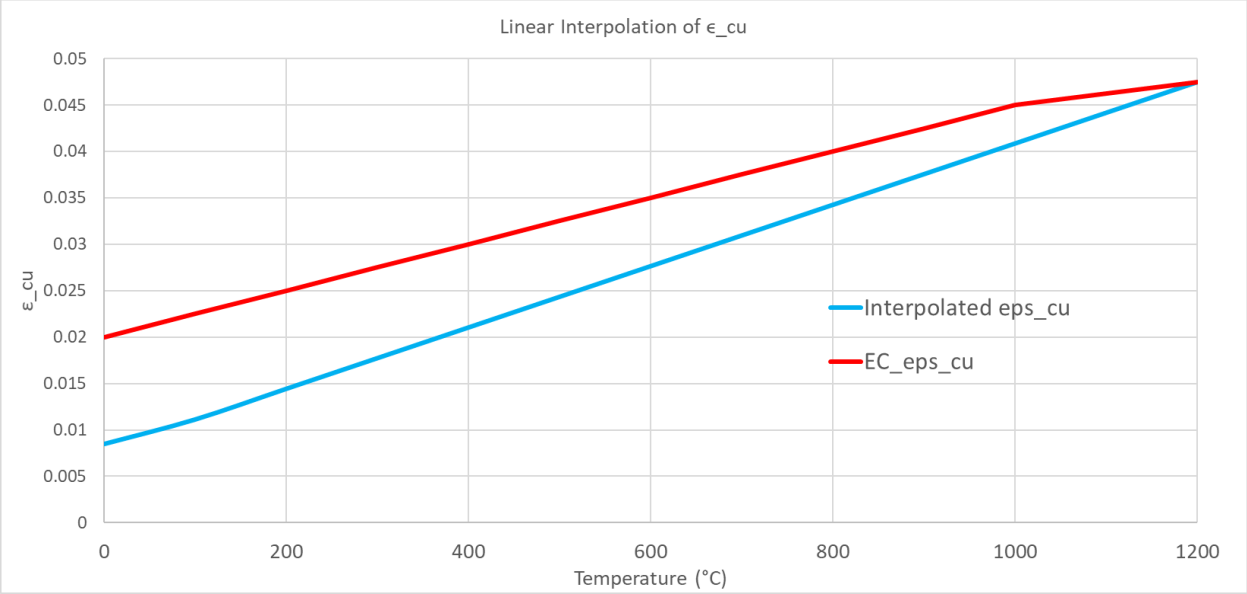

Figure 44: Interpolated values of ε_{cu}

By interpolating the strain values to match the EC values for 1200°C, the strength degradation and increase in ductility of concrete with increasing temperature is considered in the material model. The compression curve is also calibrated to fit the mesh size of the finite element model. It is important to note that while this calibration method is modelled after experimental results, further study is necessary to fully determine its accuracy and ability to adequately predict concrete behavior. The impact of using this calibration procedure is discussed in further detail in Section 10.

5.5 Determination of a Tunnel-Specific Fire Curve

While the ISO 834 fire curve is used to define the thermal properties of concrete, this thesis project concerns the fire resulting from train carriage ignition. An extensive 2018 CFD study using PyroSim was conducted in Arcadis in 2018 to determine a fire curve which estimates a railcar ignition in an immersed tube and will therefore be used extensively in this thesis project. The Arcadis developed fire curve will subsequently be referred to as the *ITFC (Immersed Tube Fire Curve)*. The output of the CFD analysis resulted in a distribution of temperatures in 3D space over

time due to a railcar fire. The points of interest in this project are chosen as those along the ceiling of the structure directly above the fire, as seen in Figure 45.

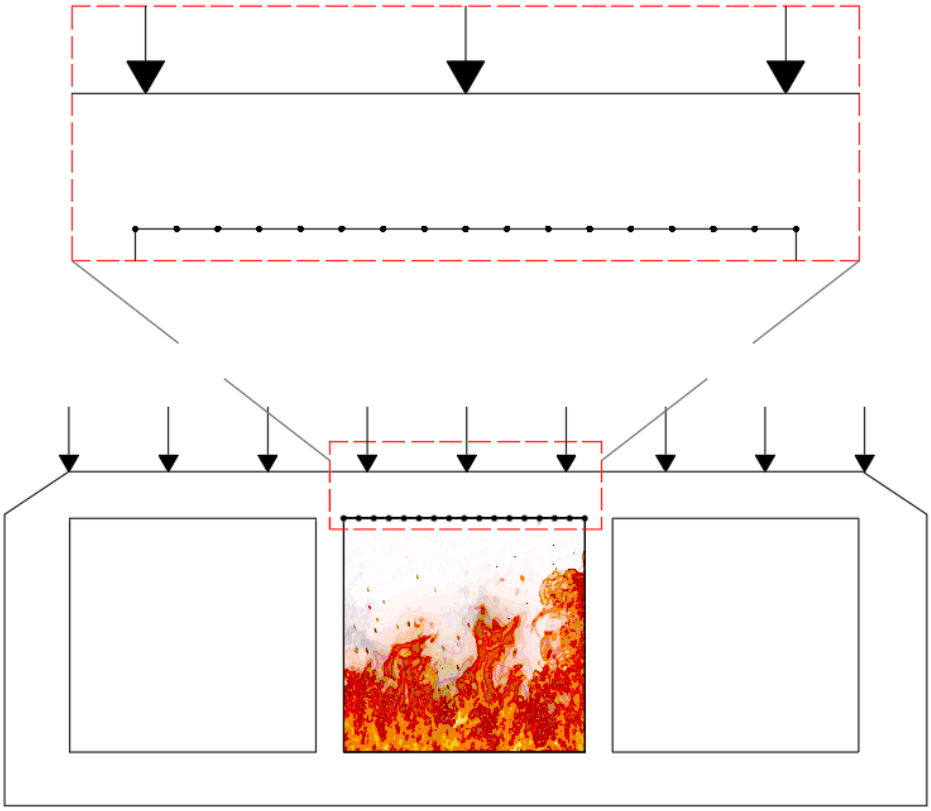

Figure 45: Schematic Representation of Fire Zone and the nodes at which fire temperatures are calculated in the CFD study

The point with the maximum temperature over the duration of the fire lasting 2000 seconds is chosen as the point of interest. The fire curve associated with that point, referred to as the 'critical point', is subsequently applied to the entire bottom face of the roof slab to ensure a conservative approach. The result is the orange curve seen below in Figure 46. The maximum temperature of the concrete as a function of time is determined by making use of the PSFC and the thermal

properties of concrete defined in Section 5.2.2.2. The blue curve in the figure is the maximum concrete temperature as a result of the PSFC.

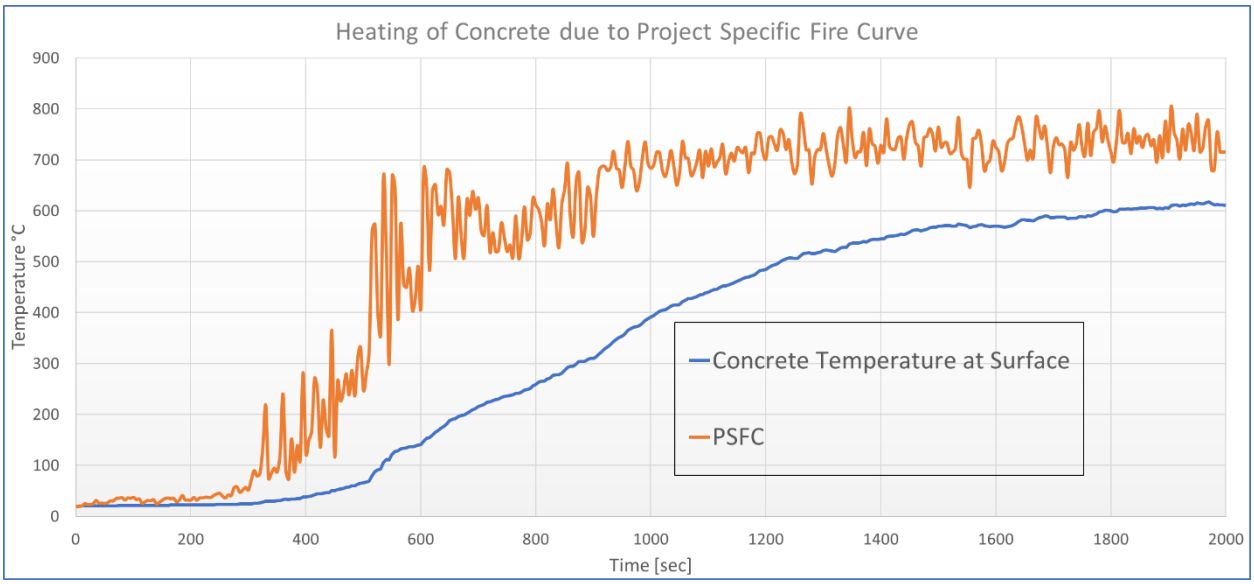

Figure 46: Heating of concrete due to PSFC

The figure above suggests that the PSFC does not begin to significantly affect the concrete until approximately 400 seconds, after which the concrete experiences a steady increase in temperature until 2000 seconds. By assuring the accuracy of the thermal properties of concrete, determining the PSFC, and properly defining the temperature dependency of the mechanical properties of concrete, it is possible to begin an in-depth study into the effects of fires in immersed tubes.

6 CMA in the Finite Element Model

6.1 Goal of this section

The ability to detect CMA in the finite element model described in Section 5 is of particular importance for the execution of this thesis project as a whole. It is also important to understand the factors which govern the extent to which CMA forms within a structure. Therefore, the goal of Section 6 is to properly define the causes of CMA in the finite element model to address the three thesis goals mentioned in Section 3.

6.2 Procedure

Sufficient lateral stiffness is a key requirement in the formation of CMA. Therefore, to induce CMA in the finite element model, a lateral restraint is added by adding an additional support to the right-hand-side tie mentioned in Section 5.1. The lateral restraint provides the necessary lateral stiffness by fully restricting displacements in the lateral direction. Fully restricting the lateral stiffness of the model implies that the structure has infinite stiffness in the lateral direction. This of course is not the case in reality since sources of lateral stiffness are always of a finite nature. The finite nature of the lateral stiffness is addressed in the sensitivity study in Section 9. This section concerns exploring the formation of CMA, and so an infinitely stiff lateral restraint is used.

To more clearly articulate the results of the findings, the following notation is used to describe the different analyses with and without a lateral restraint:

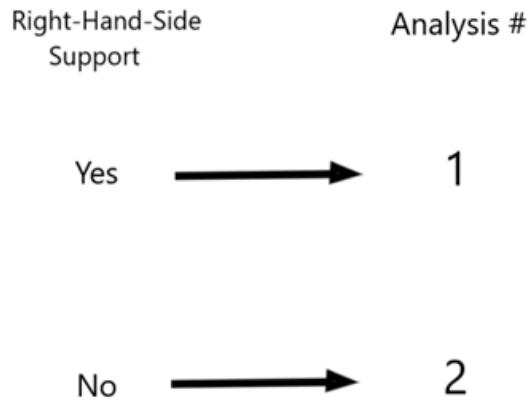

Figure 47: Naming scheme of Analyses 1 and 2

As seen in Figure 47, Analysis 1 includes a lateral restraint at the right-hand-side of the model while Analysis 2 does not. This comparison therefore isolates the effect of the lateral restraint in the model. Analysis 1 and Analysis 2 are each loaded by 4,000 incremental load steps and a load displacement diagram is produced for both analyses. It is hypothesized that significant CMA will be found in Analysis 1 and thus its load displacement diagram will deviate significantly from that of Analysis 2. Furthermore, due to the formation of CMA, it is also hypothesized that the load bearing capacity of Analysis 1 will be substantially higher than that of Analysis 2.

6.2.1 Results of Analysis 1 vs. Analysis 2

The load displacement diagrams of Analysis 1 and Analysis 2 are seen in the figure below. The load displacement diagrams track the vertical displacement of a node on the line of symmetry, seen in Figure 48. This node is chosen to present the midpoint displacement of the roof slab subjected to vertical loading.

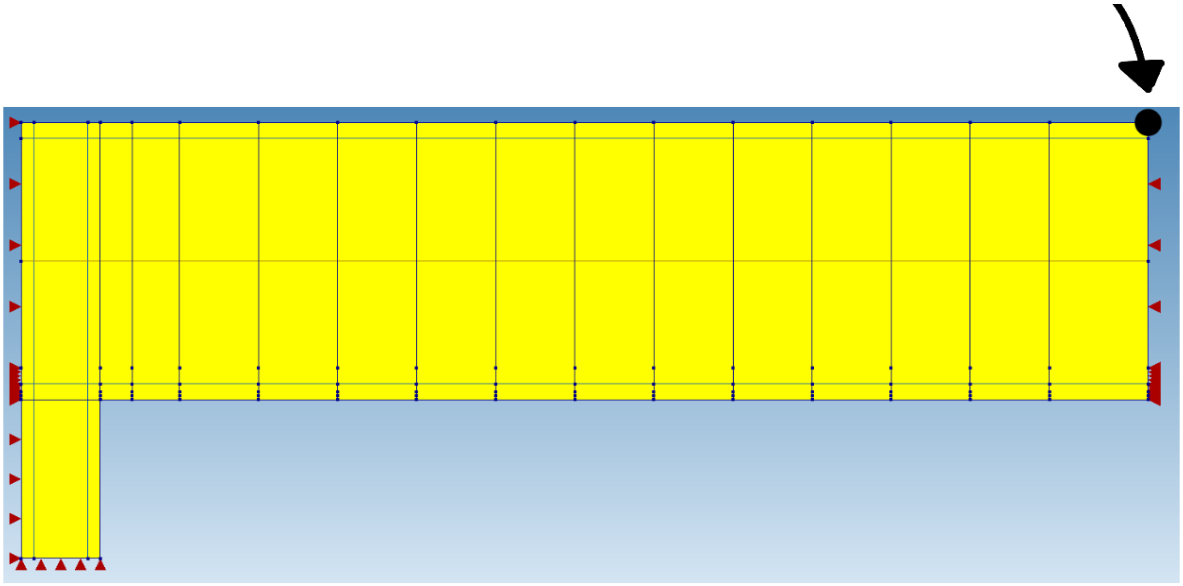

Figure 48: The node, seen in black, tracked throughout the loading process to produce the load displacement diagrams

Both load displacement diagrams as a result of incremental vertical loading are seen in the figure below.

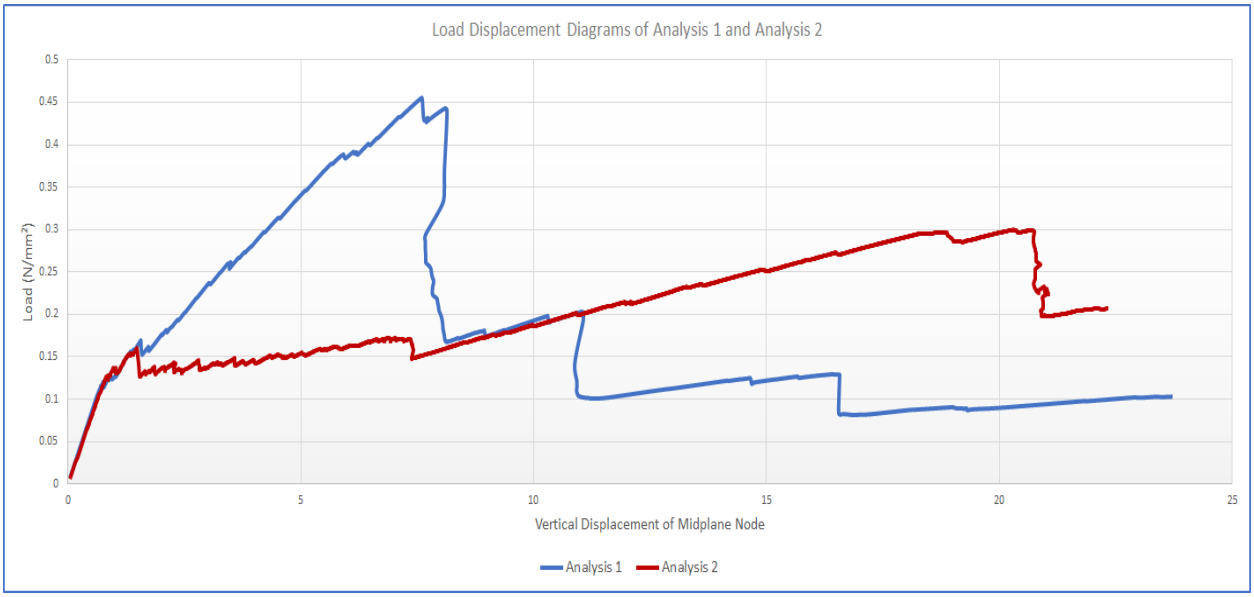

Figure 49: Load Displacement Diagrams | Analysis ½

The load displacement diagrams of Analysis 1 and 2 are almost identical up until a loading of approximately 0.15 N/mm². After that load value, the two analyses begin to diverge in two

significant ways. Firstly, Analysis 1 eventually reaches an ultimate load bearing capacity of 0.45 N/mm² while Analysis 2 has a far lower ultimate load bearing capacity of 0.303 N/mm², a reduction of 33%. Secondly, the shapes of the load displacement diagrams deviate significantly from each other. By comparing the slopes of both load displacement diagrams between 1.5mm and 7.5mm, it is evident that the lateral support in Analysis 1 results in a structure with significantly higher post-cracking stiffness.

The shapes of the load-displacement diagrams show increased stiffness and higher ultimate bearing capacity, consistent with literature regarding laterally restrained and unrestrained slabs, as seen below (25).

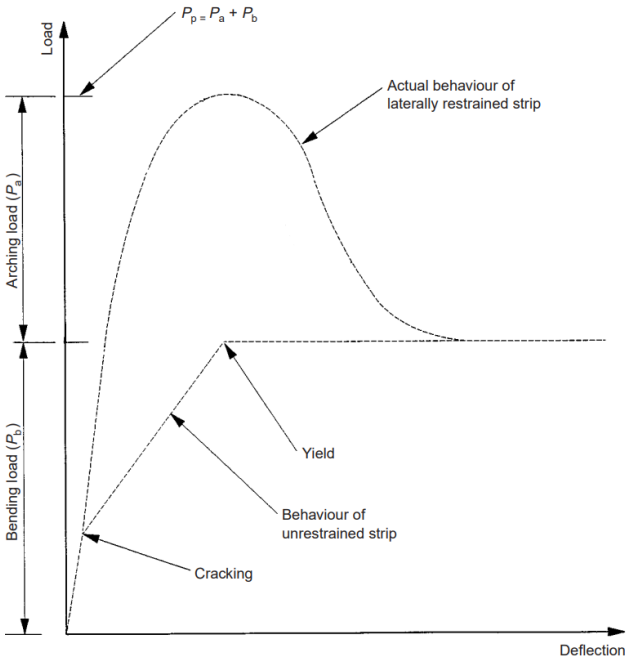

Figure 50: Idealized load-displacement diagrams of restrained and unrestrained concrete slabs

As mentioned earlier in Section 4, verification of finite element models with hand calculations is an essential aspect of the modeling procedure. The hand calculations articulated in Section 4 do not include CMA and are therefore associated with Analysis 2. The load displacement diagrams show the first crack occurring at approximately 0.17 $\frac{N}{mm^2}$ and ultimate bearing capacity is 0.30 $\frac{N}{mm^2}$. These results approach the hand calculations presented in Section 3. The deviations from the ultimate bearing capacity predicted in the hand calculation can be linked to the tensile reinforcement in the roof slab. The hand calculations predict perfect cooperation between the

concrete and the reinforcement, whereas the finite element analysis shows debonding before the yield plateau is reached.

To investigate the presence of CMA in Analysis 1, the cracking pattern and the in-plane stress components at peak loading are shown below.

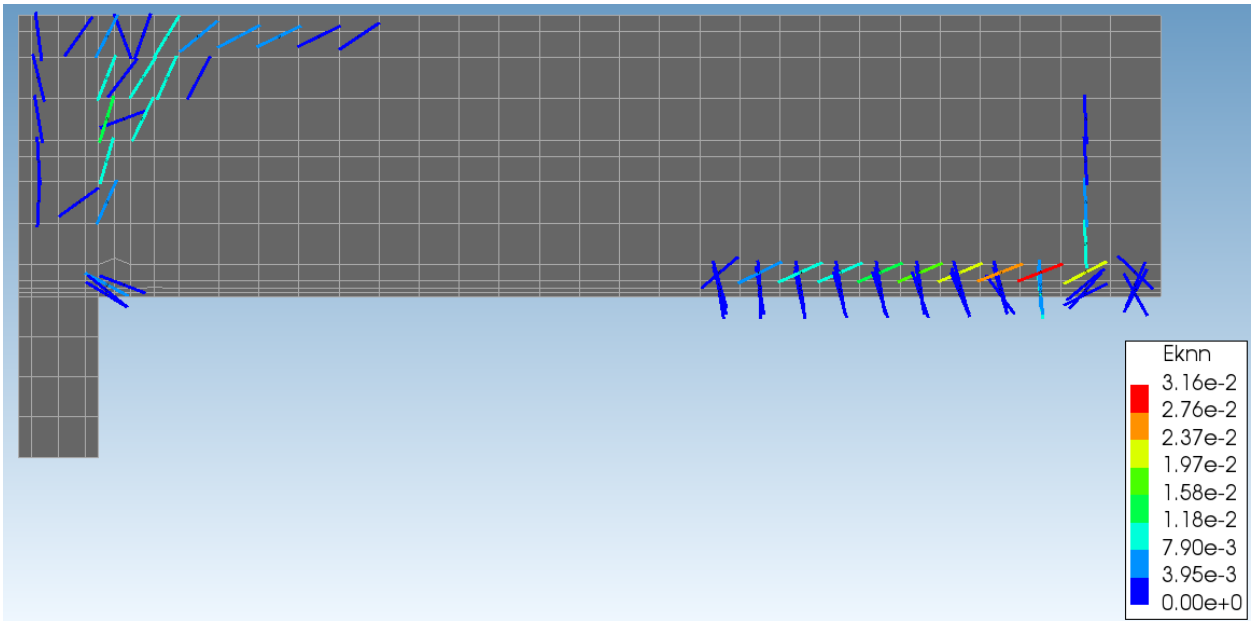

Figure 51: Cracking pattern of Analysis 1 at peak loading

The cracking has occurred in tensile areas of the roof slab due to loading and is therefore an expected result. As mentioned in Section 2.2, a requirement of CMA is cracking, which allows for the redistribution of internal forces, resulting in the compressive arches. The redistribution of the internal forces can be seen in the figure below, which represents the in-plane stress components of Analysis 1 at peak loading.

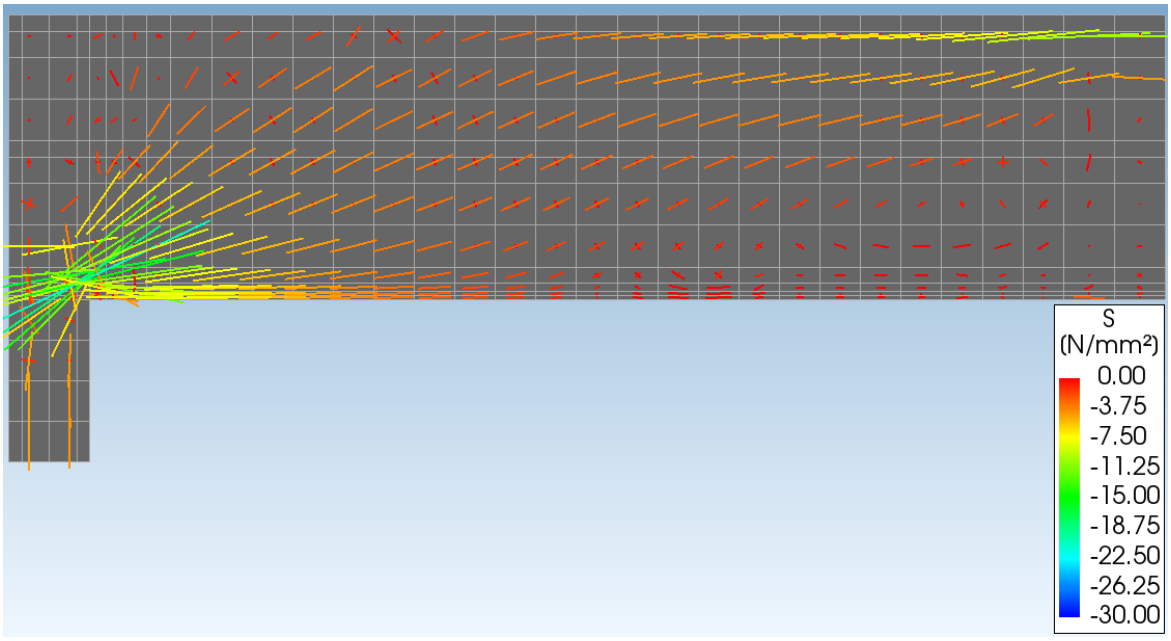

Figure 52: Analysis 1 in-plane stress components at peak loading

The in-plane stress components of Analysis 1 are presented in Figure 52 above. The stress components of Analysis 2, where CMA is not expected, is seen in Figure 103 in Section 12.7. In the above figure, the compressive strut extending from the bottom of the left support to the top of the midplane of the roof slab is clearly visible. These in-plane stress components correlate to the expected internal force development typically associated with CMA, as seen below (25).

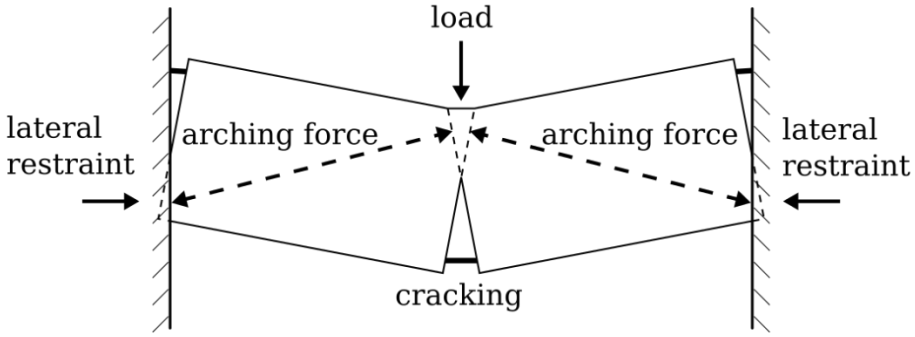

Figure 53: Internal compressive struts associated with CMA

By examining the load displacement diagrams and considering the failure mechanisms seen in Figure 52 it is evident that CMA indeed exists in Analysis 1. The implication is that the lateral restraint provided by the support at the right-hand-side of the model provides the necessary lateral stiffness to induce CMA in the model.

7 Question 1

How does thermal degradation of concrete's compressive strength affect the formation of CMA in an immersed tube roof slab subjected to fire?

7.1 Goals of this section

This section seeks to quantify the effect of the temperature dependency of the compressive strength of concrete on the development of CMA and the ultimate bearing capacity of the structure. It is speculated that the thermal degradation of the compressive strength of concrete as described in Section 5.2.2.1 can have a detrimental effect on the development of CMA and the ultimate bearing capacity. Therefore, this section addresses the degradation of concrete due to fire and that degradation's effect on the formation of CMA in the finite element model.

7.2 The Effect of Thermal Degradation on CMA

It has been established that the support at the right-hand-side induces CMA in the finite element model. To answer the first question of the thesis project, *whether or not the temperature dependent compressive strength of concrete affects the development of CMA during a fire situation*, it is necessary to introduce the dependence of the concrete's compressive strength on temperature to the analyses. That dependence is studied by introducing two new analyses. The first analysis, called *Analysis 3* is identical to Analysis 1 except that the concrete compressive strength defined in the model is temperature independent. The second new analysis, called *Analysis 4*, is identical to Analysis 2 except that compressive strength of the concrete defined in the model is temperature independent. The updated notation can be seen below in Figure 54.

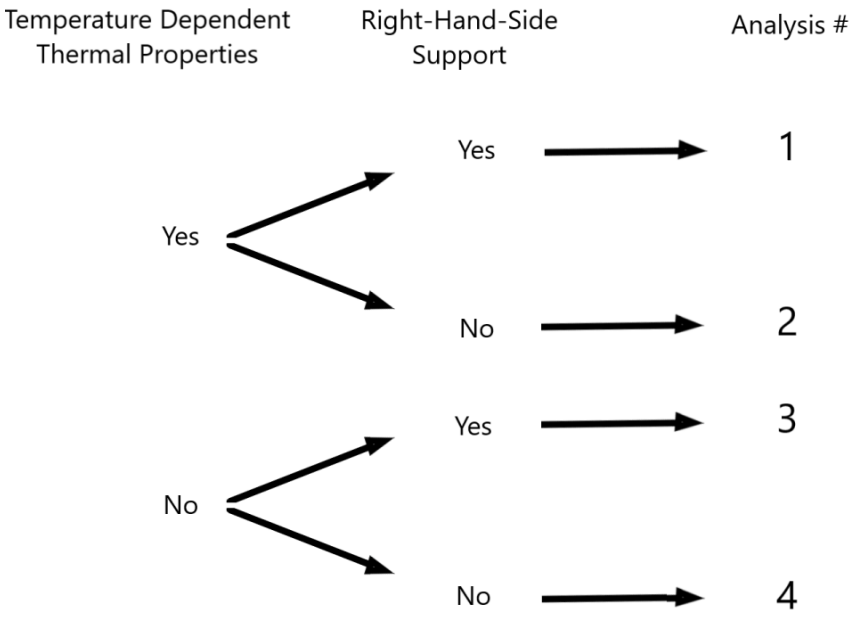

Figure 54: Labelling of finite element models

In each of the analyses described in Figure 54, several intervals of the fire curve are applied to the model, followed by the incremental vertical loading. Therefore, each analysis (1-4) contains the following calculations:

- Incremental vertical loading
- 900 seconds of The PSFC followed by incremental vertical loading
- 1000 seconds of The PSFC followed by incremental vertical loading
- 1100 seconds of The PSFC followed by incremental vertical loading
- 1200 seconds of The PSFC followed by incremental vertical loading
- 1300 seconds of The PSFC followed by incremental vertical loading
- 1400 seconds of The PSFC followed by incremental vertical loading
- 1500 seconds of The PSFC followed by incremental vertical loading
- 2000 seconds of The PSFC followed by incremental vertical loading

By subjecting the finite element model to increasing durations of the PSFC before loading, the ultimate bearing capacity of the roof slab can be evaluated as a function of the duration of the PSFC.

Comparing the ultimate bearing capacity of the models will establish the influence of temperature dependent compressive strength of concrete. The figures below show the ultimate bearing capacity of all four analyses after each duration of fire exposure. The load displacement diagrams are available in Section 12.2.

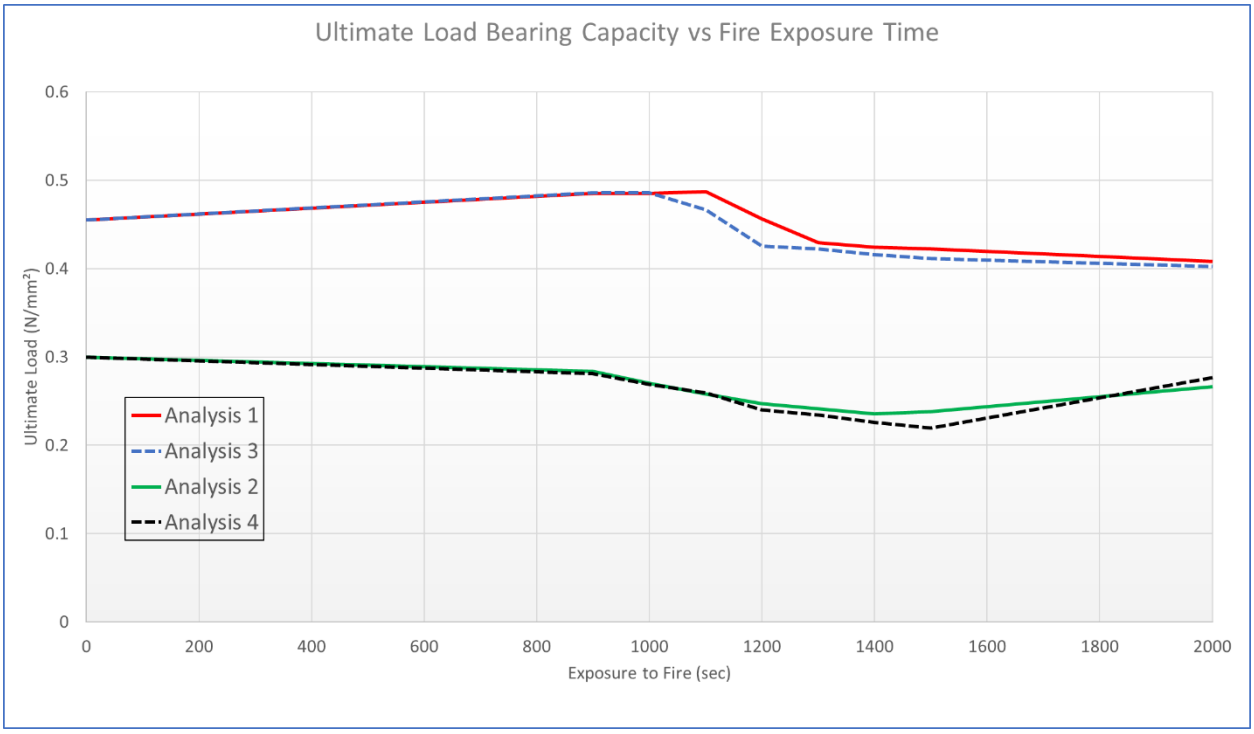

Figure 55: Ultimate Load Bearing Capacity vs Fire Exposure Time

Comparing the ultimate bearing capacities of Analysis 1 with Analysis 3 and Analysis 2 with Analysis 4 results in the conclusion that the ultimate bearing capacities of the analyses are not significantly affected by fire exposure. This can be seen in the figure as the ultimate bearing capacities of the models are not significantly reduced throughout the fire exposure. This result can be explained by examining the stress buildup during loading without the influence of the ITFC and comparing it to the strength of thermally degraded concrete.

To further investigate the failure mechanism, the softening behavior of the nodes in Analysis 1 without temperature influence are shown below. Three figures are shown below. The first figure shows the contour plot of principle stresses at ultimate loading. A significant buildup of stresses

can be seen in the bottom left corner of the beam. The second figure shows the elements which have failed, defined as having a principle strain greater than $\varepsilon_{cu} = 0.0058$, at peak loading. The second figure shows nodes which have entered the softening domain of the compression curve at peak loading. The percentage associated with each node is presented in the figure. The percentage is the amount of softening experienced, where ε_{c1} is defined as 0% and ε_{cu} is defined as 100%. It is important that some nodes are highlighted both for failure and softening. The reason for this is that the stresses are evaluated at the interpolation points. The nodes highlighted are those closest to the interpolation point. Therefore, a single node can be the closest to several integration points.

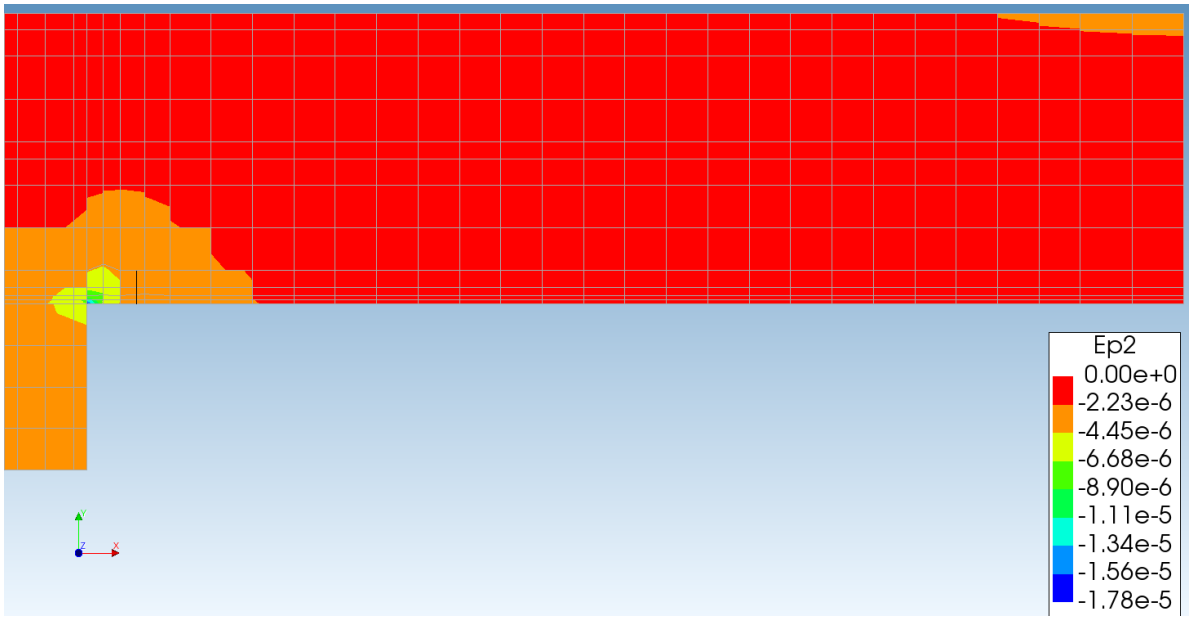

Figure 56: Contour plot of principle compressive stress at ultimate loading

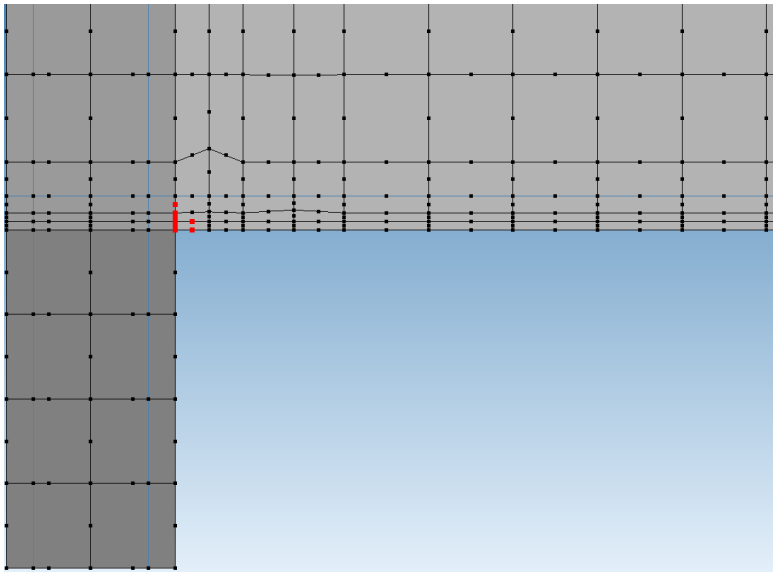

Figure 57: Analysis 1 - Failed Elements at Peak Loading

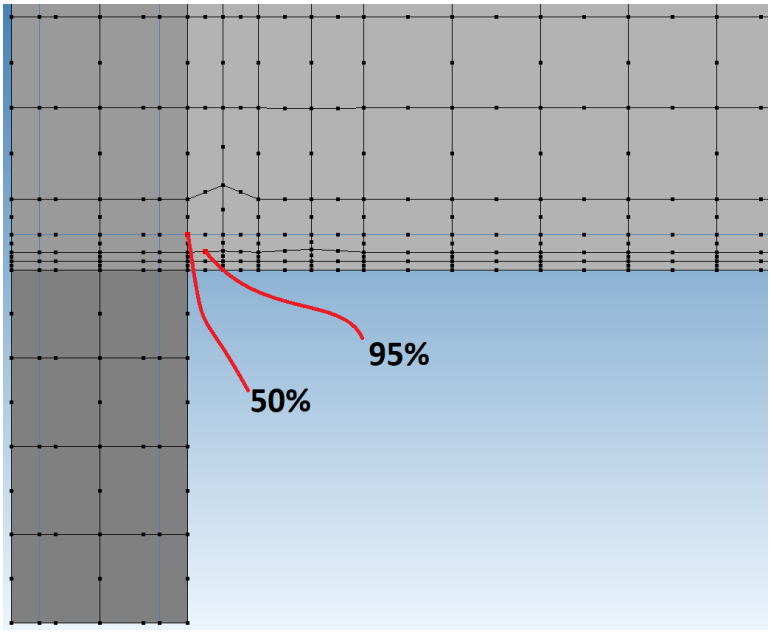

Figure 58: Analysis 1 - Elements experiencing softening at ultimate load

The above figures demonstrate the failure mechanism associated with models experiencing CMA. The compressive strut developed during loading reaches a peak value and fails in the bottom of the left support. The concrete at that region experiences crushing and the angle of the compressive strut subsequently reduces as the left side of the strut moves upwards, lessening the contribution of CMA.

The results after 2000 seconds of fire are similar to the results without the presence of fire. Below, the elements which experience failure after 2000 seconds of fire at the ultimate load are shown below.

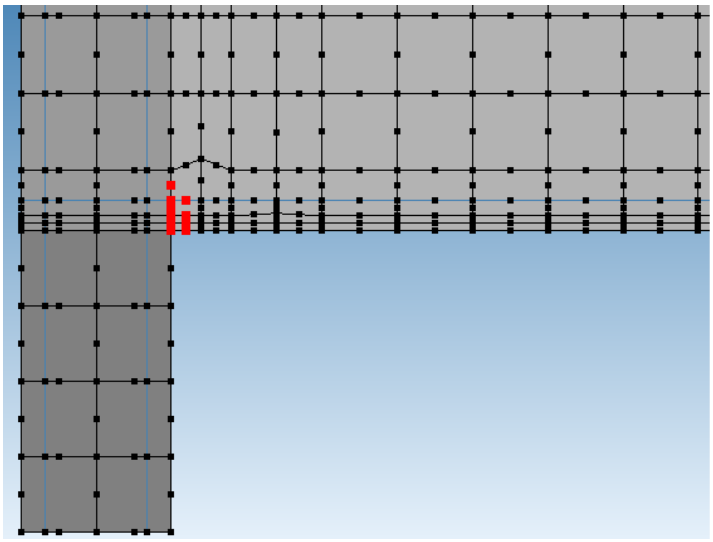

Figure 59: Analysis 1 after 2000 seconds fire exposure - failed nodes

The figure above shows approximately the same elements failing as in the situation without temperature. Furthermore, the elements which experience softening are shown below. The percentage is the amount of softening experienced, where ε_{c1} is defined as 0% and ε_{cu} is defined as 100%.

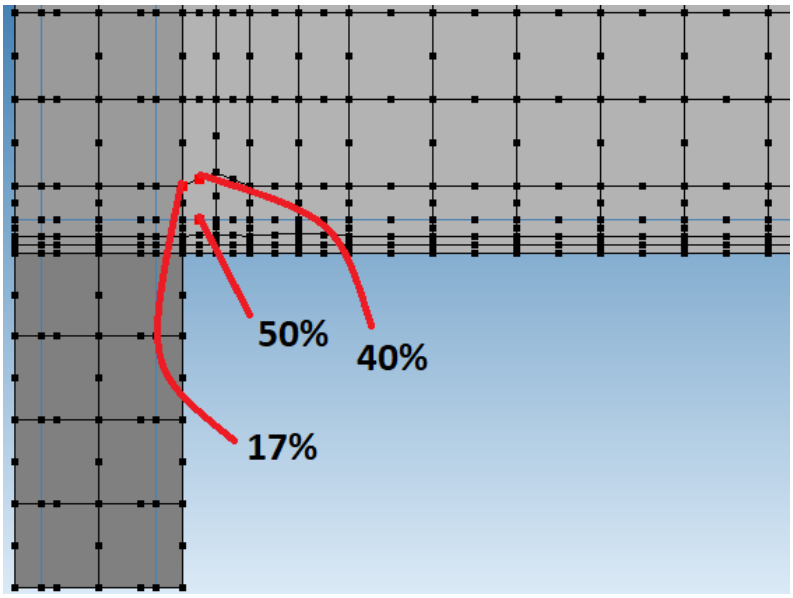

Figure 60: Analysis 1 after 2000 seconds of fire exposure - softening of nodes at ultimate load

Again the results are similar to the case without fire exposure. These results further show that the PSFC does not influence the behavior or the ultimate bearing capacity of the roof slab.

7.3 Discussion

This section quantifies the effect of concrete's temperature dependent compressive strength on the ultimate bearing capacity of the structure. Two new analyses are developed Analysis 3 and Analysis 4, whose material properties are temperature independent. By subjecting both models to the PSFC followed by incremental vertical loading, the effect of concrete's temperature dependent compressive strength is isolated and studied. By examining the ultimate bearing capacities, cracking patterns, and in-plane stress components, it is concluded that the ITFC is not severe enough to restrict the formation of CMA and thus does not have a significant impact on the ultimate bearing capacity of the structure.

7.4 Question 1 Conclusion

By applying the PSFC to Analysis 1 for 2000 seconds, it is concluded that the PSFC does not significantly reduce the ultimate bearing capacity of the structure. This conclusion can be drawn from Figure 55, where the ultimate bearing capacities after different durations of fire exposure is shown. It is clear from the figure that the ultimate bearing capacity of the structure is not significantly affected by the PSFC.

Furthermore, by comparing the ultimate bearing capacities as functions of fire exposure time, it is evident that the analyses with lateral restraint (Analysis 1 and Analysis 3) and without lateral restraint (Analysis 2 and Analysis 4) exhibit nearly identical strengths throughout fire exposure regardless of the compressive strength dependence on temperature, which further suggests that the thermal degradation of concrete is not of substantial influence of the structure's ultimate bearing capacity.

8 Question 2

How does spalling influence the formation of CMA and the ultimate bearing capacity of an immersed tube?

8.1 Goals of this section

This section focuses on the influence of concrete spalling on the both the formation of CMA and the ultimate bearing capacity of the roof slab. Since concrete spalling results in loss of structural material and a reduction of cross-section, it is theorized that the spalling due to the PSFC could have a detrimental effect on the structure's ability to form the arching compressive struts necessary for CMA and therefore the ultimate bearing capacity.

To determine the effect of spalling, a spalling velocity due to the PSFC must be established to quantify the spalling depth over time. The expected spall depth can then be removed from the structure followed by the application of an incremental vertical load equivalent to that in Section 7. The result of vertical loading of the spalled section is compared to similar loading of the unspalled section to isolate the effect of spalling on the formation of CMA and the ultimate bearing capacity of the structure.

8.2 Spalling in Concrete

As mentioned in the literature study, spalling is a phenomenon whereby medium to large sections of concrete are suddenly and violently detached from the main structure during its service life. This behavior has been well established in experiments and has been observed extensively in structures subjected to fire conditions. The rate at which the cross-section of a structure is reduced due to spalling is known as the spalling velocity, typically measured in mm/min. The prediction of the spalling velocity, even when the fire curve is known, has been the subject of extensive literature and is still very difficult to accurately predict. In this thesis project, a method for predicting the spalling velocity is presented in Section 8.3. The spalling velocity is subsequently

used to remove the spalled concrete from the finite element model to study its implications on the formation of CMA and ultimate bearing capacity.

8.3 Method for Establishing the Spalling Velocity

Accurately predicting the spalling velocity is necessary to remove the proper depth of spalled concrete material from the finite element structure. The spalling velocity prediction for concrete slabs subjected to the PSFC is based on previous experiments conducted by the Austrian Ministry for Transport, Innovation, and Technology. The study subjected concrete slabs to the RWS fire curve and measured the spalling velocities (26).

The RWS curve is a fire curve developed in the Netherlands and is used extensively in tunnels underneath open water (1). The goal of the RWS curve is to simulate a petrol truck carrying 45,000 liters of gasoline, resulting in a fire load of 300 MW. The curve has a peak temperature of 1350°C and does not include a cooling phase. Due to the RWS Curve's widespread usage in design, it is also the focus of many research initiatives involving its causing of spalling in concrete structures. The RWS curve is fully described by Table 3 below.

Table 3: Temperature of RWS fire-curve over time

Time (min)	Temperature (°C)
0	20
3	890
5	1140
10	1200
30	1300
60	1350
90	1300
120	1200

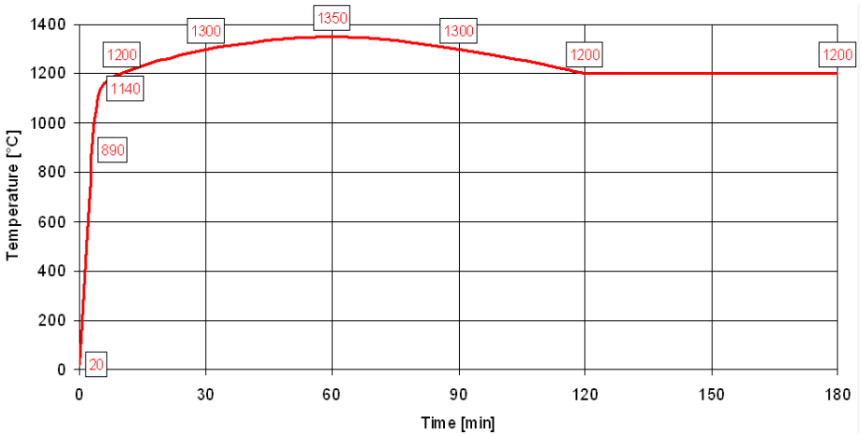

Figure 61: RWS Fire Curve

The method used in this thesis project predicts spalling velocities by examining the results of the RWS fire test. The penetration rate of different temperatures in the concrete material over time due to the fire curve is determined by applying the RWS curve to the finite element model. The goal is to find the specific temperature whose penetration speed into the concrete most closely matches the spalling velocity demonstrated in the Austrian study. That same temperature's penetration is calculated for the PSFC, and the penetration rate of that temperature is taken as the spalling velocity. This step is expanded upon in Section 8.4.

This method for estimating the spalling velocity is discussed in Section 11.

8.4 Temperature Penetration Rates from RWS Fire Exposure

The RWS curve is applied to Analysis 1 for a duration of 120 min. The temperature penetration due to the RWS fire-curve after 120 minutes of fire exposure is seen below in Figure 62.

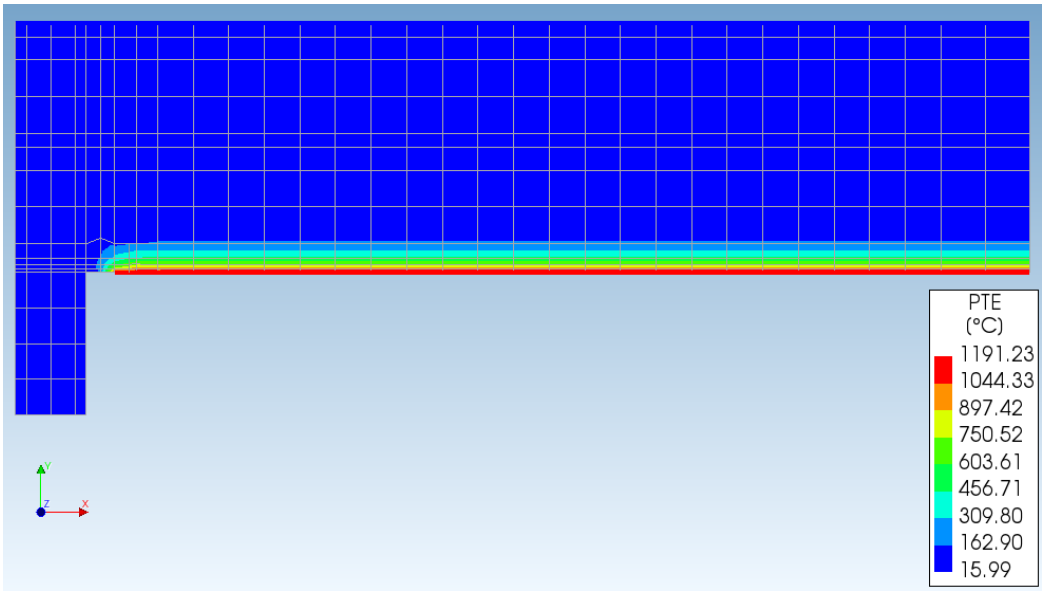

Figure 62: Temperature penetration of RWS curve in concrete roof slab after 120 minutes

Temperature penetration rates are subsequently developed by producing contour probes for different moments in time. The penetration rates for several temperatures are shown below in Figure 63.

Figure 63: RWS Penetration speeds in concrete with temperature dependent compressive strength

Figure 63 represents the deepest point in the roof slab that specific temperatures can be found in the concrete as a function of time. The figure shows that the lower temperatures penetrate more quickly than higher temperatures, as is expected. Also, it is clear from the figure that higher temperatures take longer to appear in the structure, which is another expected result. It can be established that the spalling velocity found by the Austrian Ministry for Transport, Innovation, and Technology, shown as a black dashed line in the figure, closely resembles the penetration speed of 150°C. In this thesis report, it is proposed that the 150°C penetration speed can be used to predict the spalling velocities resulting from different fire curves. The next step in determining the spalling velocity due to the PSFC is to determine the 150°C penetration speed resulting from the PSFC.

8.5 Temperature Penetration Curves for PSFC

The PSFC is applied to Analysis 1 for a duration of 2000 seconds. The temperature of the roof slab after 2000 seconds of exposure to the PSFC is seen below in Figure 64.

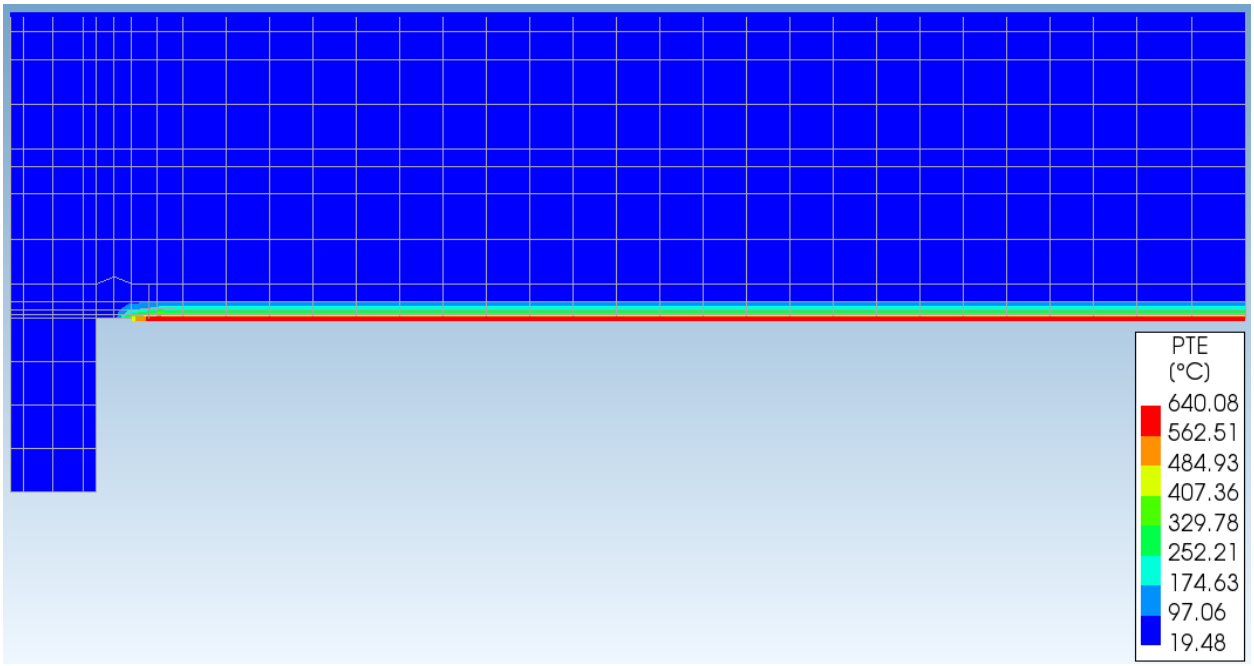

Figure 64: Temperature penetration after 2000 seconds of PSFC

Similarly to Section 8.4, temperature penetration curves resulting from the exposure to 2000 seconds of the PSFC are produced, with the 150°C penetration curve shown below in Figure 65.

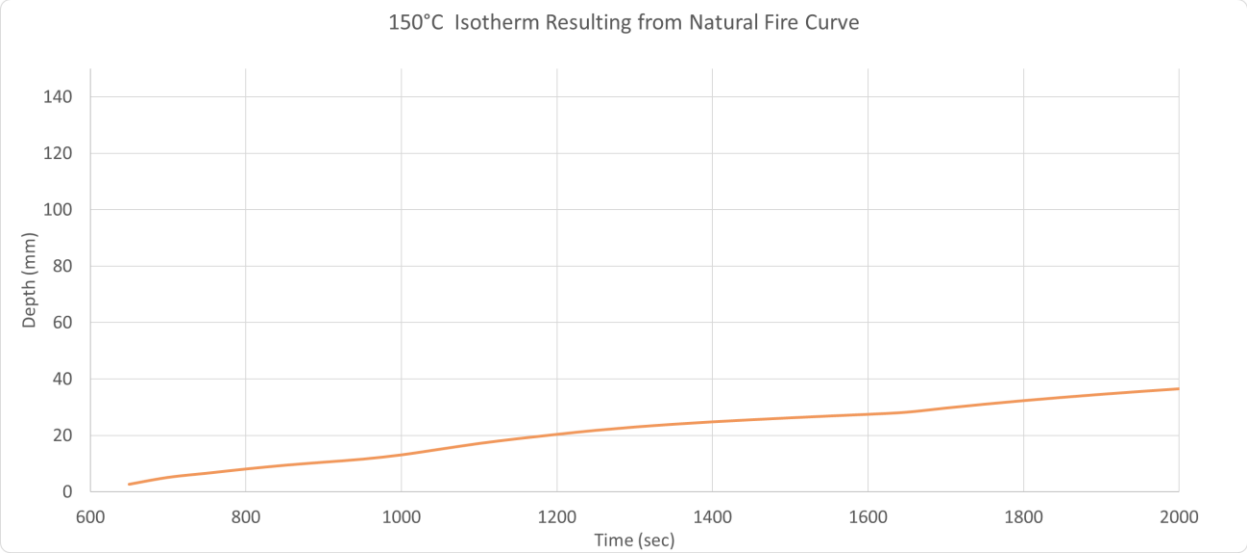

Figure 65: RWS Penetration speeds in concrete with temperature dependent compressive strength

Figure 65 above shows the 150°C penetration into the concrete resulting from the PSFC. Following the method presented in Section 8.4, this speed is used to establish the spalling velocity of the roof slab of an immersed tube subjected to the PSFC. Therefore, Figure 65 implies a spall-depth of 36.5 mm after 2000 seconds of fire exposure. A section with height 36.5 mm can therefore be removed from the main structure to simulate 2000 seconds of spalling. An incremental vertical load is subsequently applied to the model to evaluate the effect of spalling on the buildup of CMA and the ultimate bearing capacity. The spalled section is seen below in Figure 66.

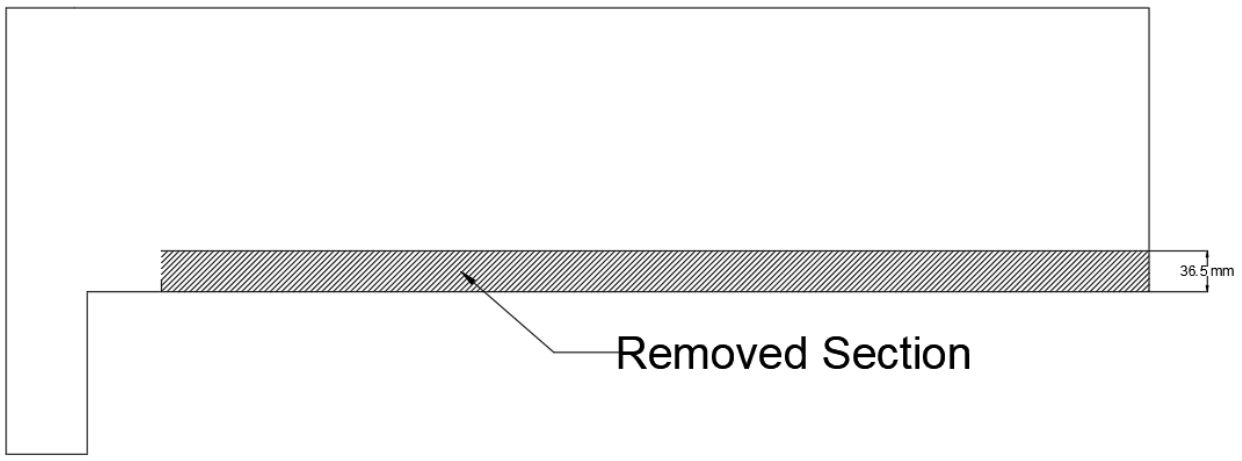

Figure 66: Spalled cross-section after 2000 seconds of the PSFC

The hatched area of the figure represents the concrete removed from the structure. It is important to note that at 150°C, concrete retains 95% of its compressive strength when compared to room temperature (20°C), as seen in Figure 67 . Therefore, when removing the spalled concrete, it is not necessary to take the thermal degradation of the newly exposed layer into account.

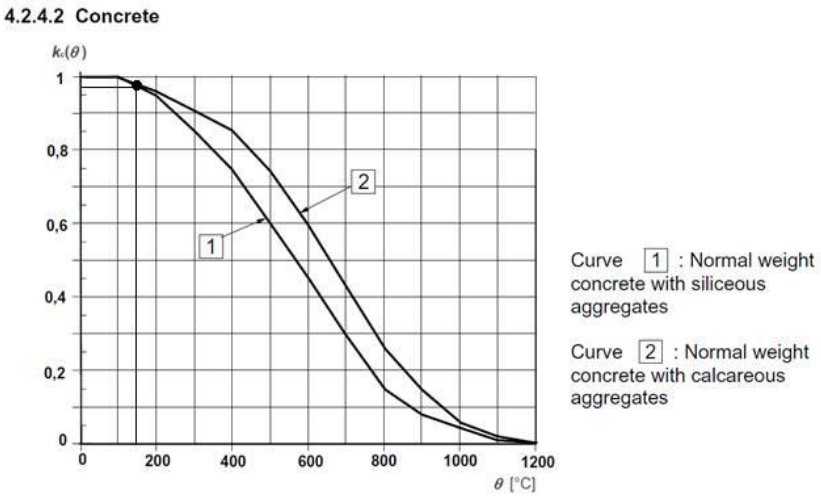

Figure 67: Thermal degradation of concrete compressive strength as a function of temperature [NEN 1992-1-2]

8.6 Results of Spalled Section

The spalled roof slab is loaded in the vertical direction in 4,000 load-steps. The load displacement diagram of the spalled section is seen in Figure 68 below. The load displacement diagram of the unspalled section is included for comparison. Comparing the load displacement diagrams of the two analyses gives an overview of the structural response and the ultimate bearing capacity of each model.

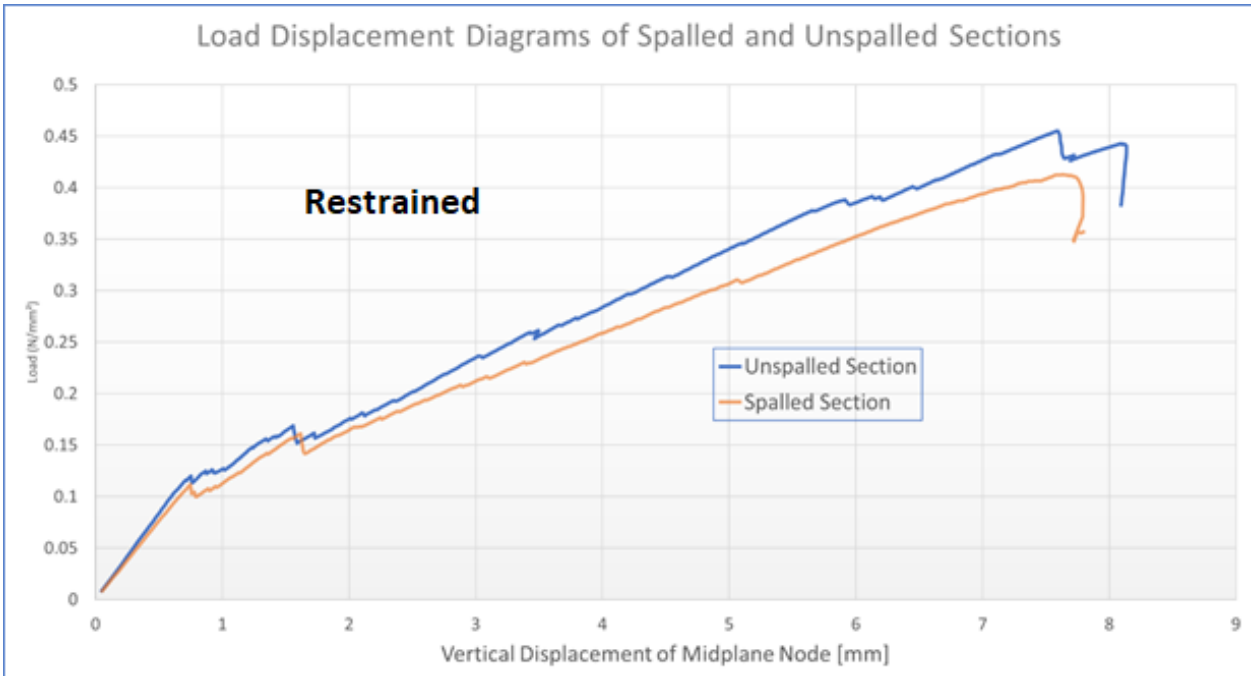

Figure 68: Load displacement diagrams of restrained spalled and unspalled sections

The load displacement diagrams of the spalled and unspalled roof slab are presented in Figure 68. Both analyses are restrained. The load displacement diagrams show two important results. The first result is that the two load displacement diagrams follow approximately the same shape throughout the loading procedure. The unspalled section is slightly stiffer, which is visible between 1.5mm and 7.5mm on the displacement-axis. This is an expected result due to the decrease in the moment of inertia in the spalled section. The second important result is that the two analyses have a similar ultimate bearing capacity. The spalled section has 93% of the load bearing capacity of the unspalled section. This reduction is not completely insignificant, but the proximity of the two results indicates a high probability that the mechanism of CMA has not been jeopardized. To investigate the buildup of CMA in the spalled section, the in-plane stress components are presented.

The in-plane stress components are presented in Figure 69 below. The in-plane stress components are taken at the point of peak loading, as characterized by the load displacement diagram shown above in Figure 68.

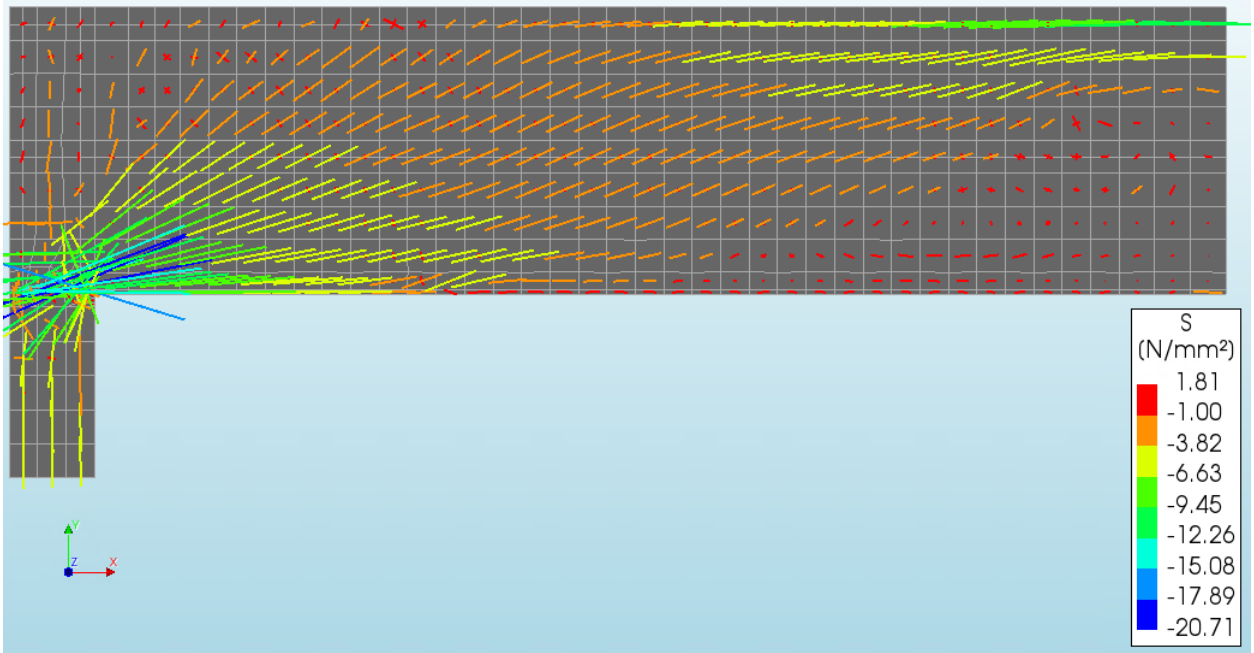

Figure 69: In-plane stress components of spalled section at peak loading

Figure 69 shows the in-plane stress components of the spalled section at the moment of peak loading. A compressive strut extending from the bottom of the left support to the top of the midplane of the roof slab is visible. The successful buildup of the compressive strut provides the justification for the similar shape of the load displacement diagrams of the spalled and unspalled sections presented in Figure 68. The implication is that CMA indeed is able to form in the spalled section.

The buildup of the compressive struts in the spalled roof slab can be explained through the typical mechanism of CMA. Significant deformations and tensile cracking cause a hinge to form in the lower region of the left-hand-side support. With increased vertical loading, the force is transferred from the top of the beam downwards to the hinge, forming the compressive strut associated with CMA. The arch shape of the strut offers increased ultimate bearing capacity to the structure. The crack strains of the beam at peak loading are presented below in Figure 70.

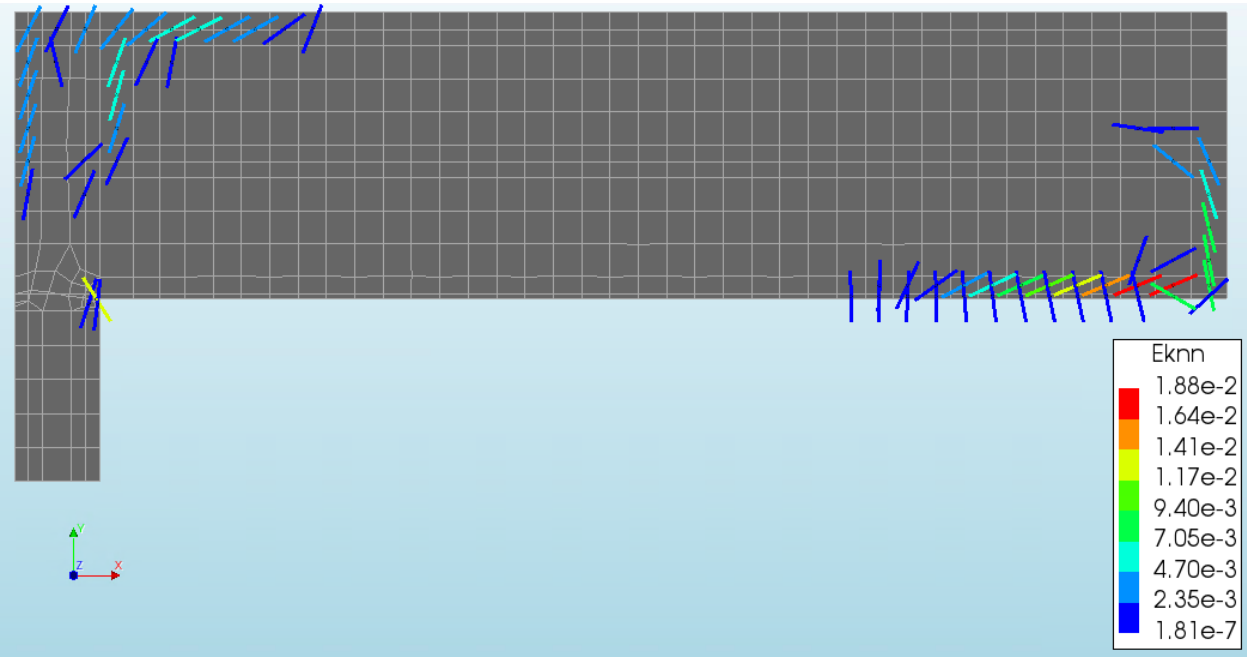

Figure 70: Crack pattern of spalled section at peak loading

The cracks at the top of the left-hand-side support are visible in the figure above. This cracking allows for the redistribution of internal forces and the subsequent development of the compressive struts commonly associated with CMA, as described in Section 6. The in-plane forces in the spalled roof slab which form a compressive strut as a result of the cracking pattern suggests that spalling does not significantly influence the formation of CMA or the ultimate bearing capacity in the roof slab of an immersed tube.

8.7 Discussion

This section quantified the impact of spalling due to the PSFC on the ability for CMA to form in the roof slab of an immersed tube. The first step of determining the influence of the spalling is to establish the spalling velocity resulting from the PSFC. The method used to find the spalling velocity involved referencing experimental spalling data resulting from the RWS curve. The temperature whose penetration into the concrete closely resembles the spalling velocity is established and subsequently used to estimate the spalling velocity due to the PSFC.

By estimating the spalling velocity as a result of the PSFC, the expected spalled zone of 36.5 mm after 2000 seconds is removed from the finite element model to simulate the reduction in cross section due to spalling. The spalled section is then incrementally loaded in the vertical direction to produce the load-displacement diagram presented in Figure 68. The load displacement diagram showed a similar structural response between the spalled and unspalled sections. The presence of CMA in the spalled section is then demonstrated by presenting the in-plane stress components and crack strains at peak loading.

The implications of using this method to predict the spalling velocity resulting from the PSFC is further discussed in Section 10.

8.8 Question 2 Conclusion

The effect of spalling on the formation of CMA and the ultimate bearing capacity of a roof slab in an immersed tube is established in this section. The depth of the spalled section is determined through an estimation of the spalling velocity based on experimental data. By removing the anticipated spalled section and applying the same loading applied on the unspalled section, the effect of spalling is effectively isolated and studied.

The load displacement diagrams of both spalled and unspalled roof slabs presented in Figure 68 showed similar structural behavior, but a reduction of 7% in the ultimate bearing capacity over the course of the ITFC. The presence of CMA in the spalled section is confirmed in Figure 69, in which the in-plane stress components of the spalled roof slab at peak loading are examined. The figure showed a clear formation of the compressive struts associated with CMA. Furthermore, the crack strains presented in Figure 70 show the typical cracking pattern common with the formation of CMA, providing further indication of CMA in the spalled roof slab. These results suggest that spalling does not have a significant effect on the ability of a roof slab in an immersed tube to develop CMA but does cause a decrease in its ultimate bearing capacity.

9 Question 3

How does lateral stiffness affect the formation of CMA and the ultimate bearing capacity of the immersed tube roof slab?

9.1 Objective of sensitivity study

As discussed in Section 2.2, sufficient lateral restraint is necessary to induce CMA in a reinforced concrete slab (27). This requirement for CMA is demonstrated in Section 6.2.1, where it is shown that the inclusion of a support at the right-hand-side of the finite element model induces significant CMA, whereas the model without the support did not. However, roof slabs in immersed tubes in the real world are restrained laterally mainly by soil and by the surrounding structure. In this thesis, the lateral stiffness is studied through the use of a sensitivity analysis. The roof slabs are restrained by linear springs with non-zero finite stiffness values. The roof slab will then be incrementally loaded in the vertical direction similarly to the loading in previous sections. The load displacement diagrams and the internal forces in models with different stiffnesses are examined and compared to isolate the contribution of lateral stiffness to the formation of CMA and the ultimate bearing capacity.

9.2 Finite element representation model

To model the effect of lateral stiffness, the finite element model is modified to include a spring boundary interface. A representation of the updated model to include finite lateral stiffness is seen below in Figure 71. The updated model includes a spring on the right-hand-side and a tie at the upper-right-hand node of the model prevents rotations of the midplane, a condition of symmetry.

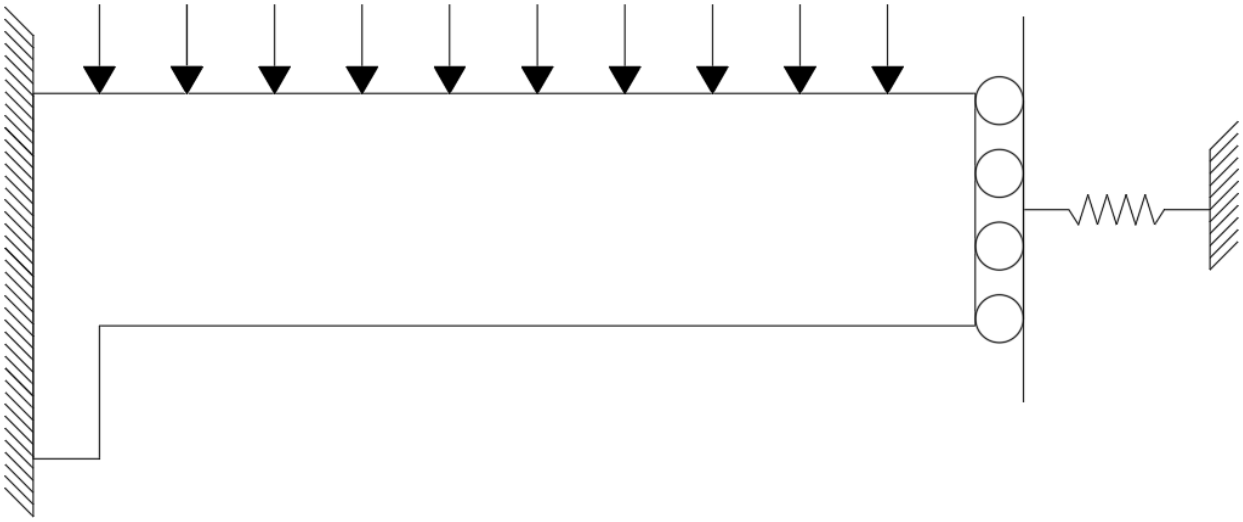

Figure 71: Schematic representation of updated finite element model to include finite lateral stiffness

9.3 Spring Stiffnesses Studied

To effectively quantify the influence of the spring stiffness on the formation of CMA, eight different spring stiffnesses are studied. The specific stiffnesses studied are chosen by examining the results of Analysis 1 and Analysis 2, which represent infinite and zero lateral stiffness respectively. In Analysis 1, the right-hand-side support leads to significant buildup of normal force in the structure during the vertical loading procedure. No such support exists in Analysis 2, implying that the right-hand-side of the roof slab is free to move in the lateral direction.

The maximum normal force developed during loading in Analysis 1 is plotted against the maximum lateral displacement during loading of Analysis 2. A line connecting the two is drawn. Thus, a linear relationship is established for the relation between the amount of lateral displacement and normal force development due to loading.

The linear spring stiffnesses are chosen based on percentages of lateral displacement of Analysis 3. For example, a 50% lateral displacement implies that the model should move 50% the maximum lateral displacement in Analysis 3. With a linear relationship established between the lateral displacement and the normal force development, the normal force associated with 50% lateral displacement is thus known. By dividing the normal force with the lateral displacement, the linear

stiffness is obtained. Figure 72 below shows the procedure described to find the linear spring stiffnesses used in the sensitivity study.

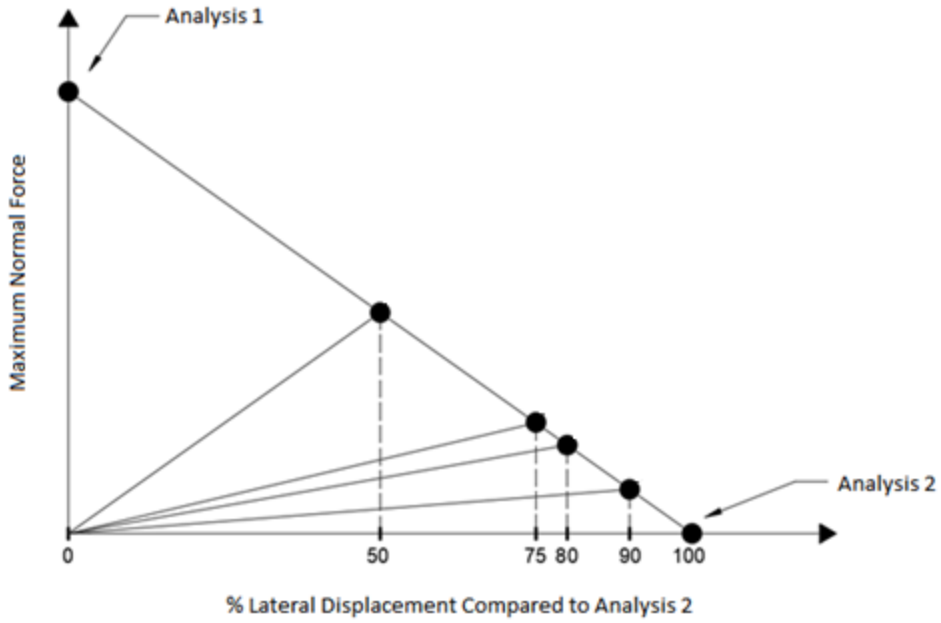

Figure 72: Spring stiffness values based on percentage of lateral displacement

The linear spring stiffnesses can be converted to an equivalent soil stiffness by making use of the model geometry described in 5.1. The equivalent soil stiffness is calculated by dividing the linear stiffness value by both the height of the roof slab [875 mm] and the thickness [1 mm]. An overview of the linear spring stiffnesses and the equivalent soil stiffness is presented in Table 4 below. The first four values derived from the method above. The following four values are added to provide more data points and to give a more accurately quantify the effect of stiffness on ultimate bearing capacity and CMA.

Table 4: Lateral stiffnesses investigated in sensitivity study

% of Lateral Displacement of Analysis 3	Linear Spring Stiffness K ($\frac{N}{mm}$)	Equivalent Soil Stiffness ($\frac{N}{mm^3}$)
50	664	0.76
75	221	0.25
80	166	0.19
90	74	0.08
N/A	230	0.26
N/A	460	0.53
N/A	572	0.65
N/A	685	0.78

With the spring stiffnesses determined for each of the eight models, an incremental vertical load is applied to each, in a manner similar to that of previous sections. The load displacement diagrams and in-plane stress diagrams associated with each model are examined to isolate the effect of linear spring stiffness. It is hypothesized that the increase in spring stiffness will increase the ultimate bearing capacity and facilitate greater buildup of CMA.

9.4 Results Diagrams of Sensitivity Study

The eight models with increasing spring stiffness are each loaded incrementally in the vertical direction. The load displacement diagrams of the first four models Table 4 are presented below in Figure 73. The load displacement diagrams of all eight models can be found in Section 12.2 Figure 98. Since the PSFC proved not to be a significant influence, the study is conducted without the effect of fire.

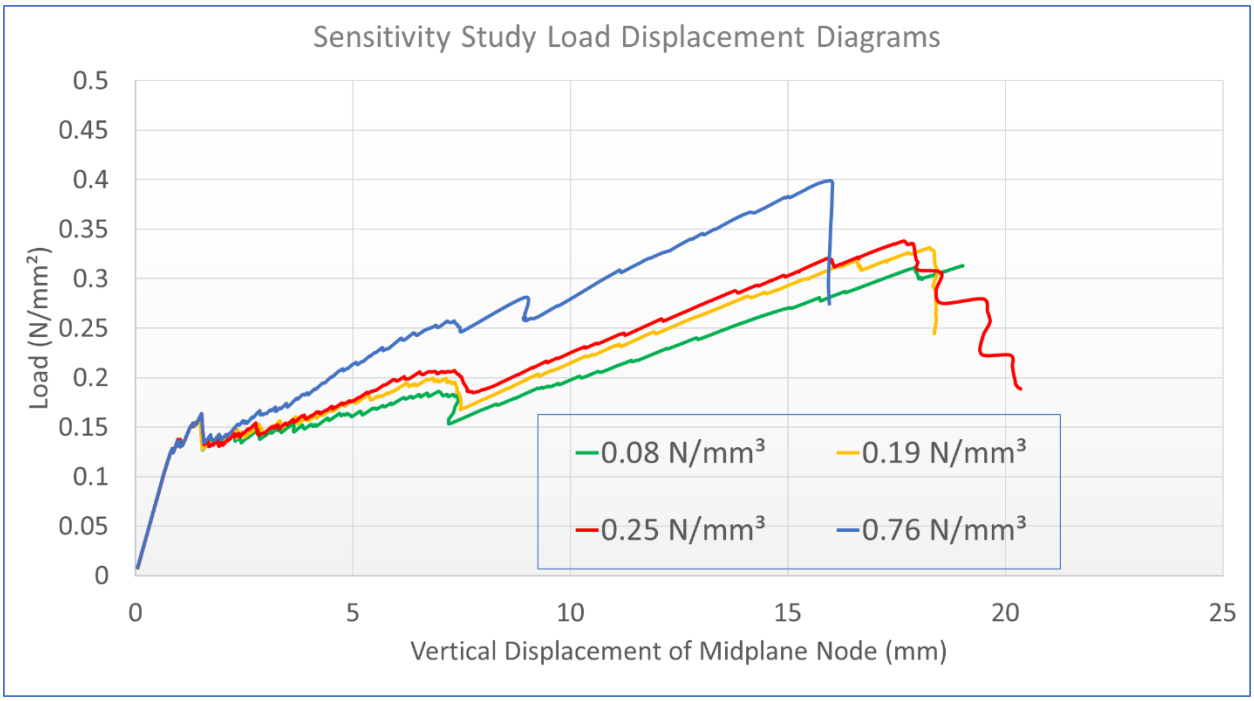

Figure 73: Load Displacement Diagrams of different spring stiffnesses without Fire Exposure

Several important conclusions can be drawn from Figure 73. Firstly, the four models exhibit similar behaviors up until the point of the first major crack formation. The material properties of the concrete and steel play a more important role than the spring stiffness at this point in the loading procedure, and so this result is expected. However, the models begin to deviate from one another after the point of the first major crack. Another important conclusion is that the load displacement diagrams increase in slope, indicating a stiffer roof slab, with each increase in spring stiffness. Lastly, the ultimate bearing capacity of each model increased with an increase in the spring stiffness.

To compare the finite stiffness values in the sensitivity analysis to Analysis 1 and Analysis 2, where infinite and no lateral stiffness are used respectively, Figure 74 is presented below.

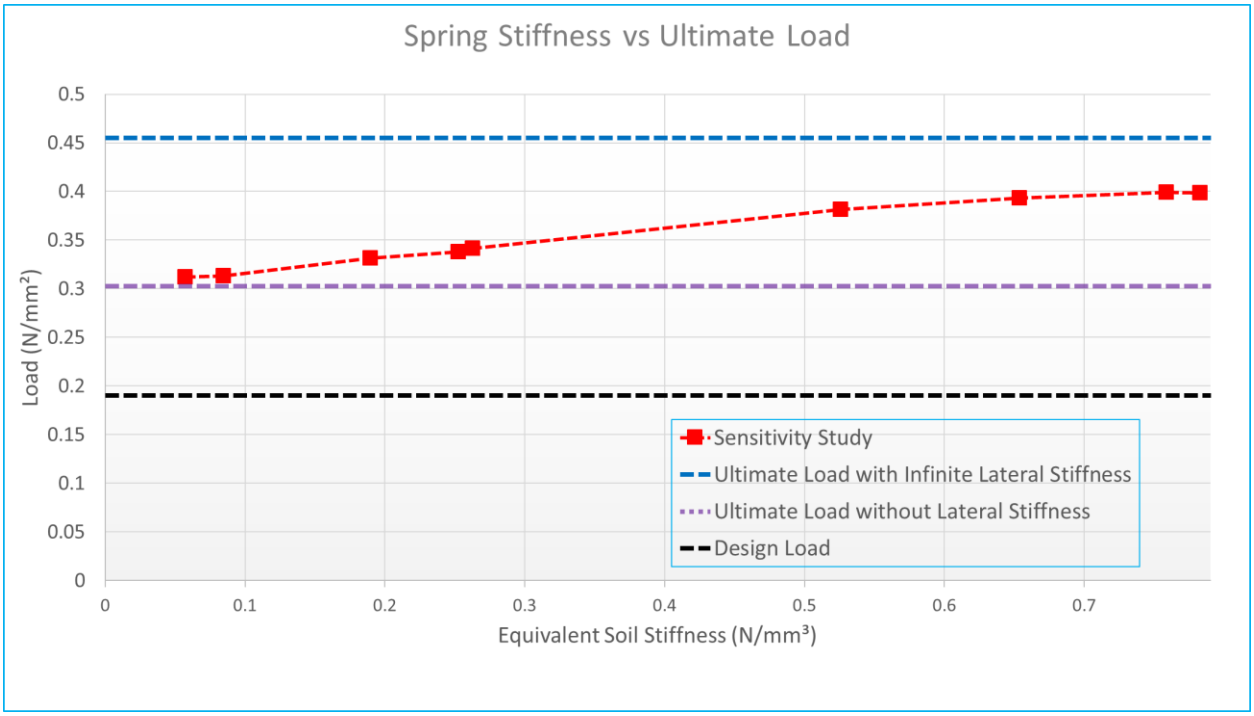

Figure 74: Ultimate bearing capacity of sensitivity analysis vs. previous analyses

Figure 74 above shows the ultimate bearing capacity of the models as a function of the spring stiffnesses defined in Section 9.3. The values are compared to the ultimate bearing capacities of Analysis 1 (infinite lateral stiffness, represented by dark blue line) and Analysis 3 (no lateral stiffness, represented by purple line). Therefore, blue and purple lines represent the theoretical maximum and minimum ultimate bearing capacities possible respectively. The ultimate bearing capacity of the structure given a non-zero finite amount of lateral stiffness must fall between the blue and the purple lines, which is what is seen in the figure. The design loaded calculated in Section 4 is shown in black. It is expected that as the spring stiffness is increased, the ultimate bearing capacities (represented by the red line) will increase within upper and lower bound shown in the figure. This result is apparent in Figure 74, thus confirming the hypothesis stated in Section 9.3.

Another result of the analyses is the increase in the compressive struts in the roof slab with increasing spring stiffness. The buildup of CMA due to the increasing linear stiffness is what allows the roof slab to achieve a higher ultimate bearing capacity. The in-plane stress components of the first four analyses in the sensitivity study can be seen in Section 12.7.

It is important to note that while increasing spring stiffness indeed increases the ultimate bearing capacity of the roof slab, once the lateral stiffness reaches a value of approximately 580 N/mm (equivalent soil stiffness 0.65 N/mm³), the marginal increase in ultimate bearing capacity begins to decline, resulting in a decrease in slope of the red line. It is expected that as the spring stiffness is increased, the ultimate bearing capacity would more closely resemble the upper boundary representative of Analysis 1. More specifically, the upper boundary represented by the purple dashed line is expected to serve as asymptote for analyses containing finite values of spring stiffness.

9.5 Lateral Stiffness Provided by Adjacent Tubes

In the case that a fire situation occurs in a middle tube, additional lateral stiffness can be provided by the adjacent tubes. In order to quantify the lateral stiffness provided by adjacent tubes, an additional study is conducted in DIANA.

9.5.1 Model

A linear finite element model is produced in order to model the stiffness provided by the adjacent tubes. The situation is shown below. The area in blue is modelled in DIANA. The forces resulting from volumetric expansion and vertical loading are represented by black arrows. The force will be taken by the adjacent tubes in compression while the The model is split into two regions, labeled “A” and “B”, as seen in Figure 76 below. The “A” region represents the region of concrete that transfers loads in tension while the “B” region represents the region of concrete transferring load in compression. Therefore, the two regions are given stiffnesses according to their expected load transfer mechanism. The model has a thickness of 875mm to represent the thickness of the roof slab. All model specifications can be found in Section 12.12.

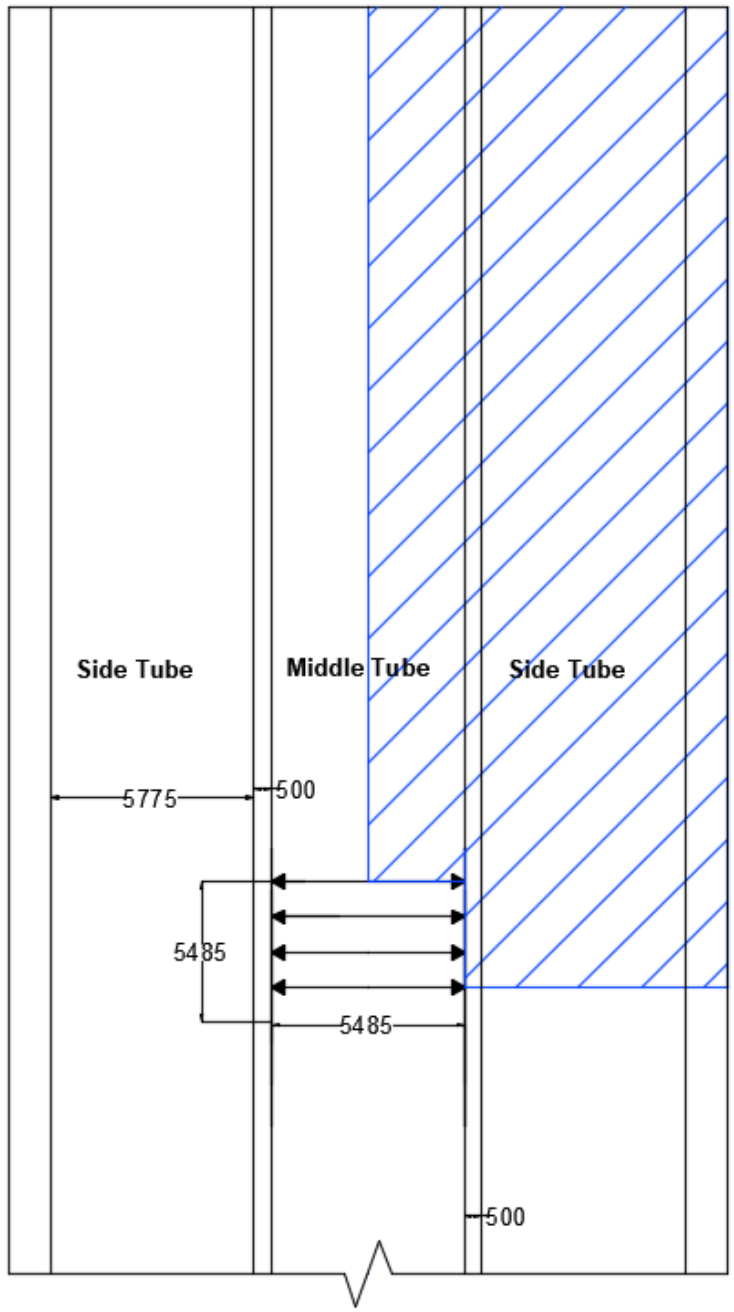

Figure 75: Mechanism of lateral stiffness provided by side tubes

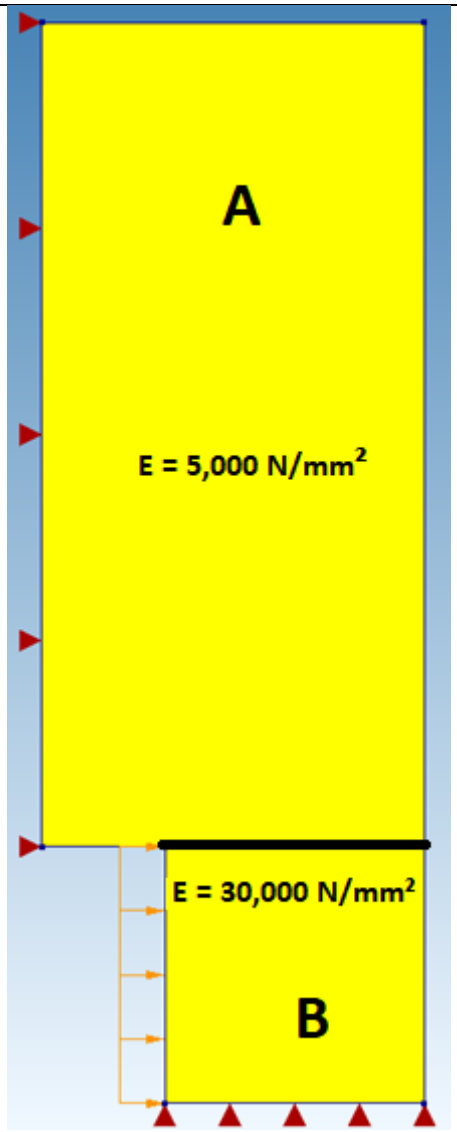

Figure 76: Finite element representation of lateral stiffness mechanism

The above figures show the immersed tube from a top view. A fire affecting the middle tube causes normal forces in all directions, as depicted by the arrows. Due to symmetry, only the right side of the roof is modeled. A line force of 1 N/mm is applied to the edge shown in Figure 76. The result is shown below.

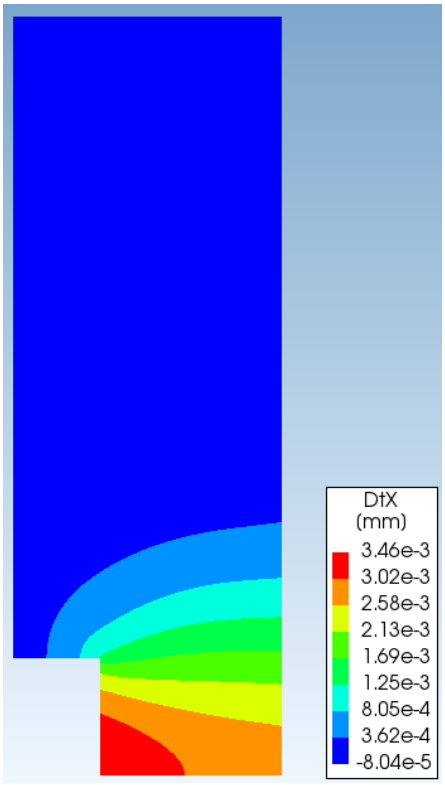

Figure 77: Lateral displacements in lateral stiffness quantification study

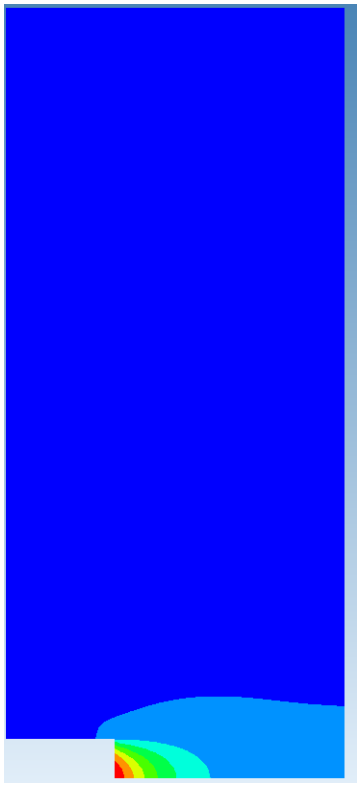

Figure 78: Reduced Fire Area

The linear stiffness is calculated by dividing the 1 N/mm force by the lateral displacement at the bottom edge. In order to gain a better understanding of the lateral stiffness provided by the adjacent tubes, the zone affected by fire is varied. Two sizes are shown in the two figures above to demonstrate the variation of the affected region. The results are shown in the table below.

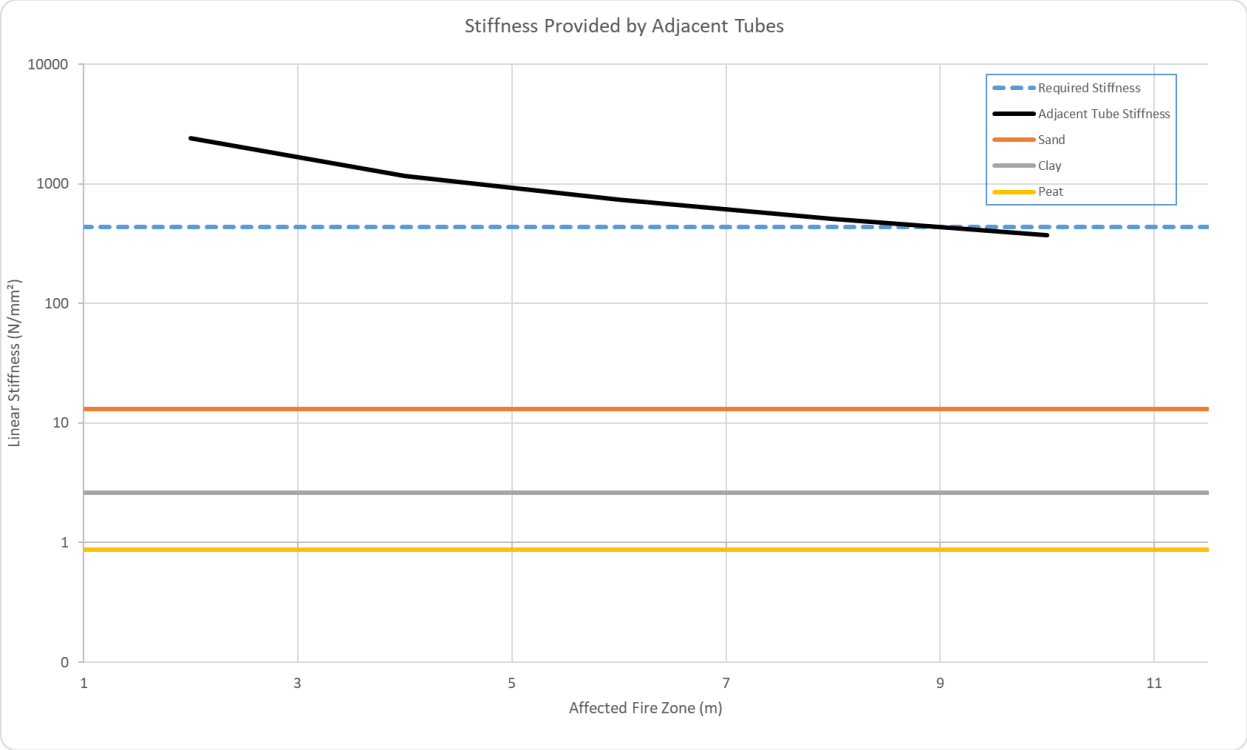

Figure 79: Lateral stiffness provided by adjacent tubes as a function of fire zone

The black line represents the results of the lateral stiffness study. The blue dashed line represents the required stiffness for CMA as concluded by the sensitivity analysis in Section 9.4. The orange, grey, and yellow lines represent the stiffnesses of common soils in the Netherlands. The soil stiffnesses are compared to those in the sensitivity study by multiplying the soil stiffness by half of the height of the roof slab (437.5 mm). The figure above shows that the lateral stiffness provided by adjacent tubes suffices for affected lengths of approximately 9 meters.

9.6 Discussion

In this section, the influence of the lateral stiffness on the formation of CMA and the ultimate bearing capacity of the roof slab is studied. Several stiffness values are chosen based on the results of Analysis 1 and Analysis 3. While it is possible to choose any non-zero finite value of spring stiffness, using the results of Analysis 1 and Analysis 3 allowed for the selection of specific

stiffnesses most likely to produce useful results. Stiffnesses that are too high or low would produce results similar to Analysis 1 and Analysis 3 respectively and would therefore not give useful information regarding the relationship between stiffness and ultimate bearing capacity.

Eight models with different linear spring stiffnesses are developed and each is loaded by an incremental vertical loading. The load displacement diagrams, in-plane stress profiles, and the cracking behavior the models is presented. The effect of linear stiffness on the buildup of CMA and the ultimate bearing capacity is subsequently established. The stiffness provided by typical Dutch soils is then compared to the values necessary to induce CMA, as per the sensitivity study.

The stiffness provided by adjacent tubes is also quantified in the sensitivity study. It was found that increasing the affected area of the fire reduces the stiffness provided by the adjacent tubes. The sensitivity study suggests that an equivalent soil stiffness of 0.50 N/mm³ is required to effectively produce CMA in the roof slab. Soils in the Netherlands have a stiffness far lower, but it is shown in the table above that the stiffness provided by the adjacent tubes may provide the necessary conditions for CMA. It is shown that the stiffness provided by adjacent tubes is inversely proportional to the size of the affected area due to fire. It is important to note that this study is conducted purely in the elastic domain with a reduced stiffness as to give a conservative estimate of lateral stiffness. Furthermore, in order to compare the soil stiffness with the stiffness provided by the concrete, the soil stiffness is multiplied by half of the roof slab height. Multiplying the stiffness by half of the height gives an approximate value of the soil contribution. Soil is a highly complex material and this approximation can be improved in future studies. Also, in this study, only the transverse forces are considered. In a real situation, forces would also be transferred in the longitudinal direction. This may have an effect on the stiffness that can be expected.

9.7 Question 3 Conclusion

A sensitivity analysis is conducted to establish the relationship between the lateral stiffness provided by soil surrounding an immersed tube and the ability for the ultimate bearing capacity of the roof slab. Load displacement diagrams and internal force vectors are developed for the eight stiffness values examined in the sensitivity study. The load displacement diagrams indicated that

increasing the spring stiffness increases the stiffness of the structure as a whole. Furthermore, load-displacement diagrams and the in-plane stresses of the models indicated an increased buildup of CMA with an increased stiffness. However, the marginal increase in ultimate bearing capacity with increased spring stiffness is shown to reduce past a spring stiffness of approximately 0.50 N/mm³, suggesting a logarithmic relationship with the linear stiffness and the ultimate bearing capacity. As the spring stiffness is increased, the ultimate bearing capacity is expected to reach that of Analysis 1, which included infinite stiffness. Therefore, it can be concluded that spring stiffness positively influences the buildup of CMA and the ultimate bearing capacity of a roof slab in an immersed tube. Furthermore, the lateral stiffness contribution from the adjacent tubes was evaluated. It was determined that the lateral stiffness is a function of the size of the affected region due to fire and that sufficient lateral stiffness may not be achieved if the fire grows to a length of approximately 10 meters.

10 Discussion

10.1 The Compression Curve

The finite element model used for this thesis project is based upon a typical immersed tube in the Netherlands. The goal of a finite element model is to predict, as accurately as possible, structural response to loading. Developing a reliable finite element model which is also efficient in terms of computing time requires many simplifications of the real-word structure. These simplifications, while reducing computing time, cause the model to deviate from the real-world situation. Therefore, simplifications and modeling choices must be made with great caution and understanding of the implications.

One of the major modeling decisions made in the course of this project is the choice of compression curve for the concrete material. Concrete's compressive curve, cracking and crushing behaviors, and the dependence of concrete's mechanical and thermal properties on temperature are complex topics which must be addressed with caution in the finite element model. Since a compression model which is both mesh independent and dependent on temperature is not available in finite element packages, a decision as to which feature of the compression curve is more important for this project had to be taken. Due to the presence of fire in this thesis project, it is decided to use a compression curve dependent on temperature, specifically the NEN 1992-1-2 curve. Since the NEN 1992-1-2 curve is mesh dependent, specifically on the crack-band width in the finite element model, great care is taken to ensure that the curve is properly fitted to the crack-band width in the finite element model. The procedure for ensure a proper NEN 1992-1-2 is described in Section 5.4. The procedure involved first establishing the Parabolic curve based on experimental uniaxial compression testing data at 20°C and subsequently fitting the NEN 1992-1-2 to the developed Parabolic curve. In that way, a curve whose stress-strain relation in compression is temperature dependent and based on experimental data is established. The NEN 1992-1-2 is fitted to the Parabolic curve by adjusting the ε_u parameter. While this is necessary for the development of an experimentally driven compression curve, ε_u at room temperature is a value defined in the EC, given in Table 5.

Changing ε_u meant losing the connection to the EC defined compression curve for 20°C. It was considered to scale the values of ε_{c1} and ε_u, but the value of ε_{c1} increases so rapidly between temperatures of 200-600°C as to overtake the value of ε_{cu}, resulting in a non-sensical post-peak behavior. Therefore, it is decided to linearly interpolate ε_{c1} and ε_u to their values at 1200°C to reestablish the temperature dependence in accordance with EC values. While linear interpolation serves as a simple approximation, the effect of temperature on material properties is often a highly nonlinearly phenomenon. Non-linear methods of interpolation are surely possible and is suggested a topic for further research.

Furthermore, it is important to acknowledge the impact of adjusting the ε_u. To quantify the impact, two models are developed. One model contained the EC value of ε_u at 20°C of 0.02, while the other model contained the adjusted value of 0.0085. The load-displacement diagrams resulting from vertically loading each model are shown below.

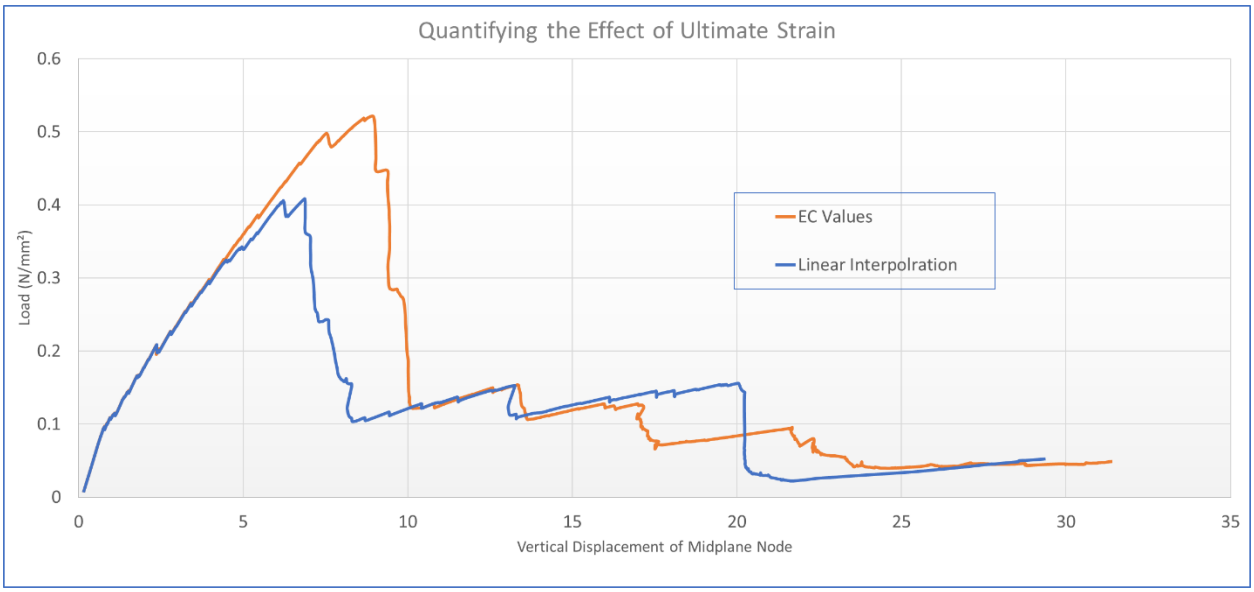

Figure 80: Load displacement diagrams of adjusted and EC NEN 1992-1-2 curve

While the shape of the load-displacement diagram and therefore the structural behavior does not significantly change, there is a significant increase in ultimate bearing capacity when using the EC values. Therefore, it is recommended to use the curve only when absolutely necessary. The NEN 1992-1-2 can be used to check the impact that the expected fire will have on the material. If it is

determined that the fire does not significantly affect the performance of the concrete, it is recommended to revert to a mesh independent compression curve such as the Parabolic curve.

10.2 Lateral Stiffness

Table 4 defines the lateral stiffnesses which are investigated in this sensitivity study. The values ranged from 0.08-0.78 $\frac{N}{mm^3}$. In the Netherlands, sand is the predominant material found below riverbeds. According to standard design practices, the first branch of stiffness of medium-packed sand is between 0.02 and 0.045 $\frac{N}{mm^3}$ (28). The results shown in Section 9.4 suggest that the stiffness provided by Dutch sand alone is not sufficient to produce CMA in roof slabs of immersed tubes. However, it may be the case that other sources of lateral stiffness can be utilized to induce CMA in middle tubes of immersed tunnels, such as stiffness provided by adjacent tubes. A simple finite element study was conducted to estimate the lateral stiffness to be expected from adjacent tubes. The values varied based on the effected fire region. The study showed that the necessary lateral stiffness may be present. The influence of lateral stiffness sources other than soil on the formation of CMA is suggested as a topic for future research.

It is important to note that while the stiffnesses used in this sensitivity study are assumed constant over the height of the roof slab, soil stiffness increases with depth. It is possible that the increased stiffness with depth influences the results of the sensitivity study. To simplify the finite element model and because the potential for the increased stiffness with depth is assumed not to be of great importance, it is not included in the finite element model. Soil is an incredibly complex and nonlinear material and a simplified model is preferable to avoid unnecessary complications.

10.3 Spalling Velocity

The effect of spalling on the ability of the roof slab to develop CMA is established in Section 8. To establish the influence of spalling on the buildup of CMA, the spalling velocity for the PSFC had to be estimated. The spalling velocity estimation is based on experiments conducted by Austrian Ministry for Transport, Innovation, and Technology using the RWS fire curve. The Austrian Ministry conducted an RWS fire test on a concrete slab and measured the resulting

spalling velocity. Temperature penetration charts are created by applying the same fire curve to the finite element model. The velocity of the penetration of 150°C as a result of the RWS curve is shown to line up closely with the spalling velocity reported in the fire test. Therefore, the prediction of the spalling velocity in the PSFC is based on the velocity of 150°C as well. Since concrete is known to spall at approximately 200°C, this approximation fit well with previous literature. The implication of using the estimated spalling speed is that spalling had not reached the bottom layer of reinforcement after a period of 2000 seconds. Had spalling reached the bottom layer of reinforcement, direct heating of the reinforcement by the PSFC would have quickly caused thermal degradation of the reinforcement. Reinforcement degradation could have serious implications for the buildup of CMA and the ultimate bearing capacity of the roof slab.

Another implication of using the estimated spalling velocity is that the concrete strength of the newly exposed layer of concrete due to spalling is not reduced. Since the spalling velocity is assumed to follow the 150°C penetration speed, the newly exposed layer of concrete will have a temperature of 150°C, at which 97% of the compressive strength remains. However, a fire test is necessary to confirm this result. If a fire test in an immersed tube concludes that spalling occurs at a temperature significantly higher than 150°C, the finite element model should consider the strength reduction due to the temperature increase. This may have implications for the effect that spalling has on the formation of CMA and the ultimate bearing capacity in the roof slab. To establish a more accurate spalling velocity, further investigation into the PSFC and the spalling velocity induced are recommended as future research questions.

It is important to note that while this method of determining the spalling velocity is based on previous experimental work, it is a possibility that the 150°C penetration speed selected from the RWS experiments is not directly transferrable to other fire curves.

10.4 The PSFC

The PSFC is a fire curve developed by Arcadis to study the phenomenon of railcar ignition in an immersed tube. The CFD analysis produced temperatures in 3D space as a function of time as a result of the ignition. The ITFC is applied in specific increments, each followed by the vertical

loading. This is to quantify the ultimate load bearing capacity of the structure as a function of time. The analysis is conducted for a period of 2000 seconds due to the analysis being focused mainly on the safety of tunnel occupants rather than structural safety. It is possible that the continuation of the ITFC would eventually cause further damage to the structure than reported in this thesis project, especially when considering that the concrete temperature can be seen to still be rising in Figure 46. There are two major causes for concern regarding an ITFC with greater duration. The first cause for concern involves the more severe thermal degradation of concrete over time. This would naturally result in a significant loss of compressive strength and an increase in ductility.

The second cause for concern involves spalling. The estimation of spalling velocity in this thesis concludes that spalling does not reach the bottom reinforcement, embedded 50mm in the concrete, after 2000 seconds of ITFC exposure. A longer duration ITFC will likely increase the spalling depth, potentially exposing the bottom layer of reinforcement. Reinforcement exposure would result in direct heating by the ITFC and cause substantial thermal degradation of the steel. Steel degradation has significant implications for the bearing capacity of the roof slab. It is therefore a suggestion for future research to develop an ITFC of longer duration.

11 Conclusions

CMA in immersed tubes are investigated in this thesis project through the use of the finite element method. Specifically, three questions are addressed. The questions and their conclusions are described below:

Question 1: How does the thermal degradation of concrete's mechanical properties as a result of fire affect the formation of CMA in an immersed tube roof slab subjected to fire?

To address this question, a model of the roof slab with temperature dependent concrete strength is subjected to a fire curve specific to immersed tubes, referred to as the ITFC in this report. Following the fire exposure, an incremental vertical load is applied. The ultimate bearing capacity of the roof slab as a function of ITFC exposure duration is compared with that of a model with temperature independent concrete strength. The ultimate bearing capacity of both models match each other in terms of the ultimate load values and remain approximately constant throughout the ITFC exposure, suggesting that the thermal degradation resulting from the ITFC does not prevent the buildup of CMA.

To understand the insignificance of the ITFC thermal degradation, nodes particularly important for the development of CMA are examined. The strength reduction of the nodes is found not to be significant enough to inhibit the development of CMA. This confirms the result that the thermal degradation resulting from 2000 seconds of ITFC exposure does not affect the ability of CMA to form within the roof slab nor does it significantly influence its ultimate bearing capacity.

Question 2: How does spalling influence the formation of CMA and the ultimate bearing capacity of an immersed tube?

The effect of spalling on the formation of CMA and the ultimate bearing capacity of the roof slab is established by first approximating a spalling velocity based on previous experimental data and removing the expected spalled concrete from the finite element model. Unspalled and spalled models are loaded and the results are compared. Two important conclusions are found through this procedure. The first conclusion is that spalling does not reach the bottom reinforcement of the roof slab over the course of the ITFC. The second conclusion is that while spalling does not

significantly restrict the formation of CMA, the ultimate bearing capacity of the roof slab decreased by approximately 7% over the course of the ITFC.

Can the lateral stiffness provided by Dutch soils alone provide the necessary lateral stiffness to induce CMA?

The effect of lateral stiffness on the formation of CMA is investigated via a sensitivity study in which several non-zero finite values of lateral stiffness are applied to the finite element model before loading. Results showed an increase in the development of CMA and the ultimate load bearing capacity of the structure with increased stiffness. Therefore, it is concluded that increasing lateral stiffness has a positive effect on the formation of CMA and the ultimate bearing capacity in the roof slab.

12 Annexes

12.1 Annex A: Determination of Compression Curve of Concrete

Parabolic Compression Curve

Material Properties are defined

$$f_c := 27 : G_c := 13 : h := 130 : E := 31000 : \alpha_{\frac{c}{3}} := -\frac{1}{3}\cdot\frac{f_c}{E} : \alpha_c := -\frac{5}{3}\cdot\frac{f_c}{E} : \text{alpha}_u := \min\left(\alpha_c - \frac{3}{2}\cdot\frac{G_c}{h\cdot f_c}, 2.5\cdot\alpha_c\right) :$$

The first branch of the parabolic compression curve is defined

$$f_1 := -\frac{f_c}{3}\cdot\frac{\text{alpha}}{\alpha_{\frac{c}{3}}} :$$

The second branch of the parabolic compression curve is defined

$$f_2 := -\frac{f_c}{3}\cdot\left(1 + 4\frac{\left(\text{alpha} - \alpha_{\frac{c}{3}}\right)}{\left(\alpha_c - \alpha_{\frac{c}{3}}\right)} - 2\left(\frac{\left(\text{alpha} - \alpha_{\frac{c}{3}}\right)}{\left(\alpha_c - \alpha_{\frac{c}{3}}\right)}\right)^2\right) :$$

The third branch of the parabolic compression curve is defined

$$f_3 := -f_c\cdot\left(1 - \left(\frac{\text{alpha} - \alpha_c}{\alpha_u - \alpha_c}\right)^2\right) :$$

The fourth branch of the parabolic compression curve is defined

$$f_4 := 0 :$$

$$plot\left(f_1, \text{alpha} = 0 \,..\alpha_{\frac{c}{3}}\right)$$

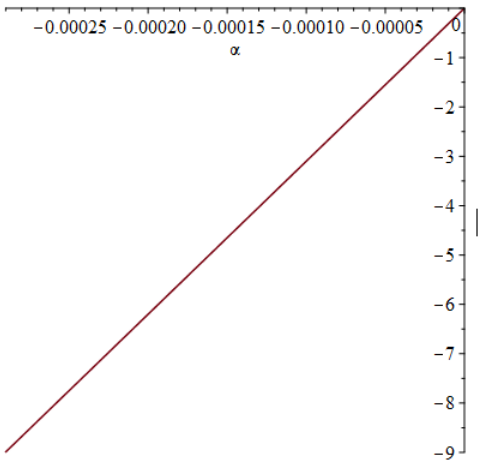

$plot\left(f_2, \text{alpha} = \alpha_{\frac{c}{3}} .. \alpha_c\right)$

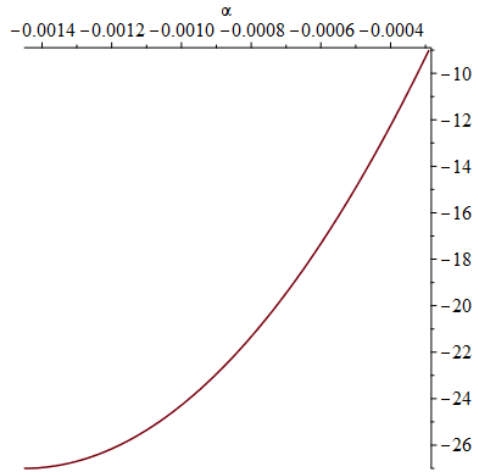

$plot\left(f_3, \text{alpha} = \alpha_c .. \alpha_u\right)$

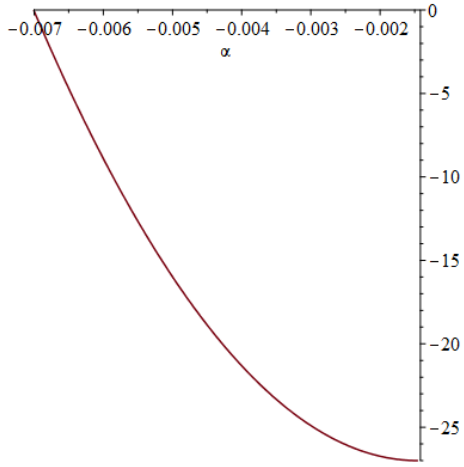

The area under the full parabolic compression curve is evaluated

$$\int_0^{\alpha_{\frac{c}{3}}} f_1 \,\text{dalpha} + \int_{\alpha_{\frac{c}{3}}}^{\alpha_c} f_2 \,\text{dalpha} + \int_{\alpha_c}^{\alpha_u} f_3 \,\text{dalpha}$$

$$\frac{7793}{62000}$$

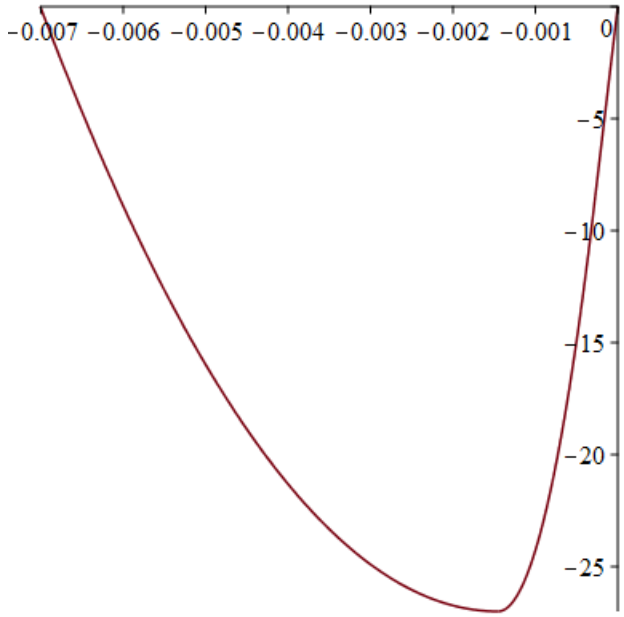

NEN 1992-1-2 Curve

$$equation_{1-2} := \frac{3\cdot\left(\epsilon_c\cdot 27\right)}{0.003\left(2+\left(\frac{\epsilon_c}{0.003}\right)^3\right)}:$$

The equation to solve for the ultimate strain of NEN 1992-1-2 is set up

$$\int_0^{\alpha_{\frac{c}{3}}} f_1\,\mathrm{dalpha} + \int_{\alpha_{\frac{c}{3}}}^{\alpha_c} f_2\,\mathrm{dalpha} + \int_{\alpha_c}^{\alpha_u} f_3\,\mathrm{dalpha} = \int_0^{0.003} equation_{1-2}\,\mathrm{d}\epsilon_c + \frac{1}{2}\cdot 27\cdot x:$$

$$\epsilon_{u_{1-2}} := 0.003 + x$$

$$\epsilon_{u_{1,2}} := 0.008503112646$$

12.2 Annex B: Analyses 1-4 Load Displacement Diagrams

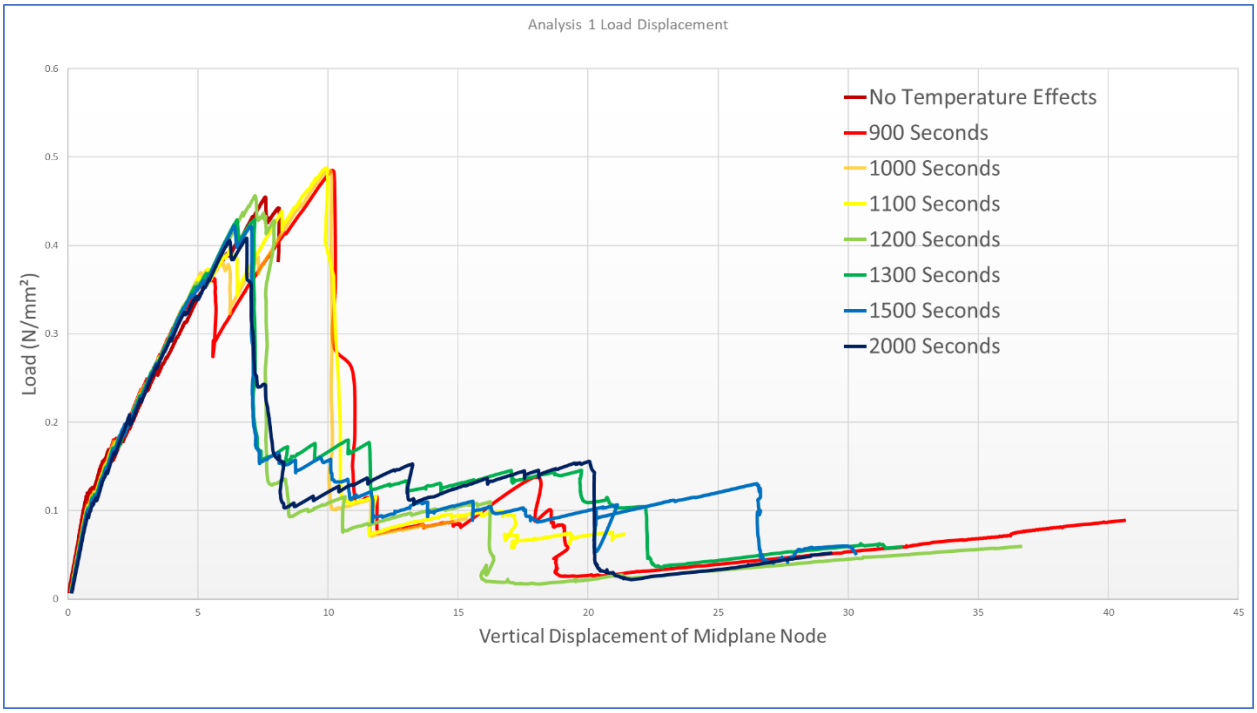

Figure 81: Load displacement diagrams for Analysis 1 for different durations of fire exposure

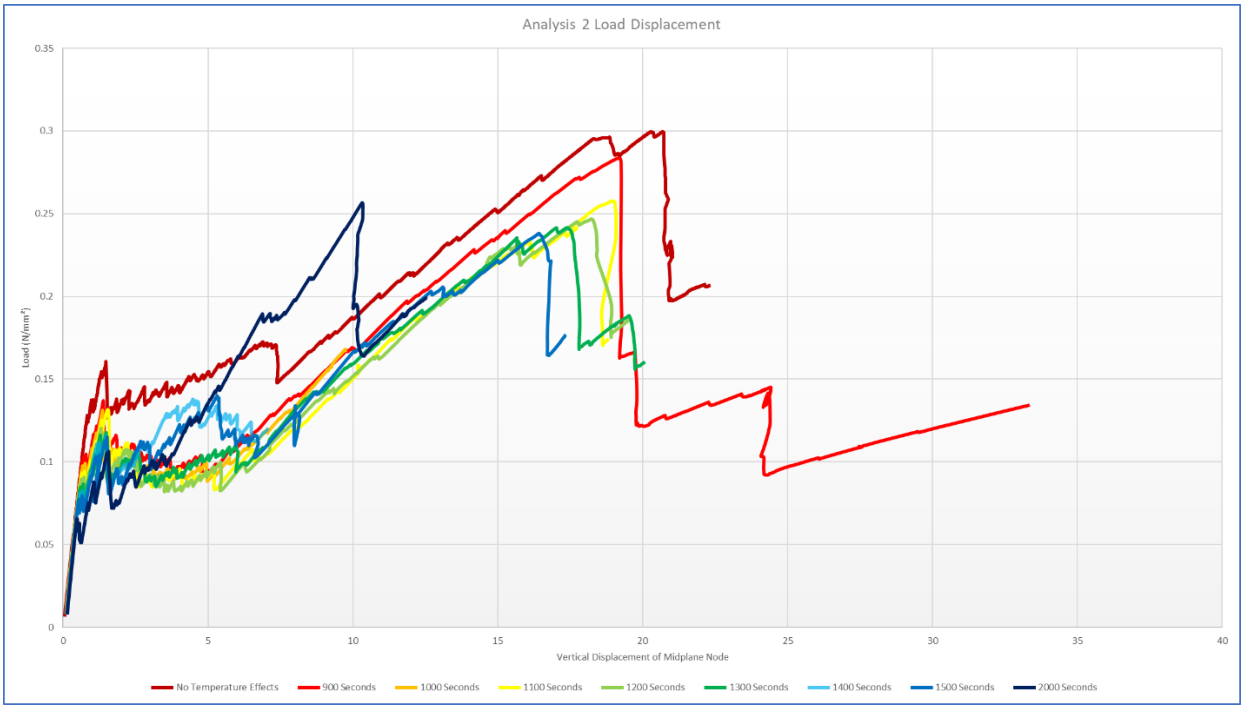

Figure 82: Load displacement diagrams for Analysis 2 for different durations of fire exposure

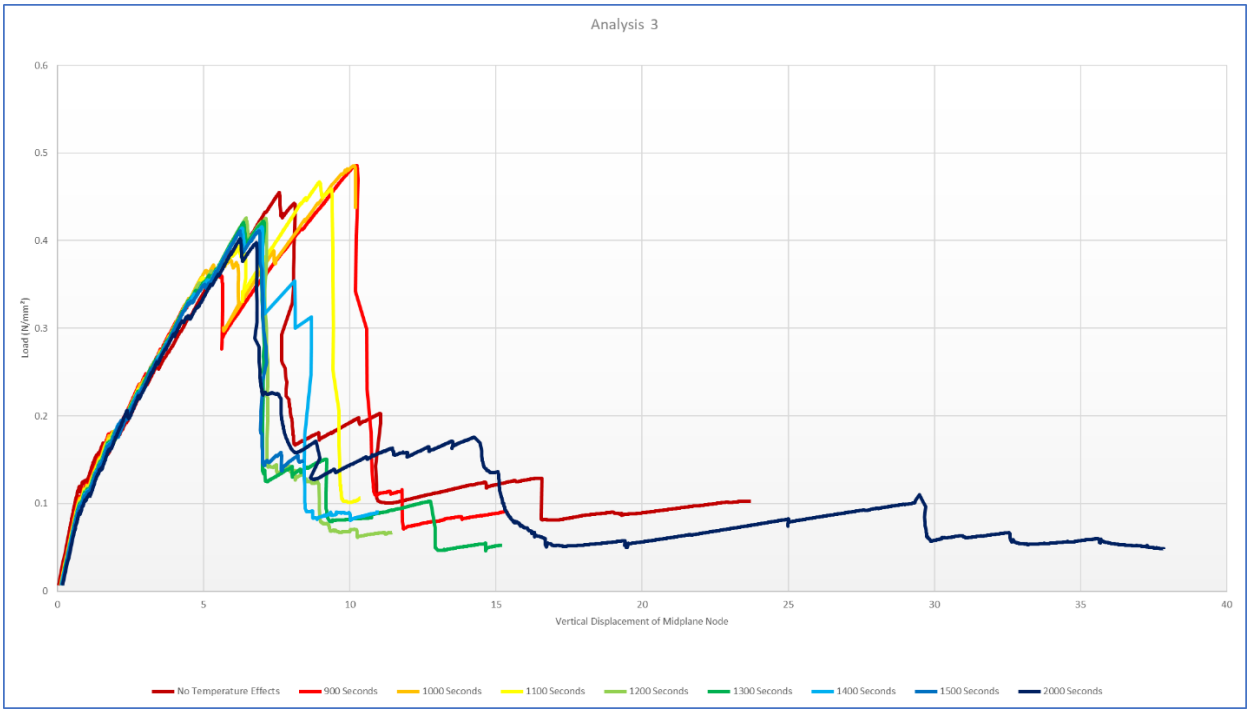

Figure 83: Load displacement diagrams for Analysis 3 for different durations of fire exposure

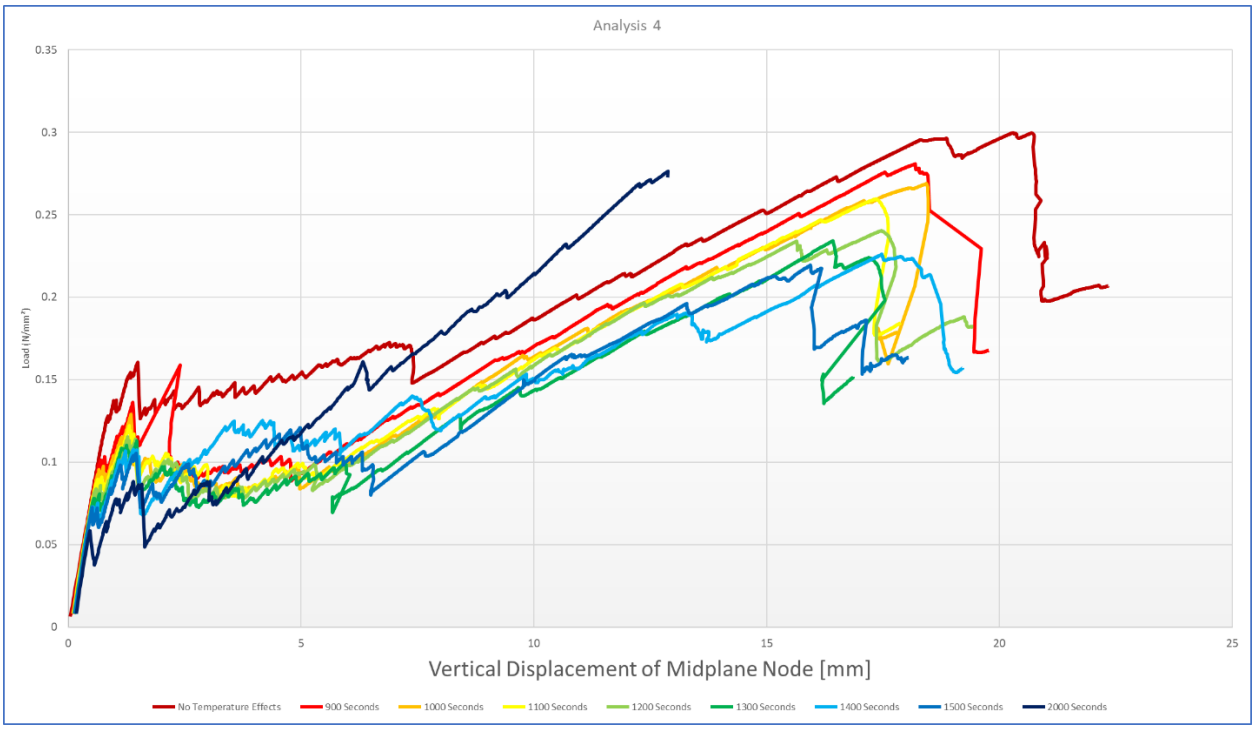

Figure 84: Load displacement diagrams for Analysis 4 for different durations of fire exposure

12.3 Annex C: Fire Exposure Duration vs. Ultimate Bearing Capacity Graphs

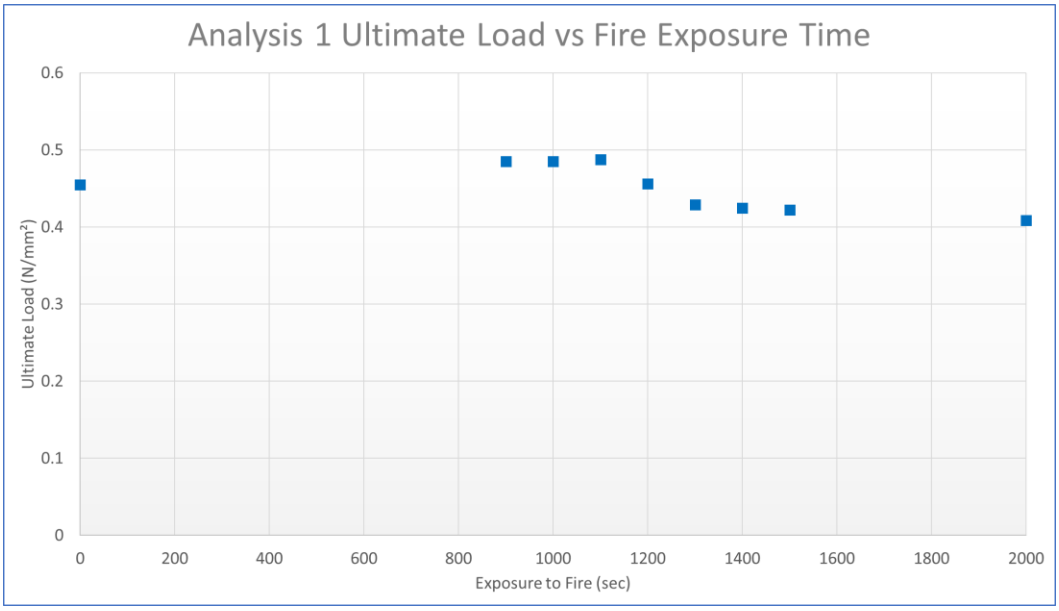

Figure 85: Fire exposure time vs ultimate load Analysis 1

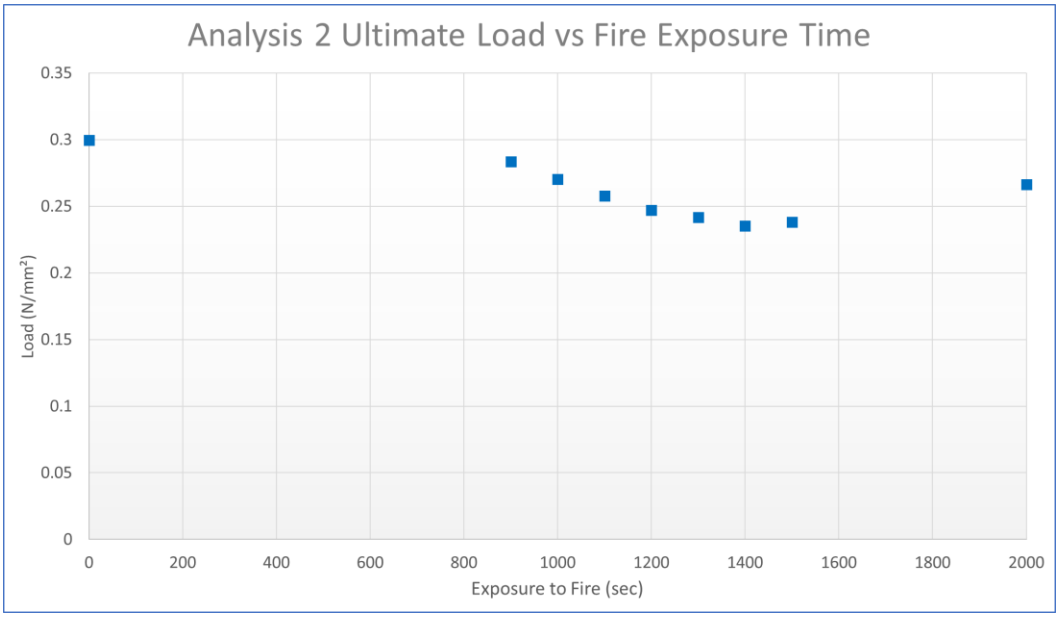

Figure 86: Fire exposure time vs ultimate load Analysis 2

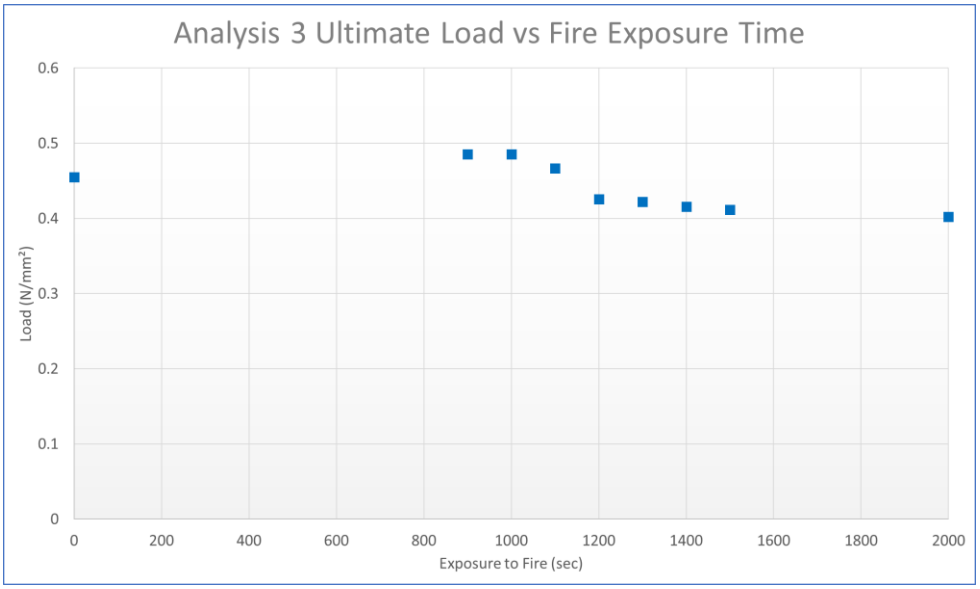

Figure 87: Fire exposure time vs ultimate load Analysis 3

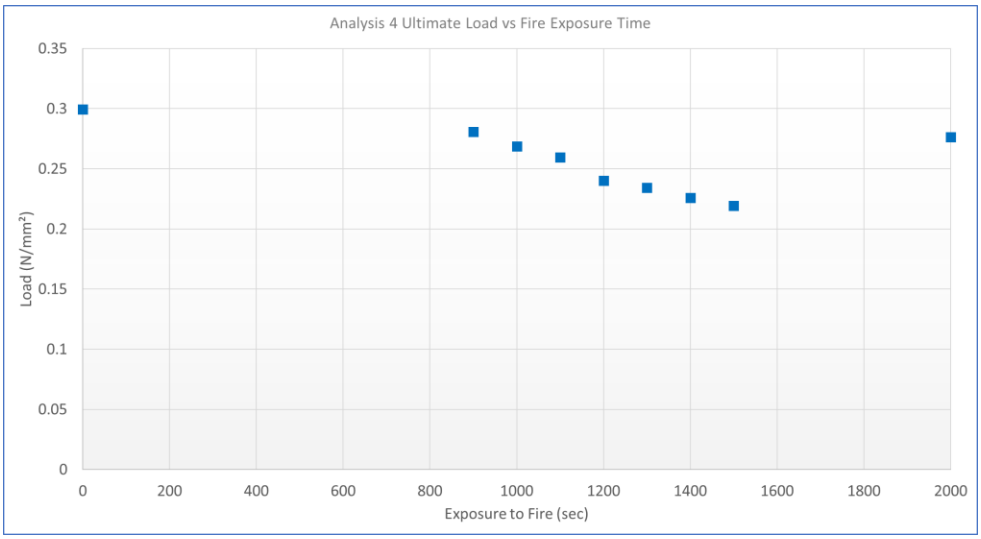

Figure 88: Fire exposure time vs ultimate load Analysis 4

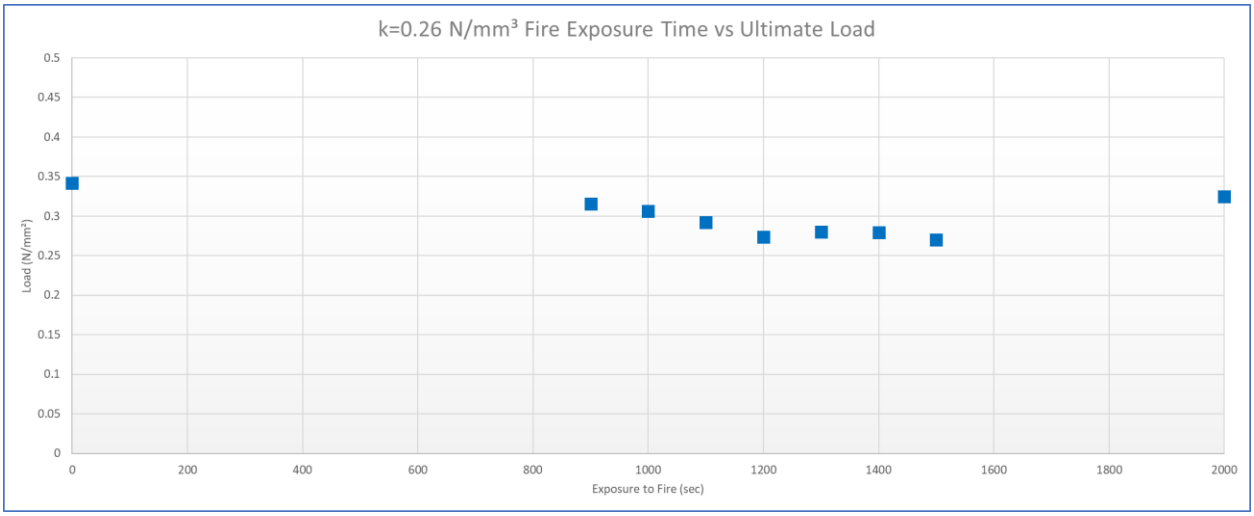

Figure 89: Fire exposure time vs ultimate load 0.26 N/mm³

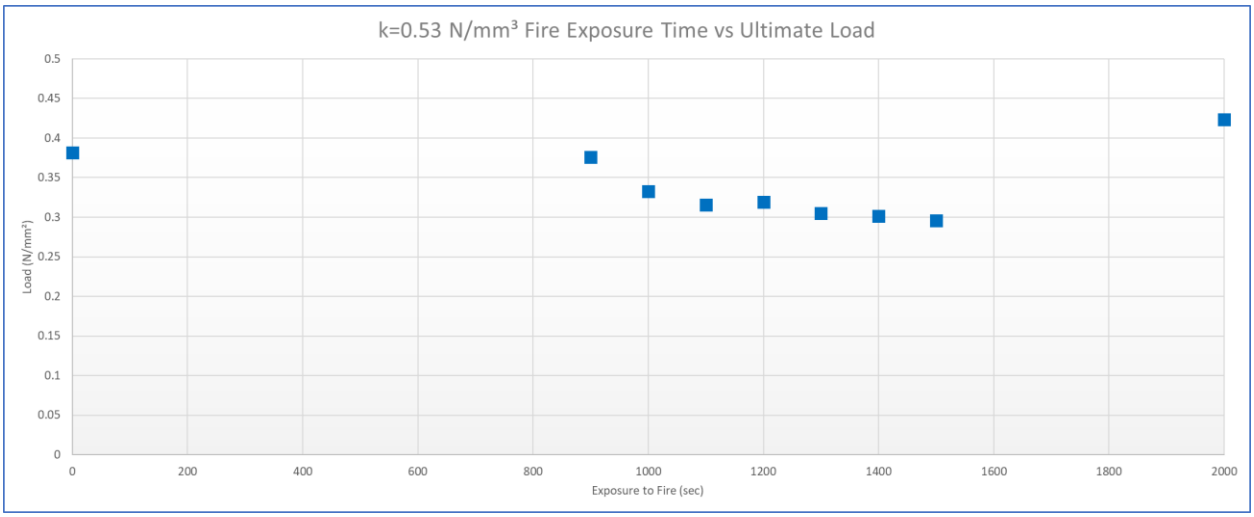

Figure 90:Fire exposure time vs ultimate load 0.53 N/mm³

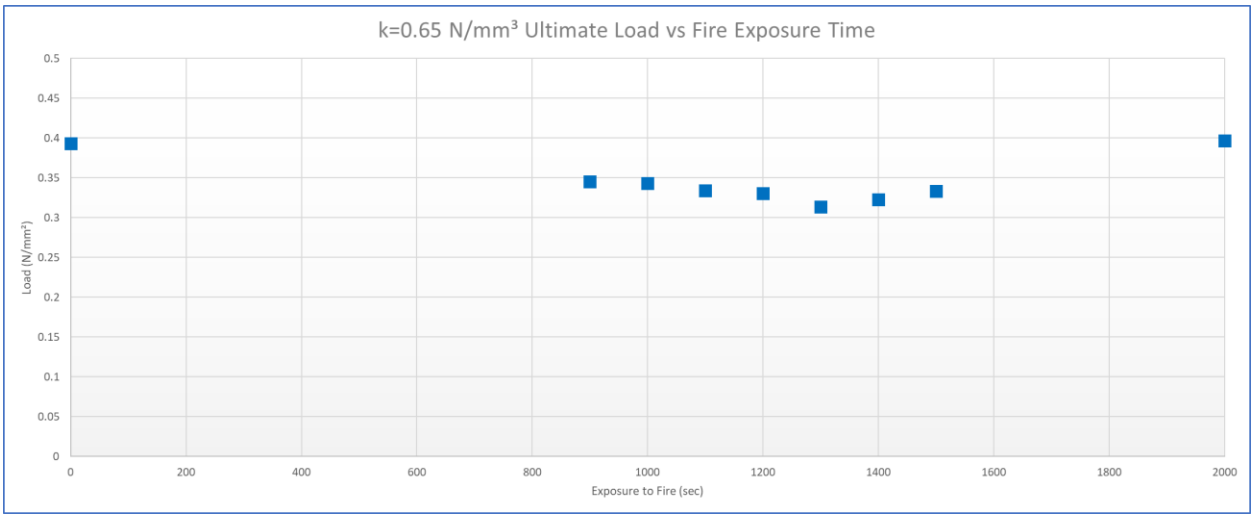

Figure 91: Fire exposure time vs ultimate load 0.65 N/mm³

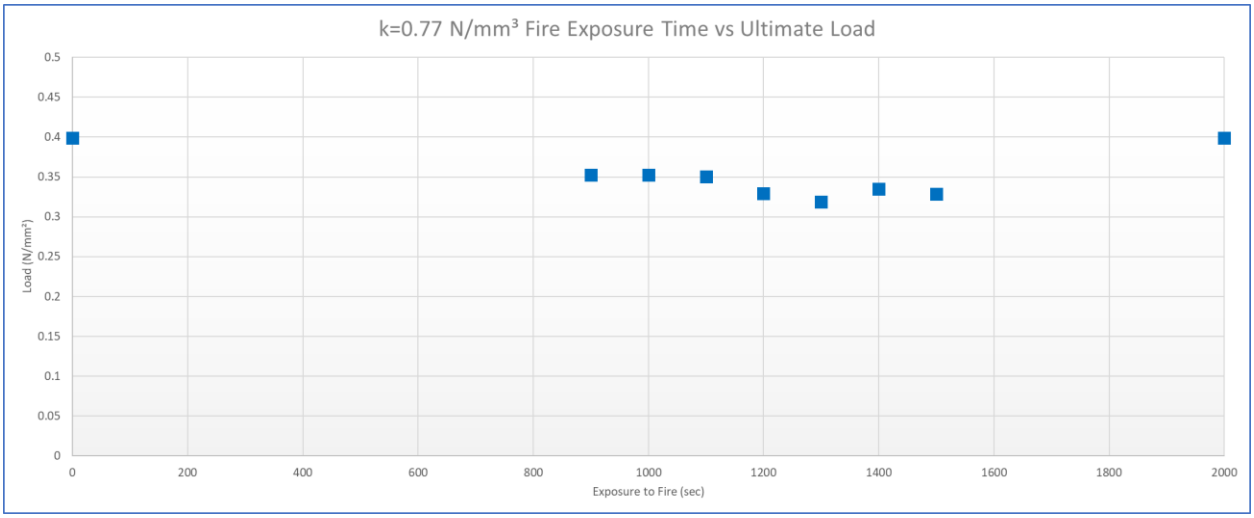

Figure 92:Fire exposure time vs ultimate load 0.77 N/mm³

12.4 Annex D: Normal Force Buildup

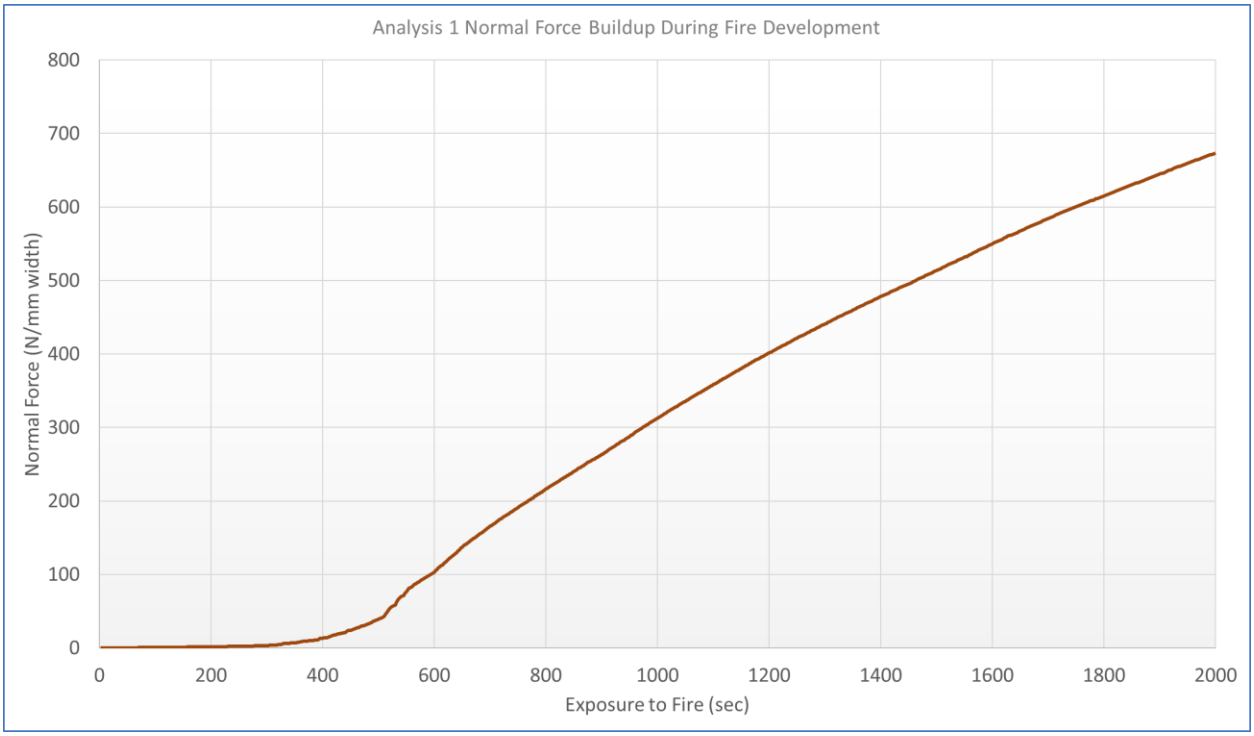

Figure 93: Normal force buildup during fire exposure Analysis 1

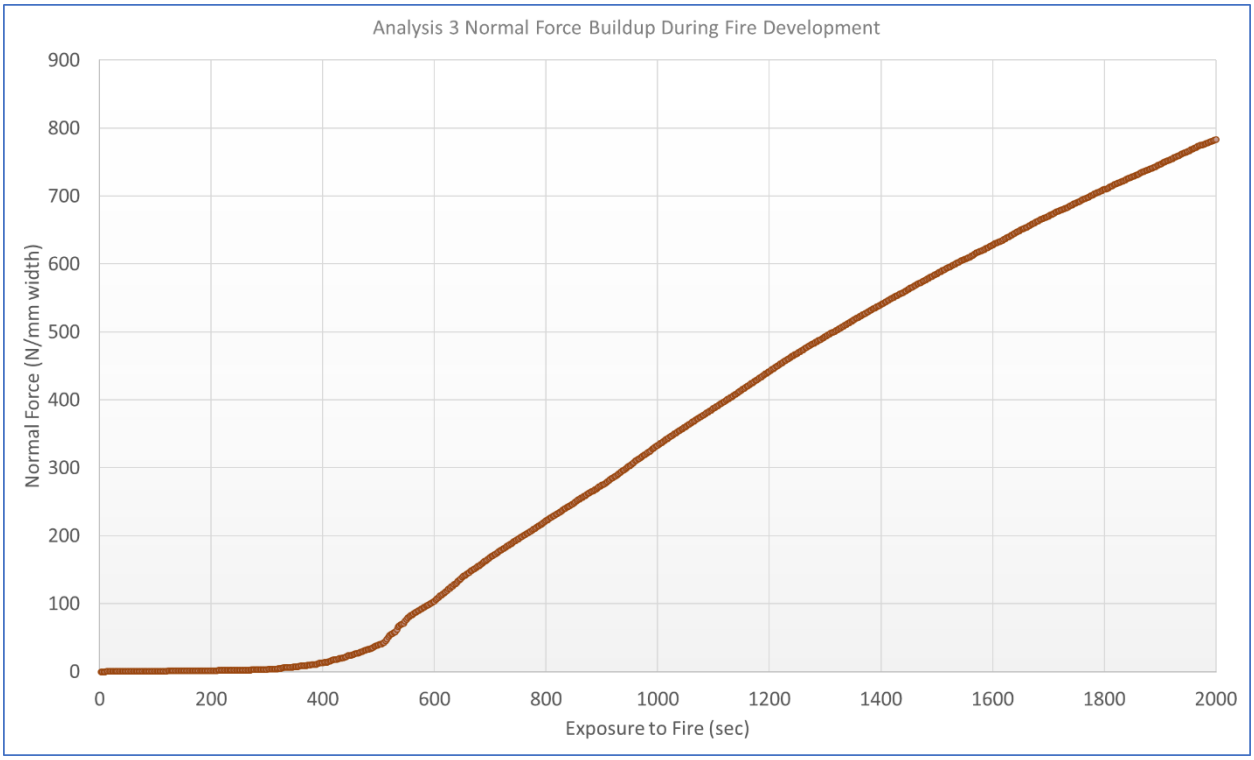

Figure 94: Normal force buildup during fire exposure Analysis 3

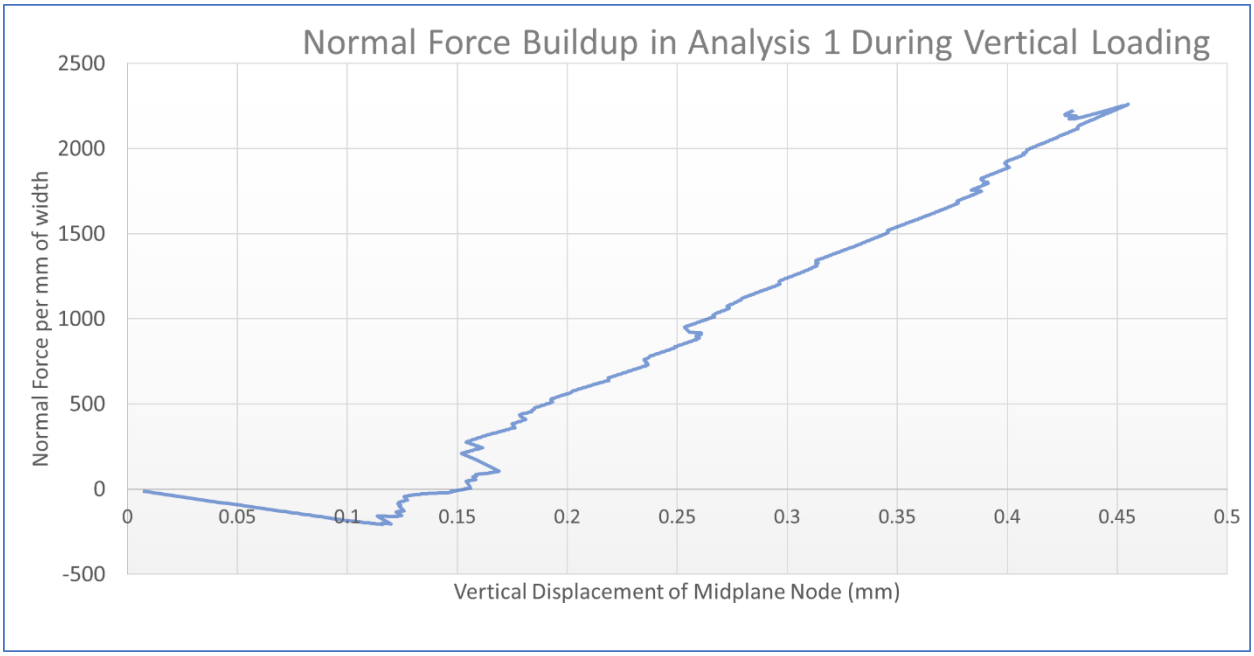

Figure 95: Normal Force Buildup in the 1mm thick model

12.5 Annex E: Normal Force During Loading vs. Ultimate Load Capacity

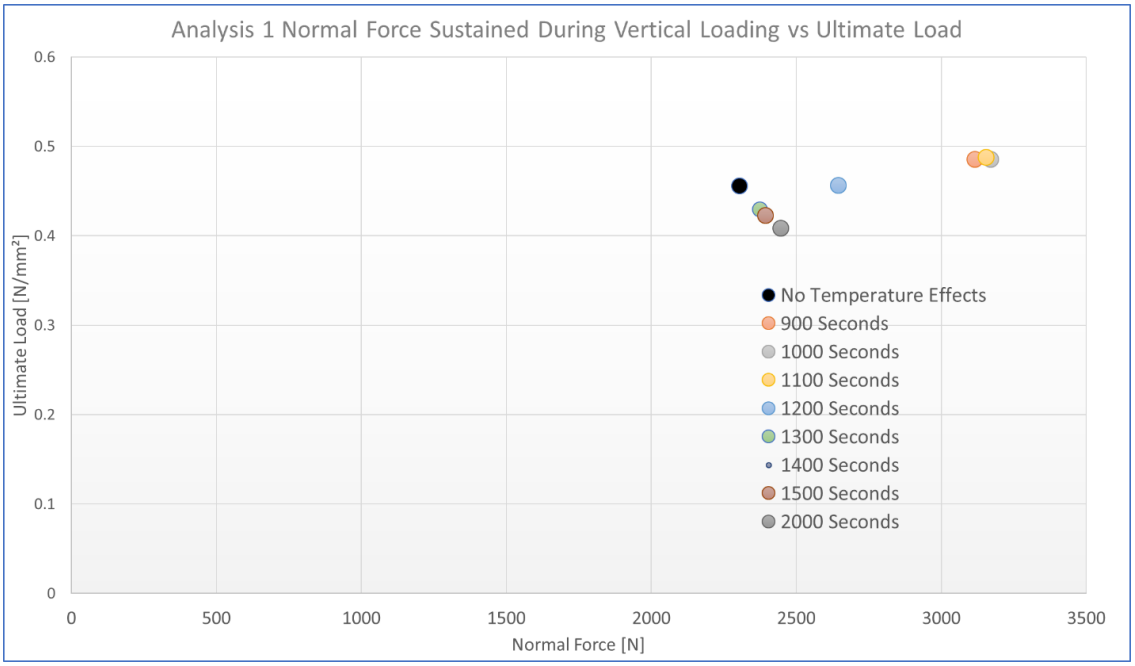

Figure 96: Normal force sustained during vertical loading vs. ultimate load Analysis 1

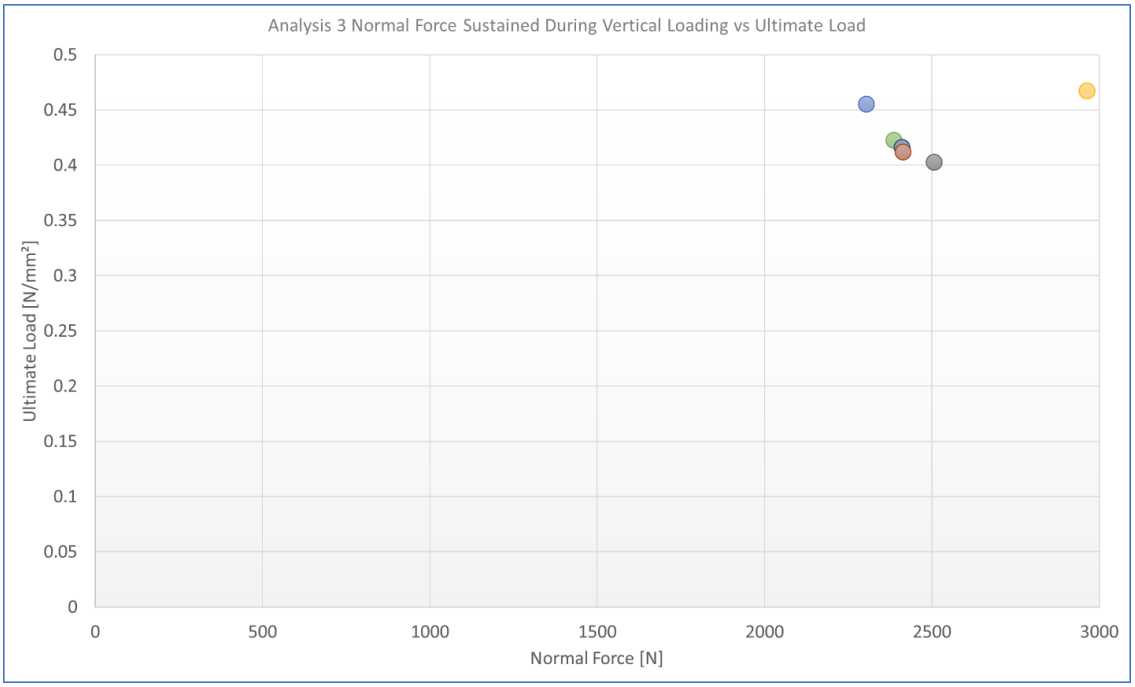

Figure 97: Normal force sustained during vertical loading vs. ultimate load Analysis 3

12.6 Annex F: Sensitivity Study Load Displacement Diagrams

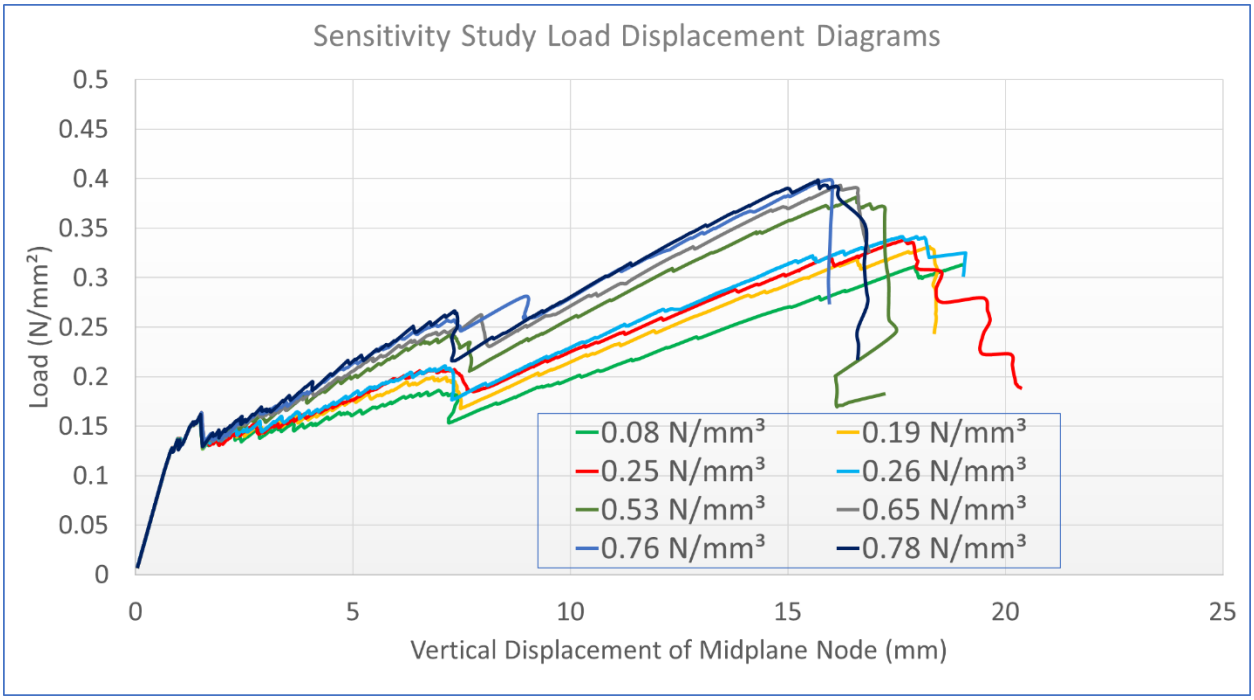

Figure 98: Load Displacement Diagrams of all eight models in sensitivity study

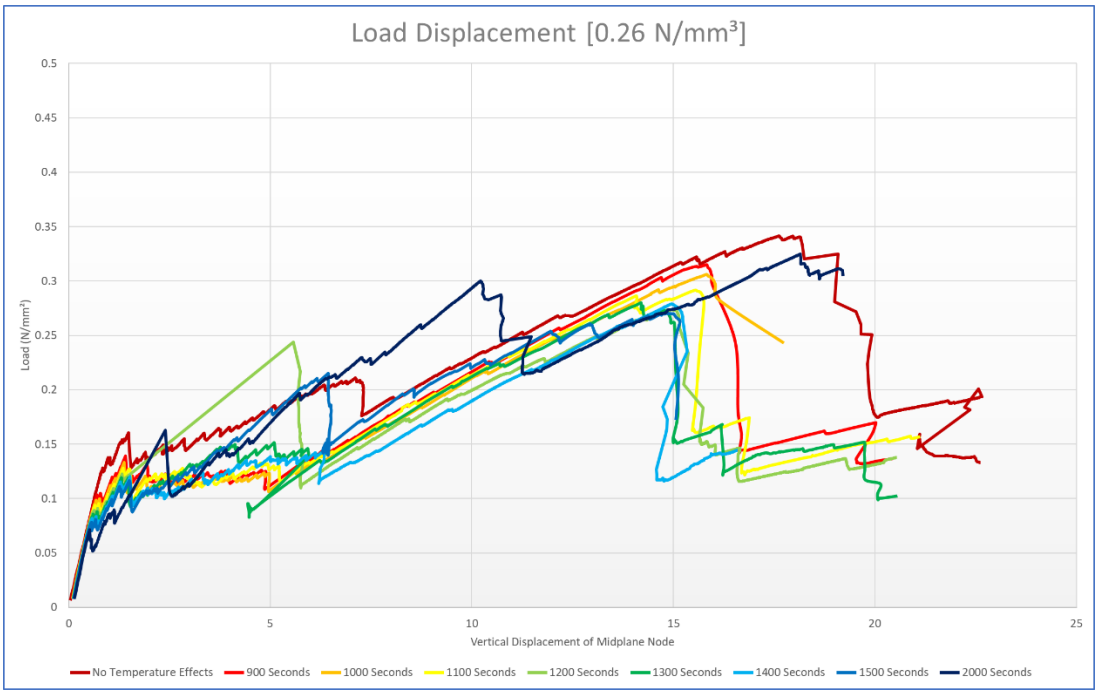

Figure 99: k=0.26 N/mm³ spring stiffness load displacement diagrams for different durations of fire exposure

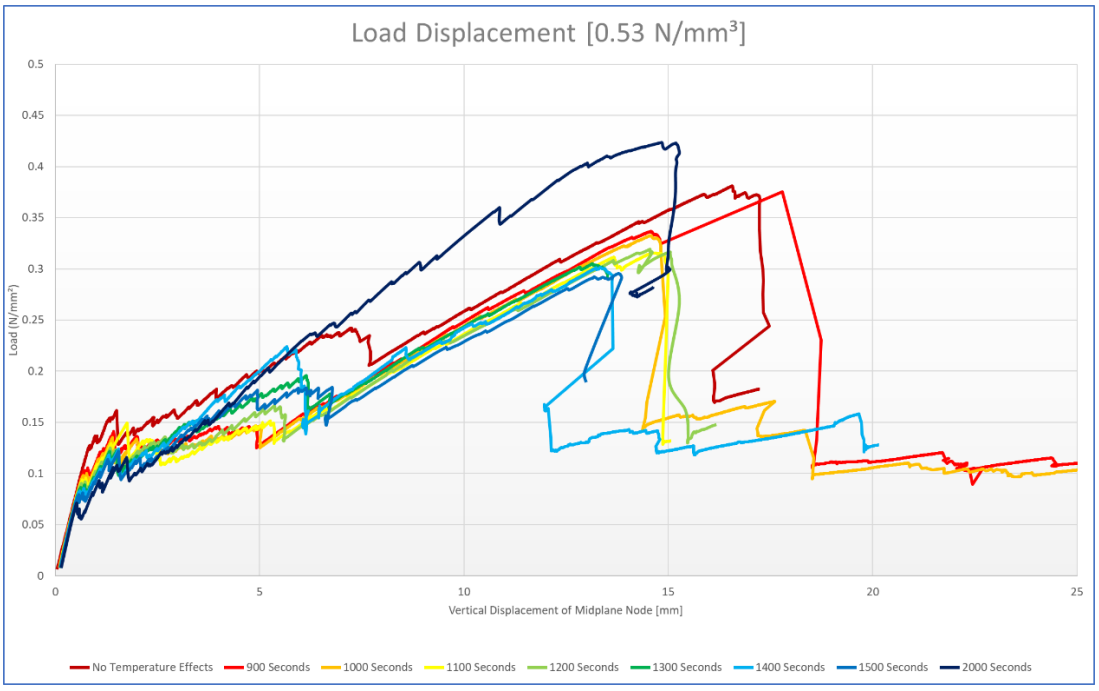

Figure 100: k=0.53 N/mm³ spring stiffness load displacement diagrams for different durations of fire exposure

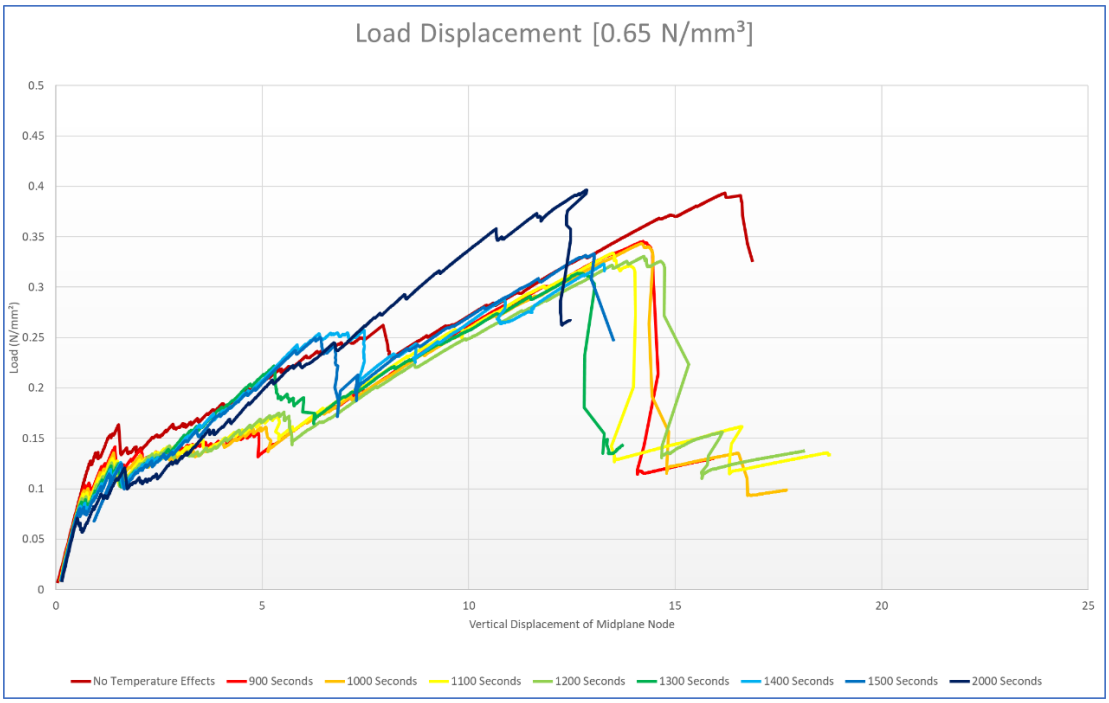

Figure 101: k=0.65 N/mm³ spring stiffness load displacement diagrams for different durations of fire exposure

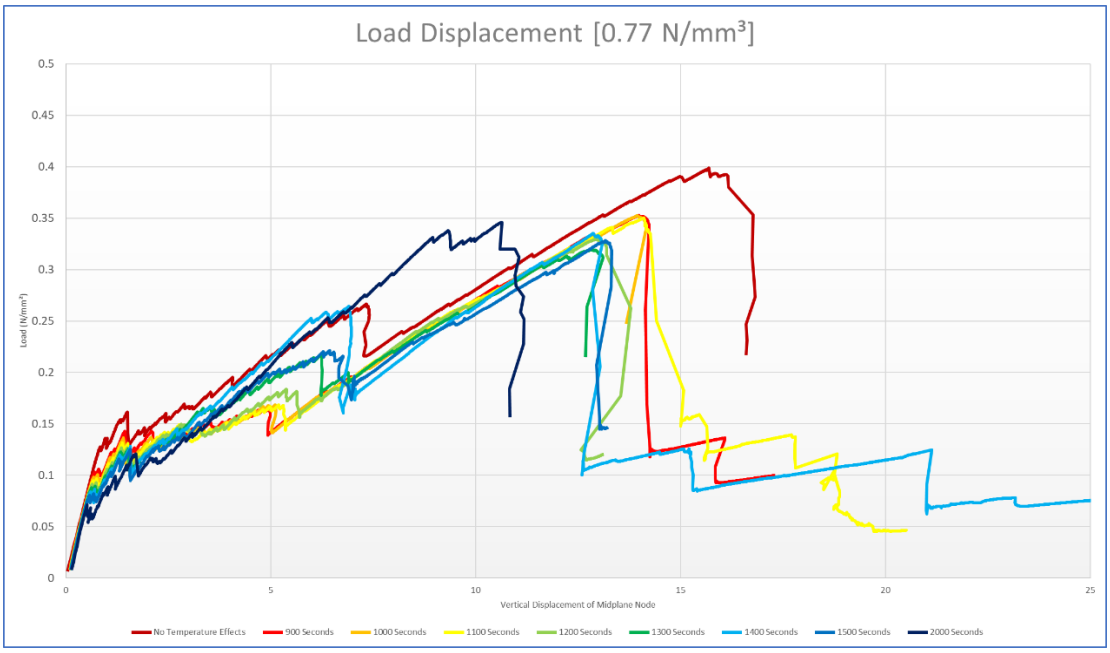

Figure 102: k=0.77 N/mm³ spring stiffness load displacement diagrams for different durations of fire exposure

12.7 Annex G: In-plane stresses

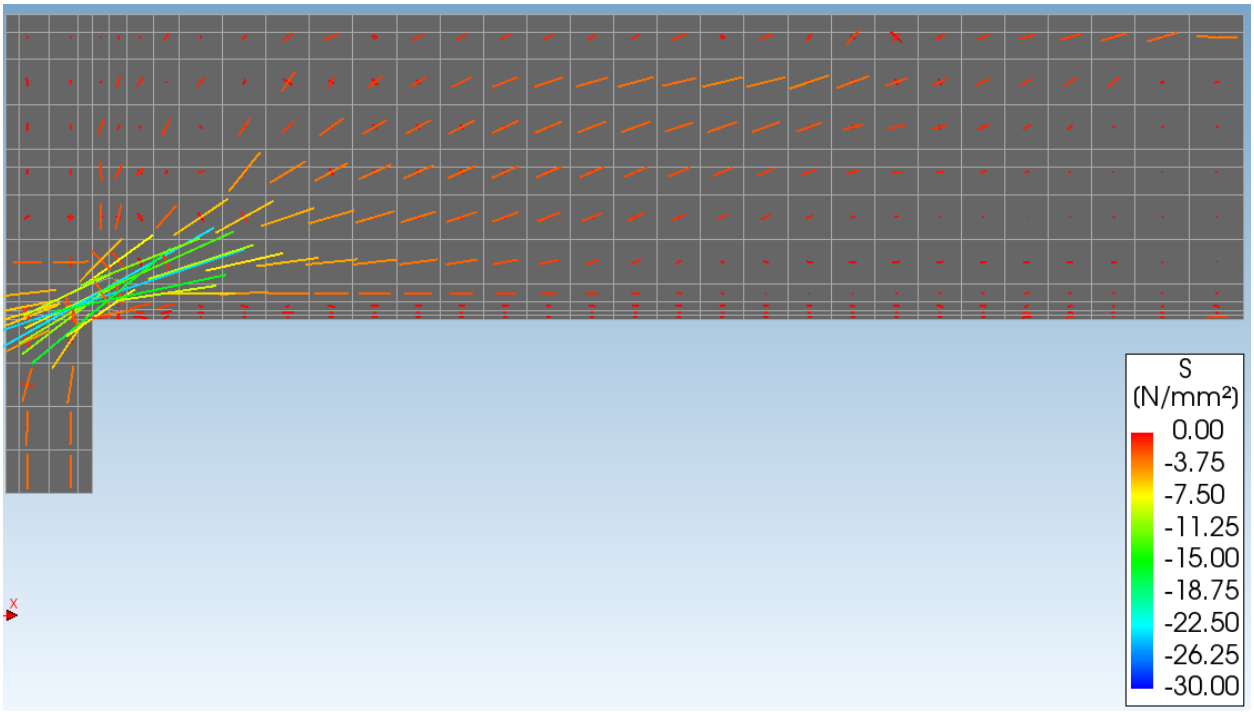

Figure 103: Analysis 2 in-plane stress components at peak loading

12.7.1 Sensitivity Study In-Plane Stress Diagrams at peak loading

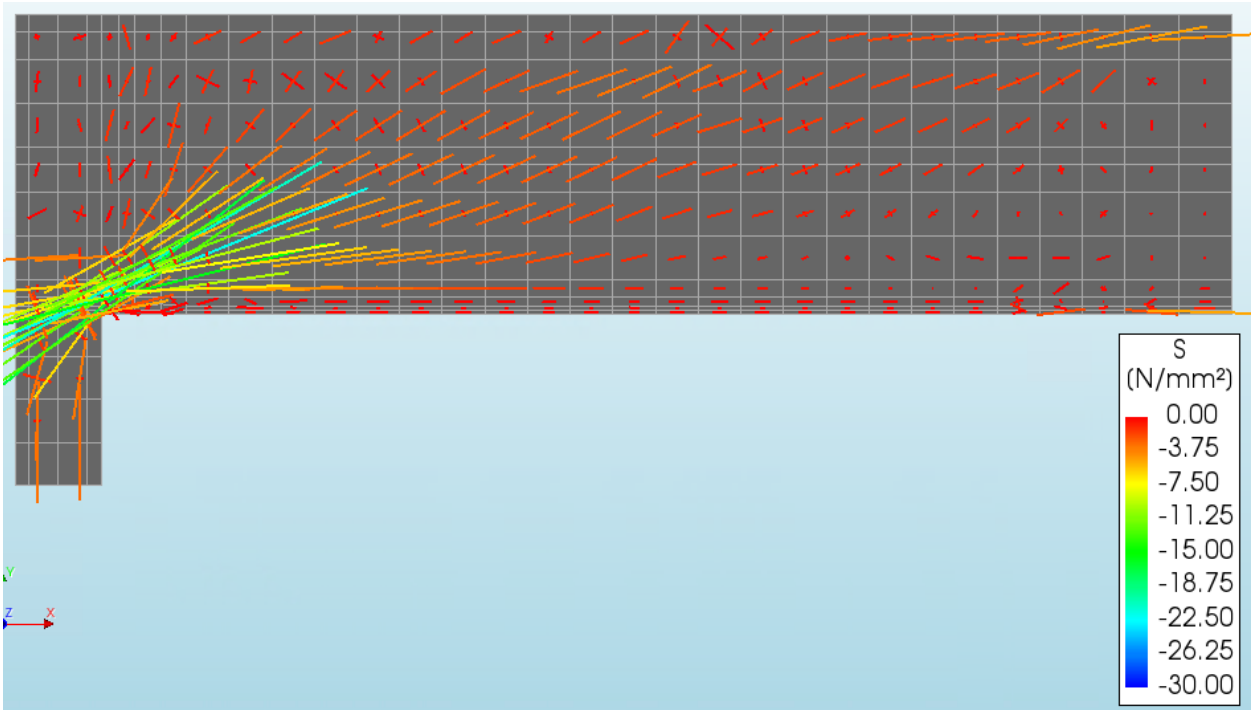

Figure 104: In plane stresses at peak stress for k=0.08 N/mm³

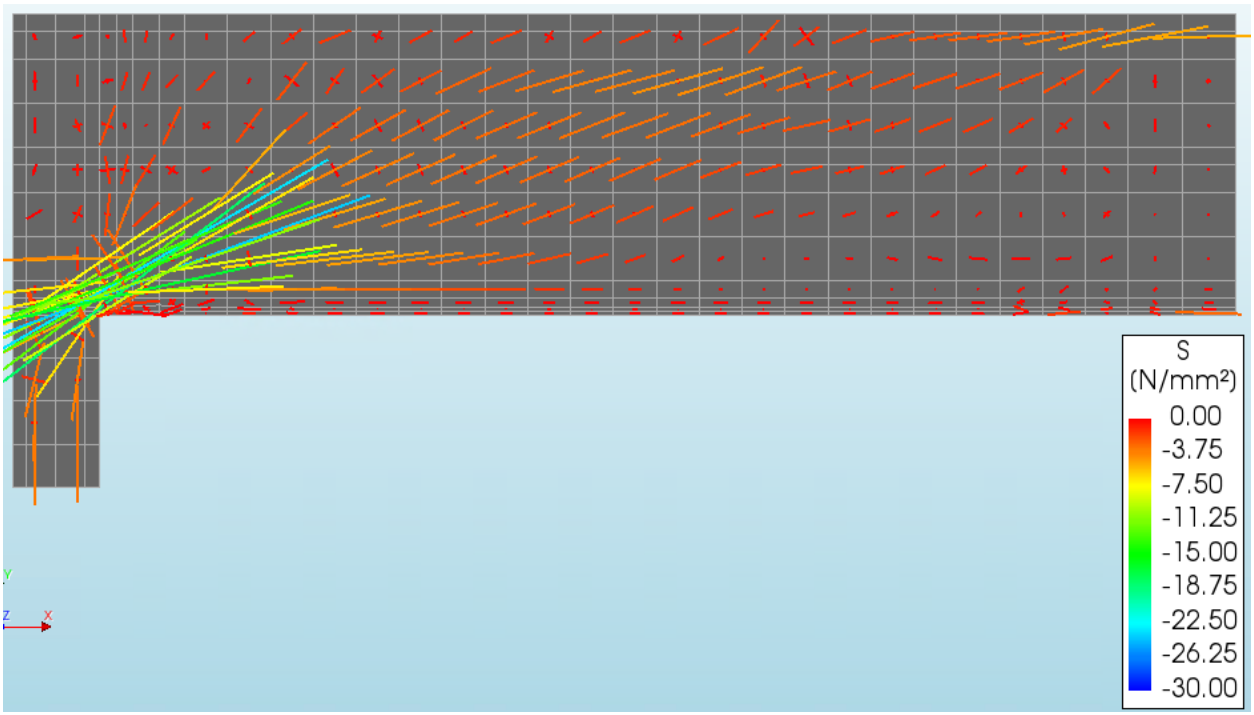

Figure 105: In plane stresses at peak stress for k=0.19 N/mm³

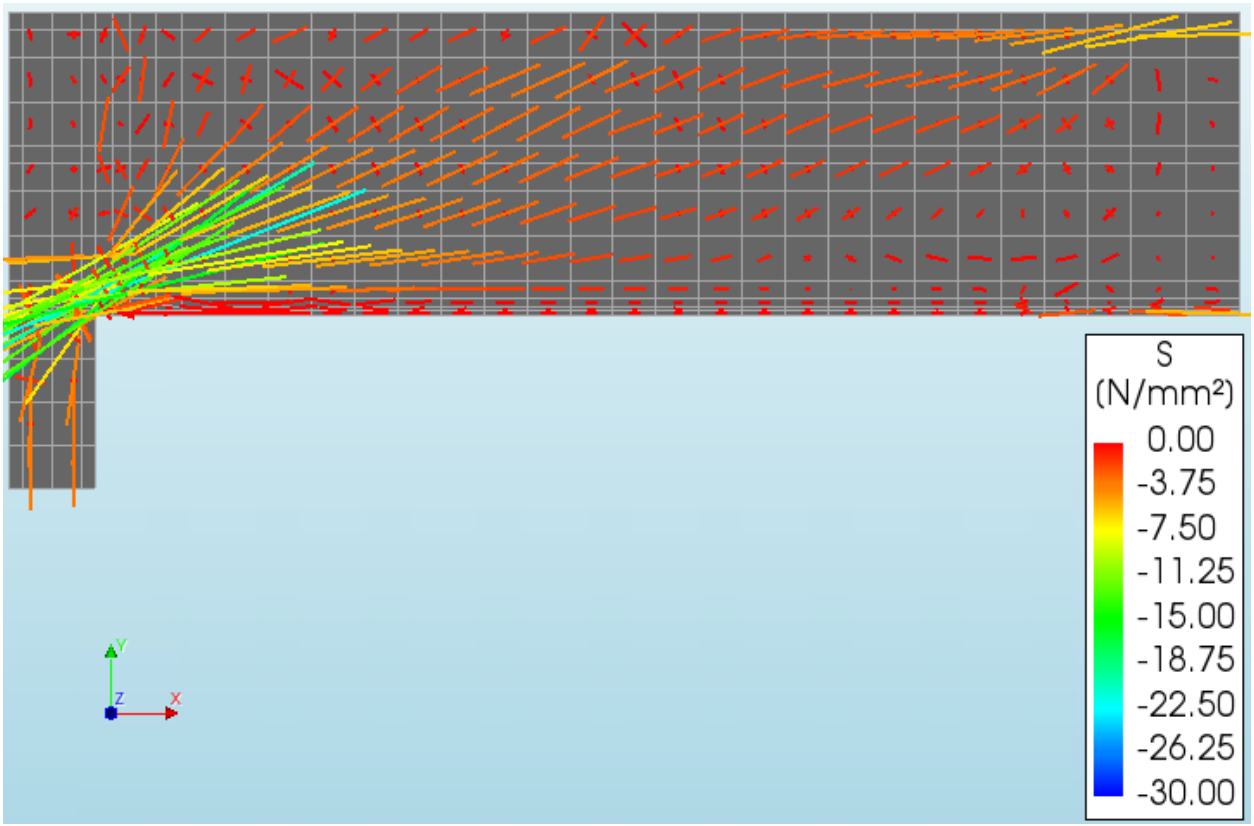

Figure 106: In plane stresses at peak stress for k=0.25 N/mm³

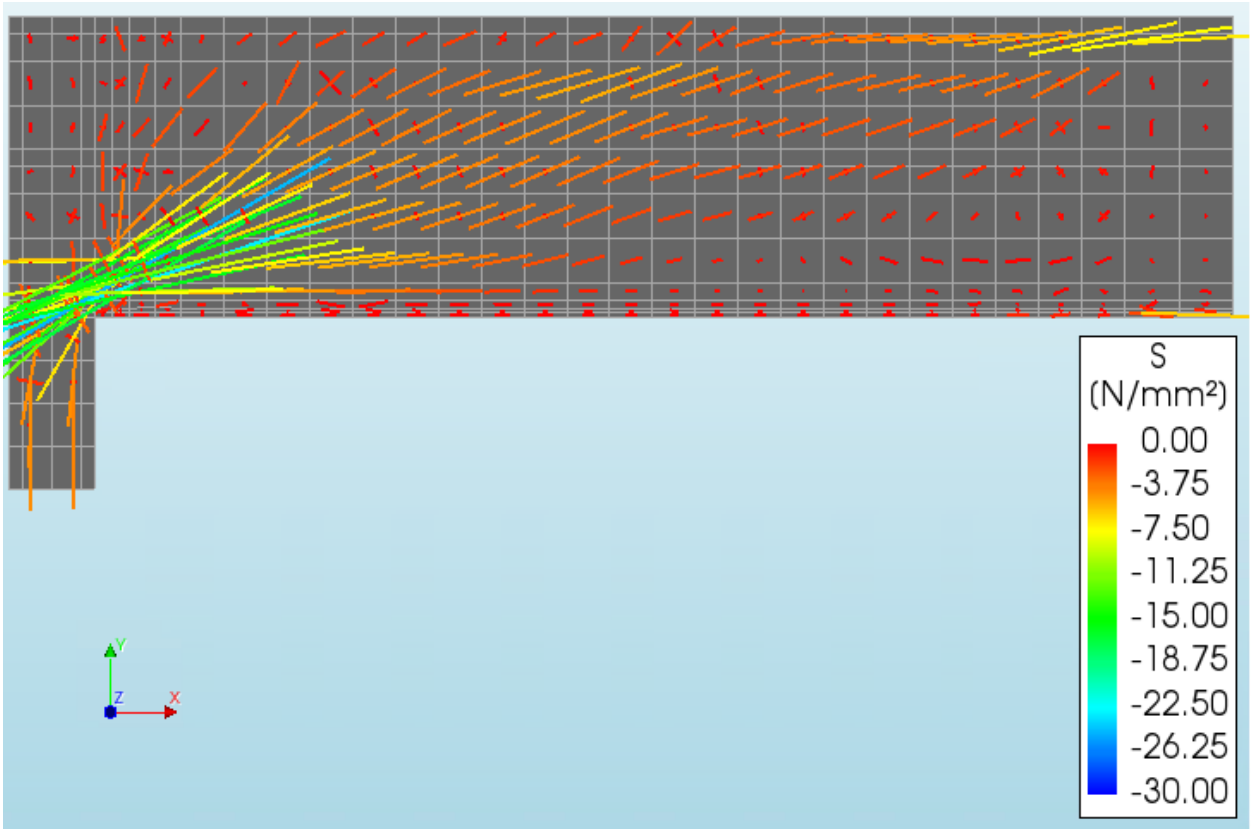

Figure 107: In plane stresses at peak stress for k=0.76 N/mm³

12.7.2 In Plane Stress Components with PSFC

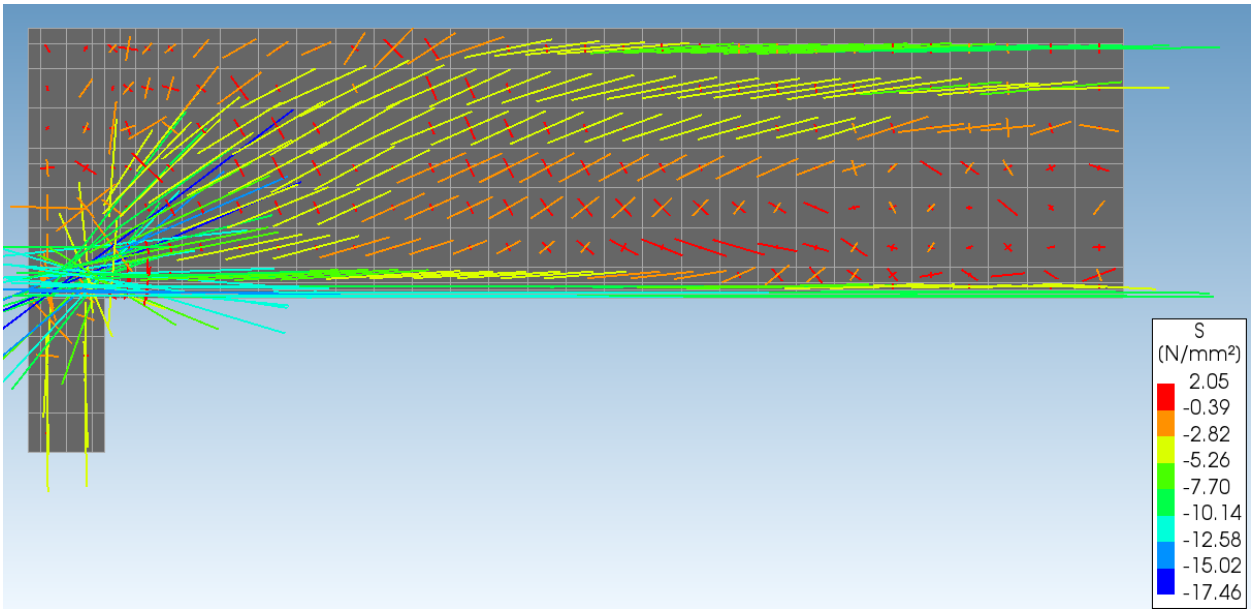

Figure 108: In-plane stress components of Analysis 1 after 2000 seconds

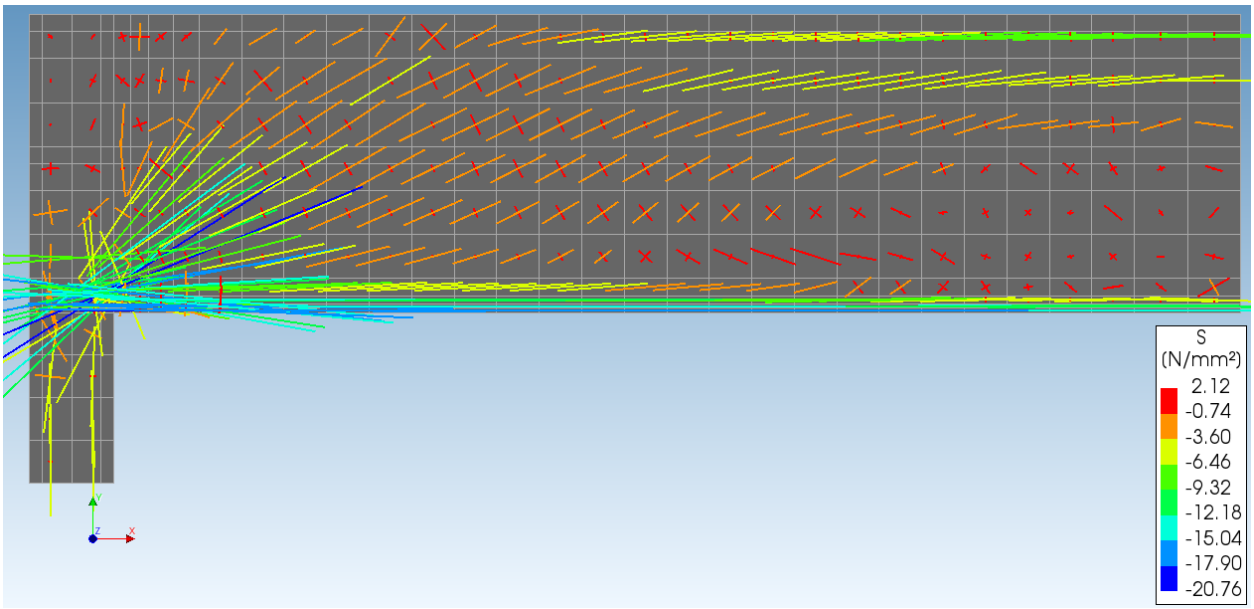

Figure 109: In-plane stress components of Analysis 3 after 2000 seconds

12.8 : Annex H: Thermal Dependency of Concrete

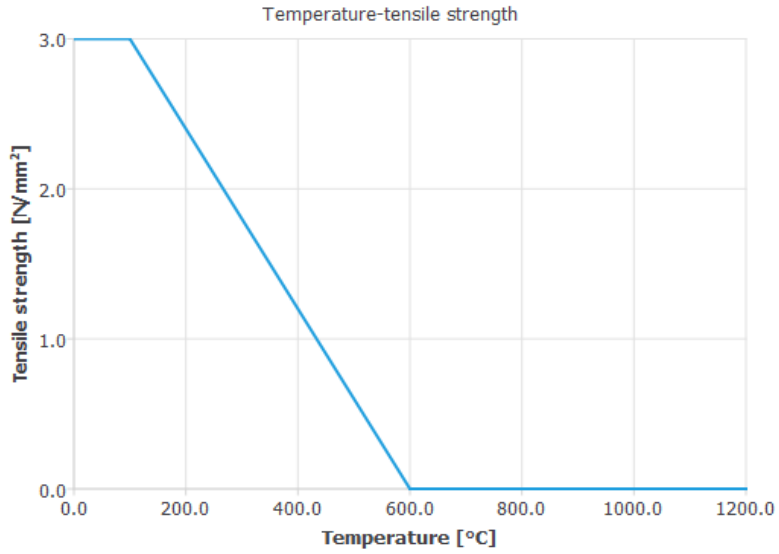

Figure 110: Concrete tensile strength as a function of temperature; NEN-EN-1992 1-2 Figure 3.2

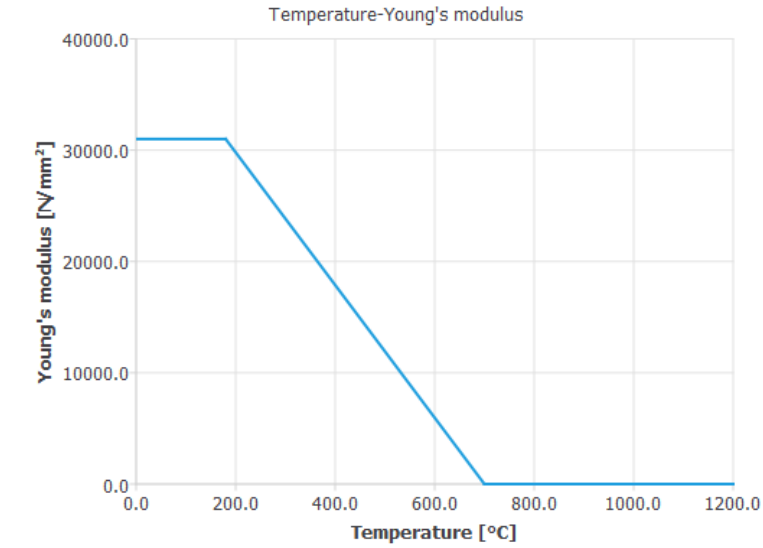

Figure 111:Modulus of elasticity as a function of temperature; NEN-EN-1992 1-2

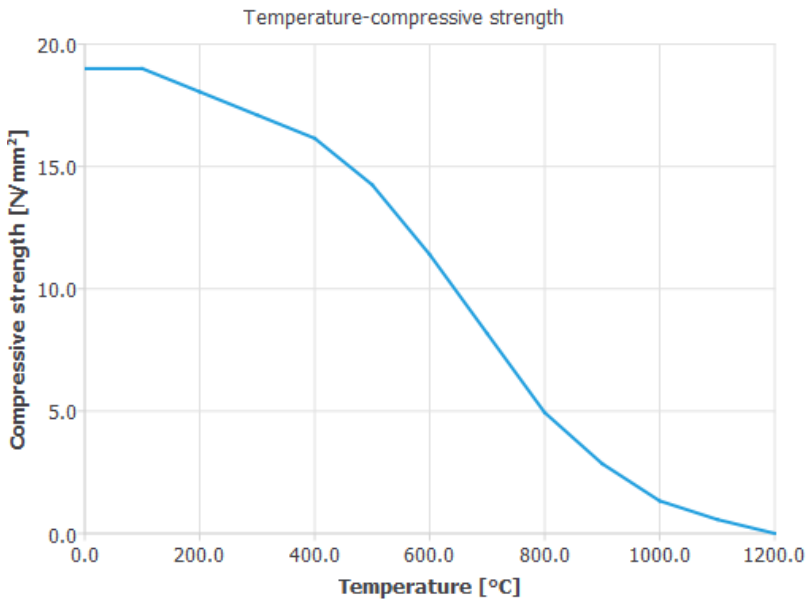

Figure 112:Concrete compressive strength as a function of temperature; NEN-EN-1992 1-2 Figure 4.1

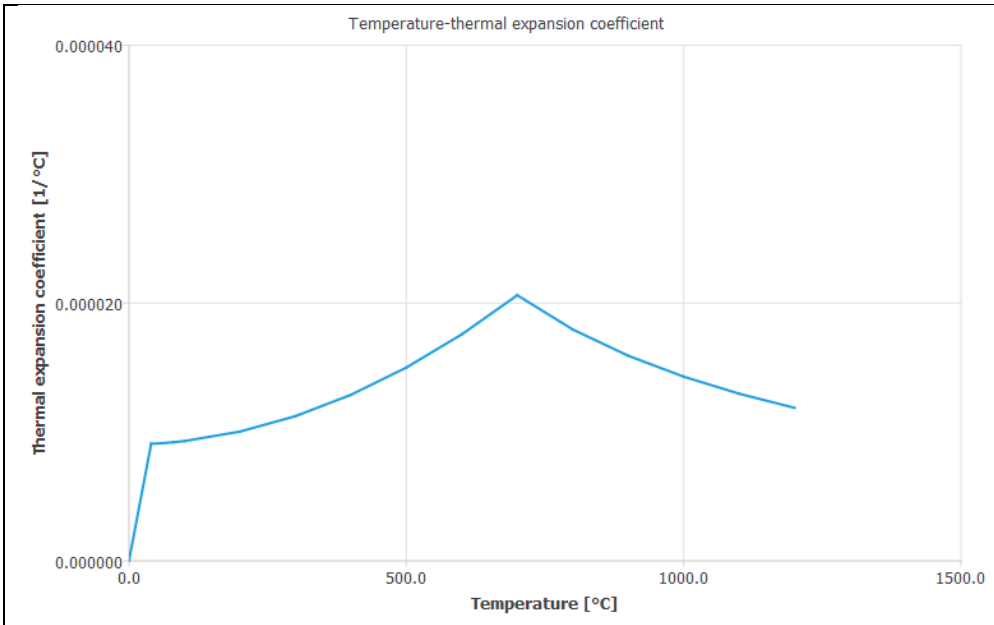

Figure 113: Thermal expansion coefficient as a function of temperature; NEN-EN-1992 1-2

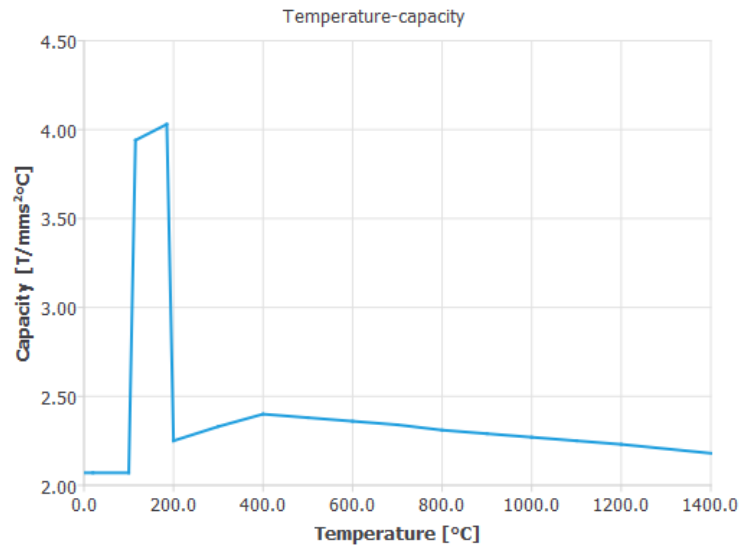

Figure 114: Specific heat capacity as governed by NEN-EN 1992 1-2 figure 3.6b

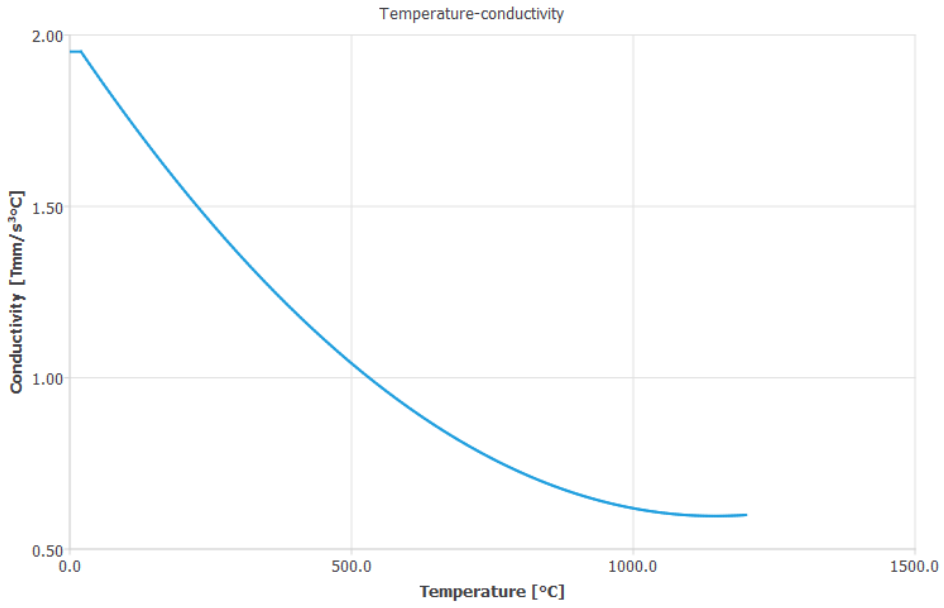

Figure 115: Temperature conductivity of concrete as a function of temperature as governed by the equation $\lambda_c = 2 - 0.2451 * \left(\frac{\theta}{100}\right) + 0.0107 * \left(\frac{\theta}{100}\right)^2 \ \frac{W}{m\,K} \ for\ 20°C \leq \theta \leq 1200°C$ *[NEN 1992-1-2]*

12.9 Annex I Temperature Calibration Curves

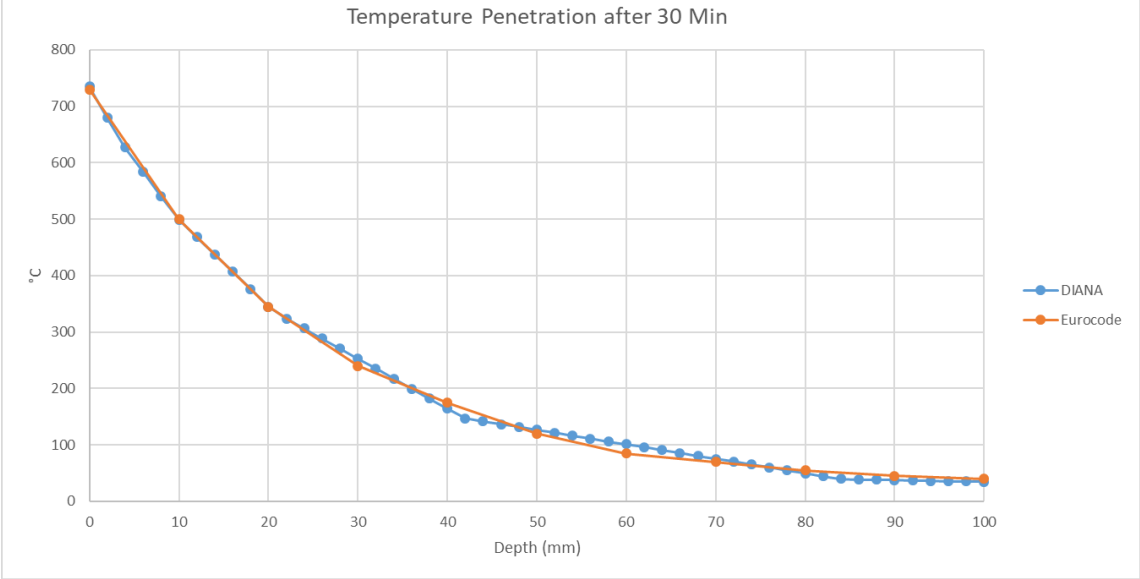

Figure 116: Temperature Penetration as a function of depth after 30 minutes of ISO 834 exposure

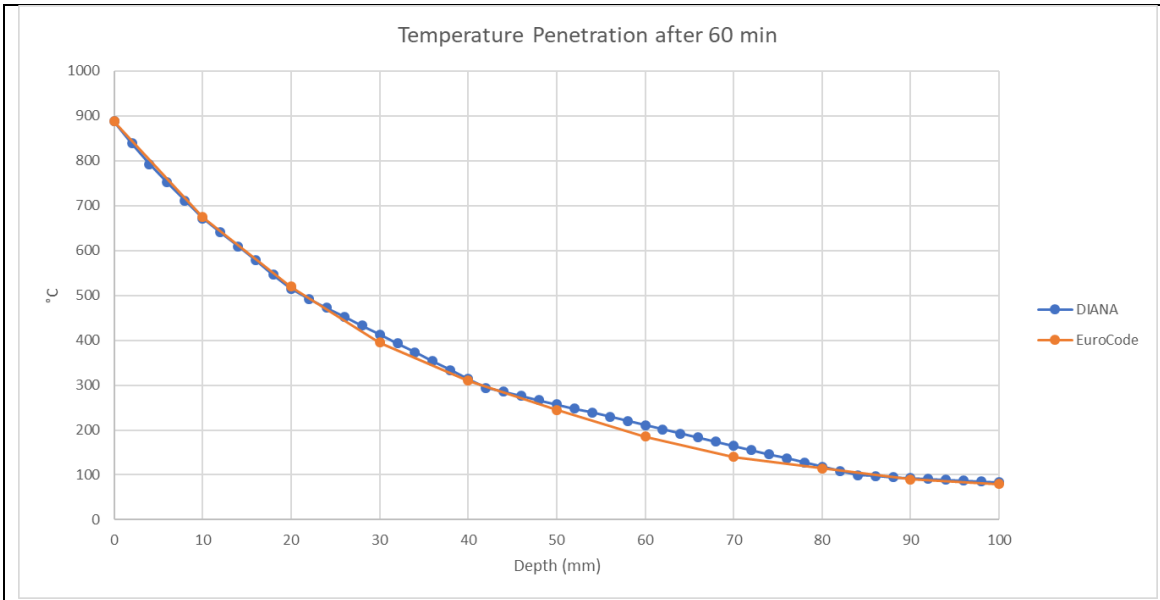

Figure 117: Temperature Penetration as a function of depth after 60 minutes of ISO 834 exposure

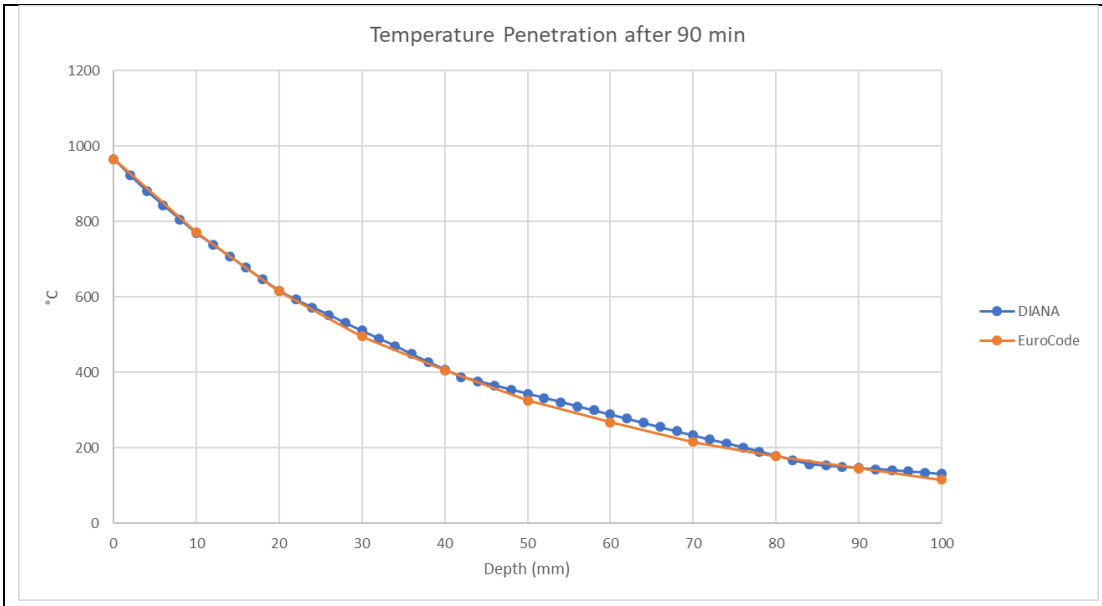

Figure 118: Temperature Penetration as a function of depth after 90 minutes of ISO 834 exposure

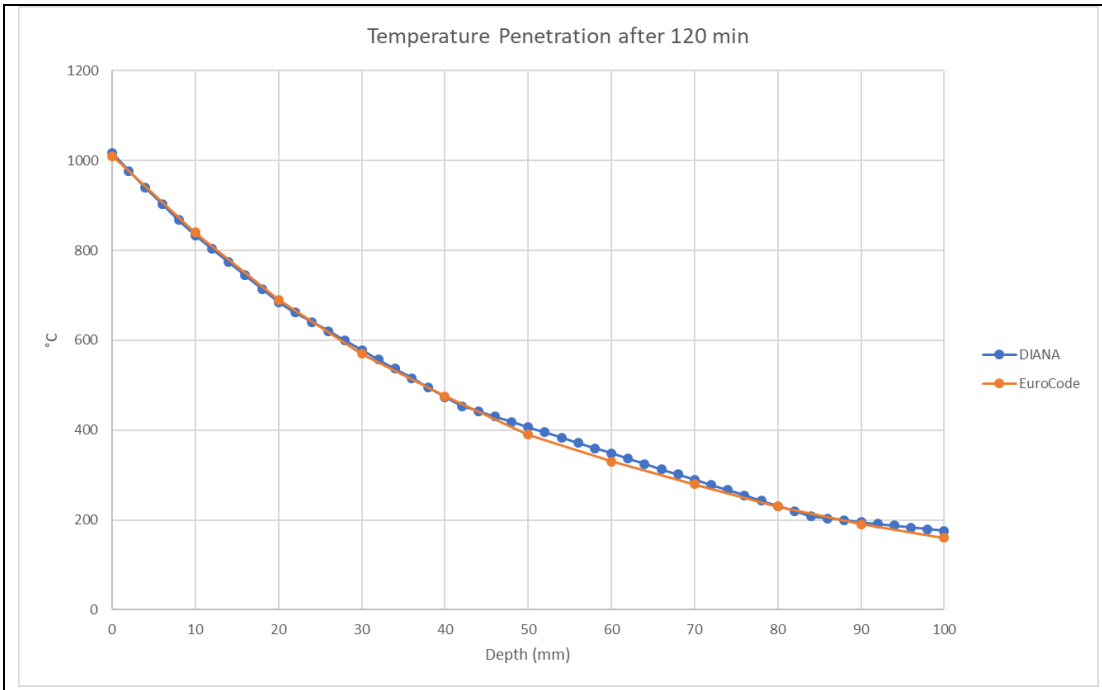

Figure 119: Temperature Penetration as a function of depth after 120 minutes of ISO 834 exposure

12.10 Annex J: ε_{c1} and ε_{cu} Values

Table 5: Temperature dependence of NEN 1992-1-2 compression curve

Temperature (°C)	ε_{c1}	ε_{cu}	f_c
20	0.0025	0.02	1
100	0.004	0.0225	1
200	0.0055	0.025	0.95
300	0.007	0.0275	0.85
400	0.01	0.03	0.75
500	0.015	0.0325	0.6
600	0.025	0.035	0.45
700	0.025	0.0375	0.3
800	0.025	0.04	0.15
900	0.025	0.0425	0.08
1000	0.025	0.045	0.04
1100	0.025	0.0475	0.01

Table 6: Linearly interpolated strain values based on calibration process

Temperature (°C)	ε_{c1}	ε_{cu}	f_c
0	0.0025	0.0085	1
100	0.0025	0.0111	1
200	0.0040	0.0145	0.95
300	0.0059	0.0178	0.85
400	0.0078	0.0211	0.75
500	0.0097	0.0244	0.6
600	0.0117	0.0277	0.45
700	0.0136	0.0310	0.3
800	0.0155	0.0343	0.15
900	0.0174	0.0376	0.08
1000	0.0193	0.0409	0.04
1100	0.0212	0.0442	0.01
1200	0.0231	0.0475	0

12.11 Annex K: Finite Element Calculation Specifications

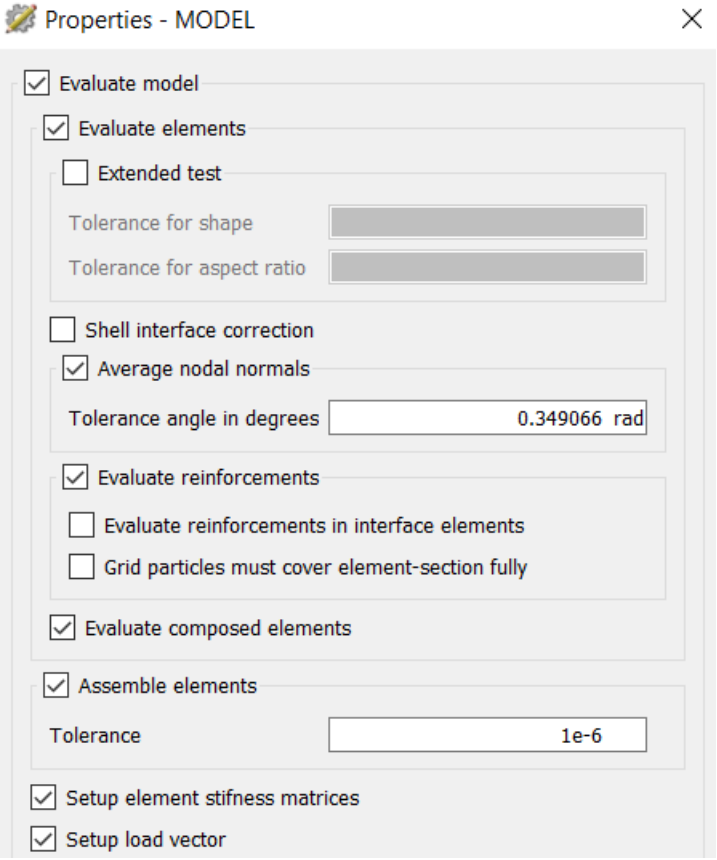

Figure 120: Modeling properties

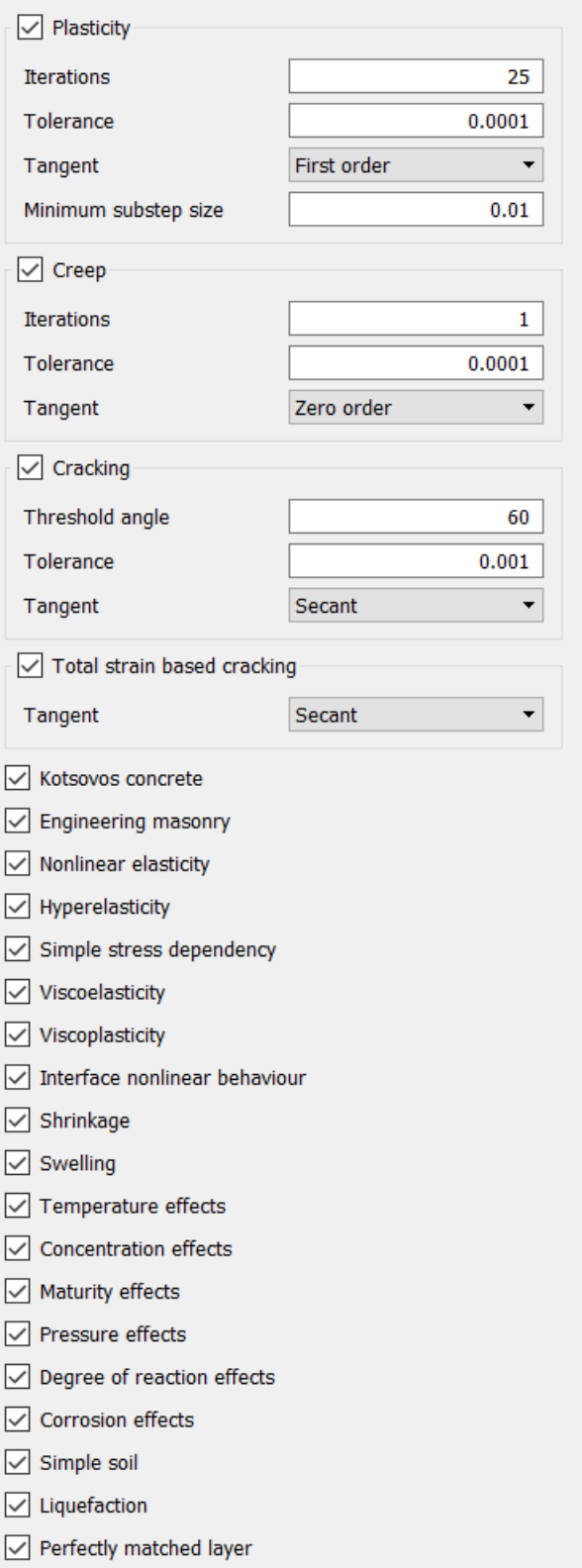

Figure 121: Physical Nonlinearity Settings

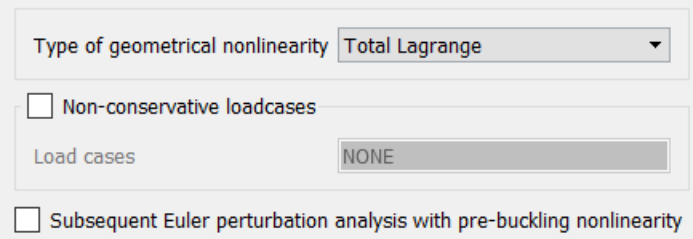

Figure 122: Geometrical Nonlinearity Settings

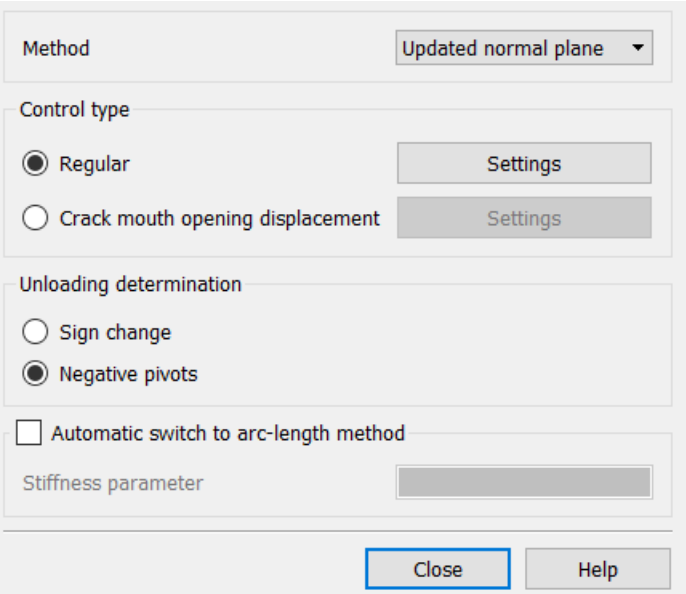

Figure 123: Arc Length Control Settings

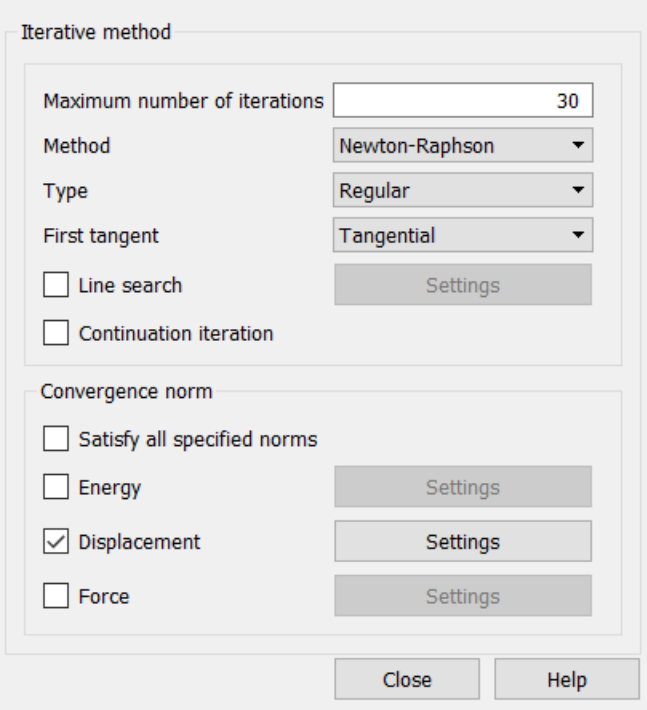

Figure 124: Iteration Procedure Specifications

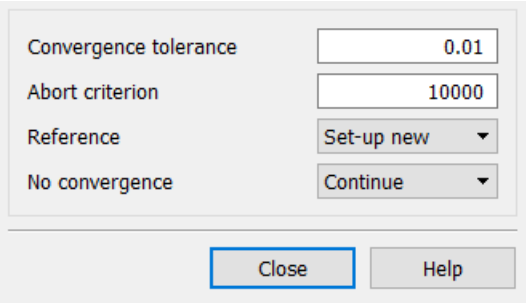

Figure 125: Displacement criterion specifications

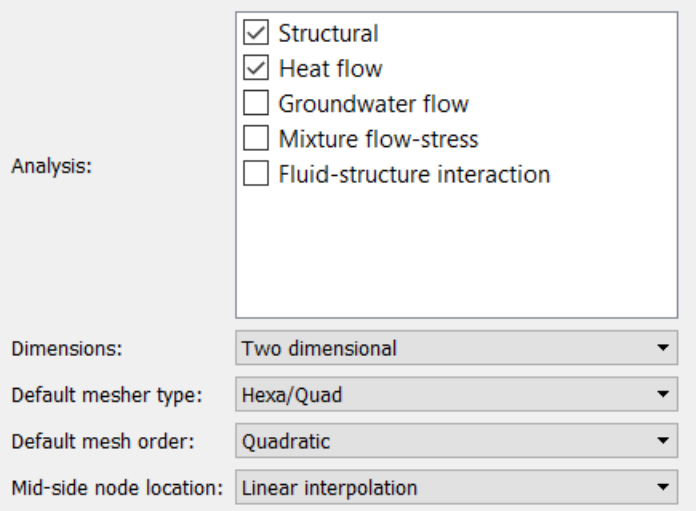

Figure 126: Project Specifications

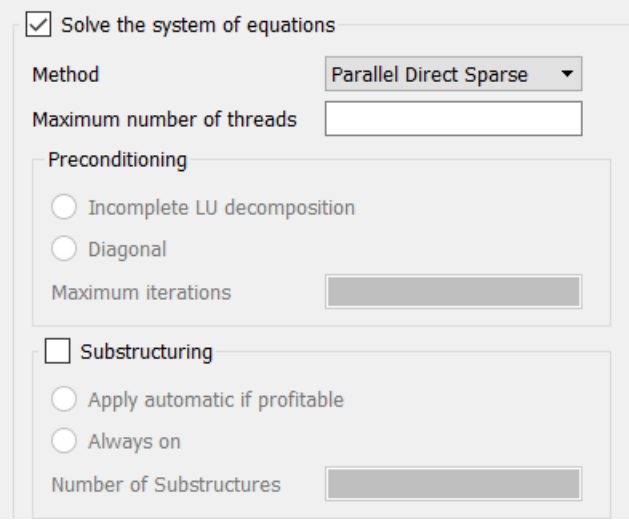

Figure 127: Solver specifications

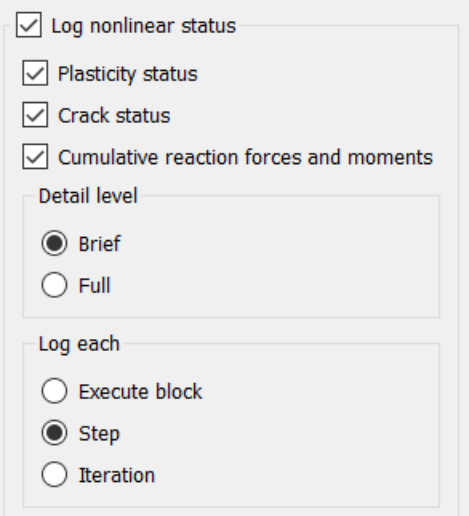

Figure 128: Logging Specifications

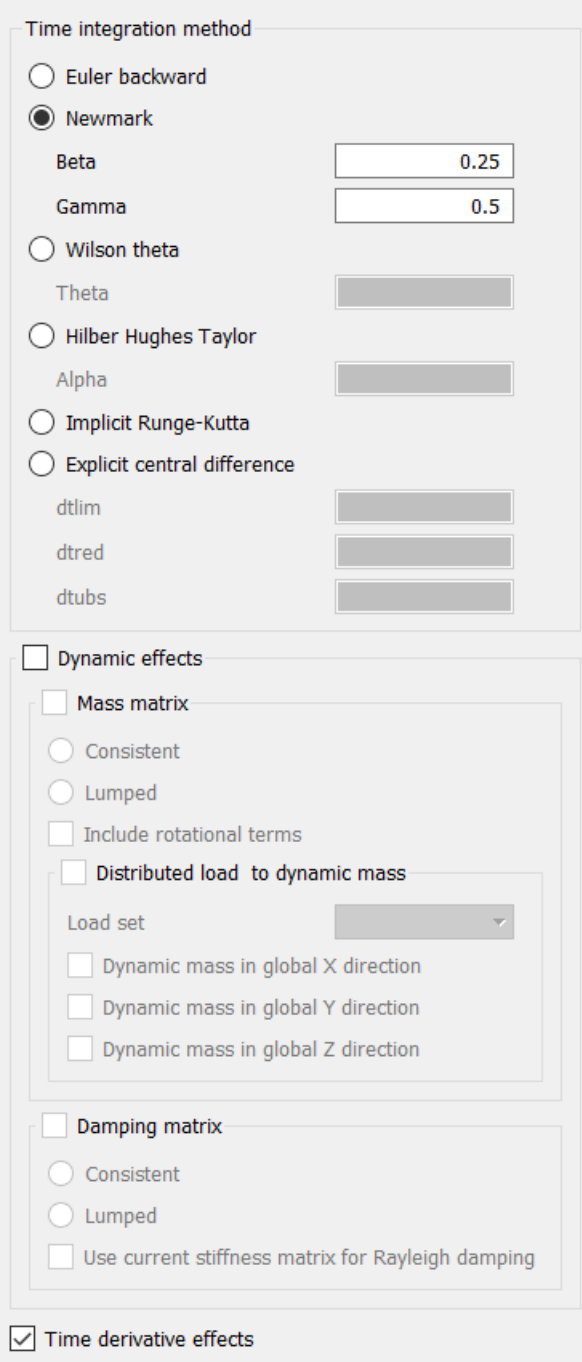

Figure 129: Transient Effects Settings

12.12 Annex L: Finite Element Specifications for Lateral Stiffness Study

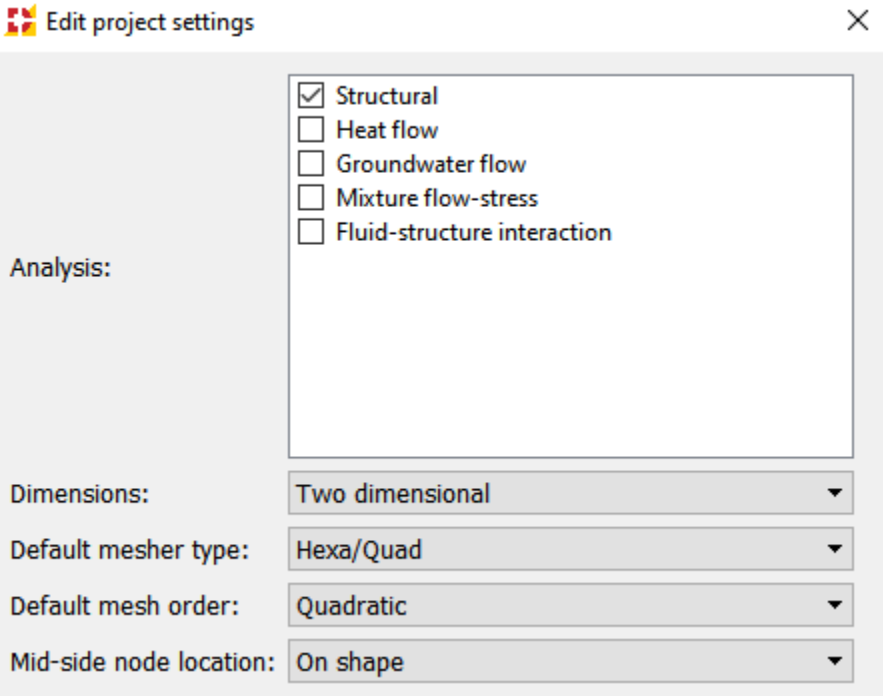

Figure 130: Project Settings

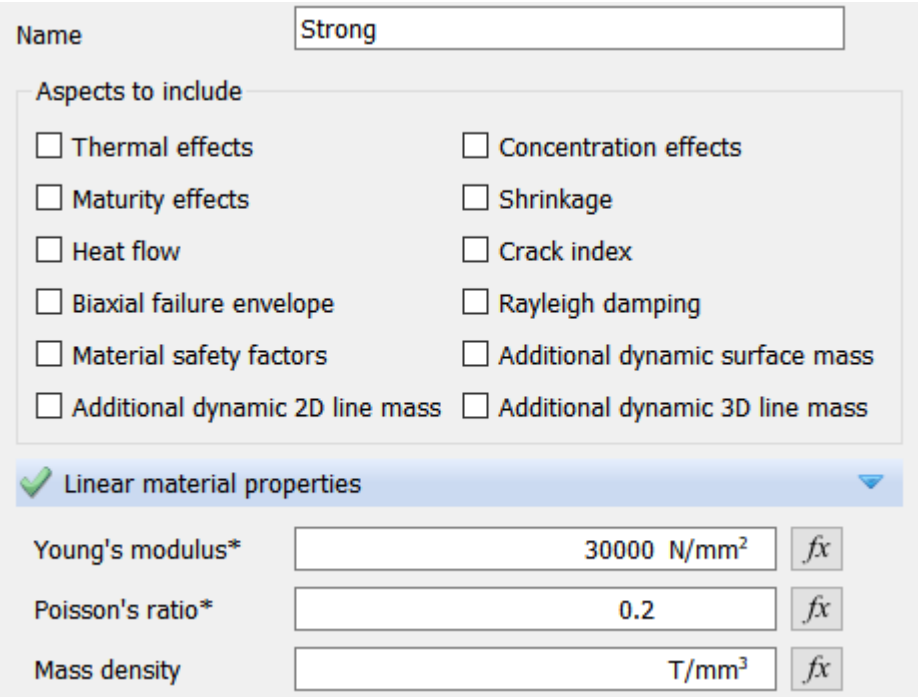

Figure 131: Material Properties of full strength concrete

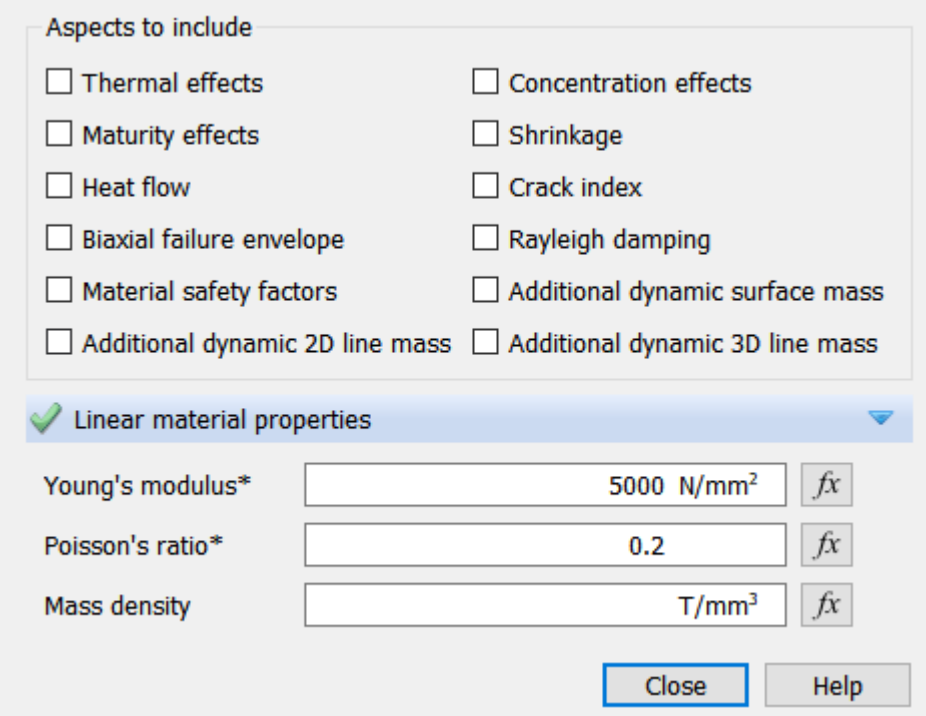

Figure 132: Material properties of cracked concrete

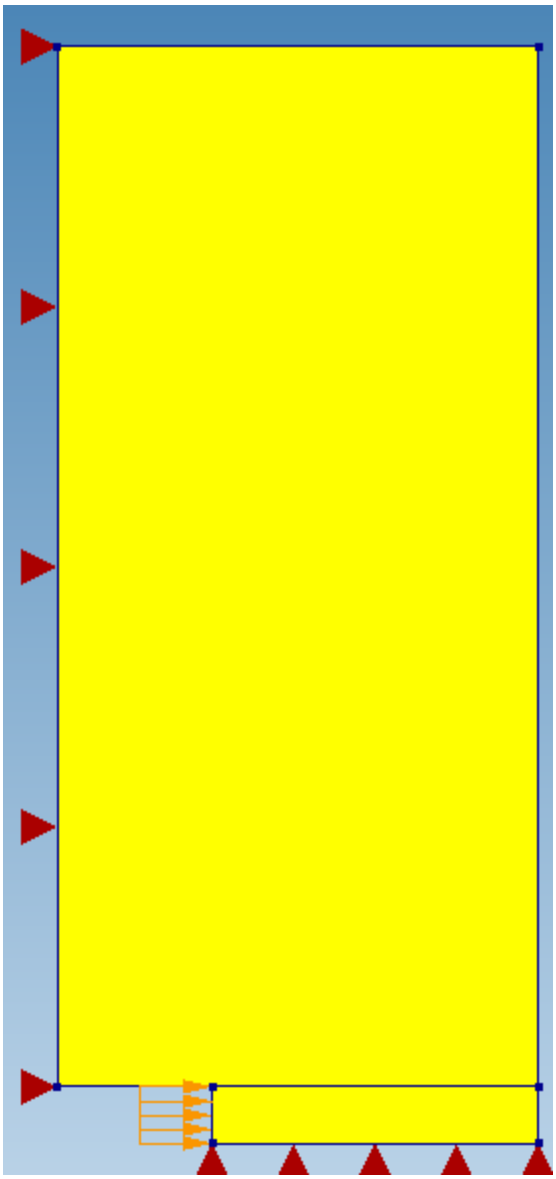

Figure 133: Boundary conditions

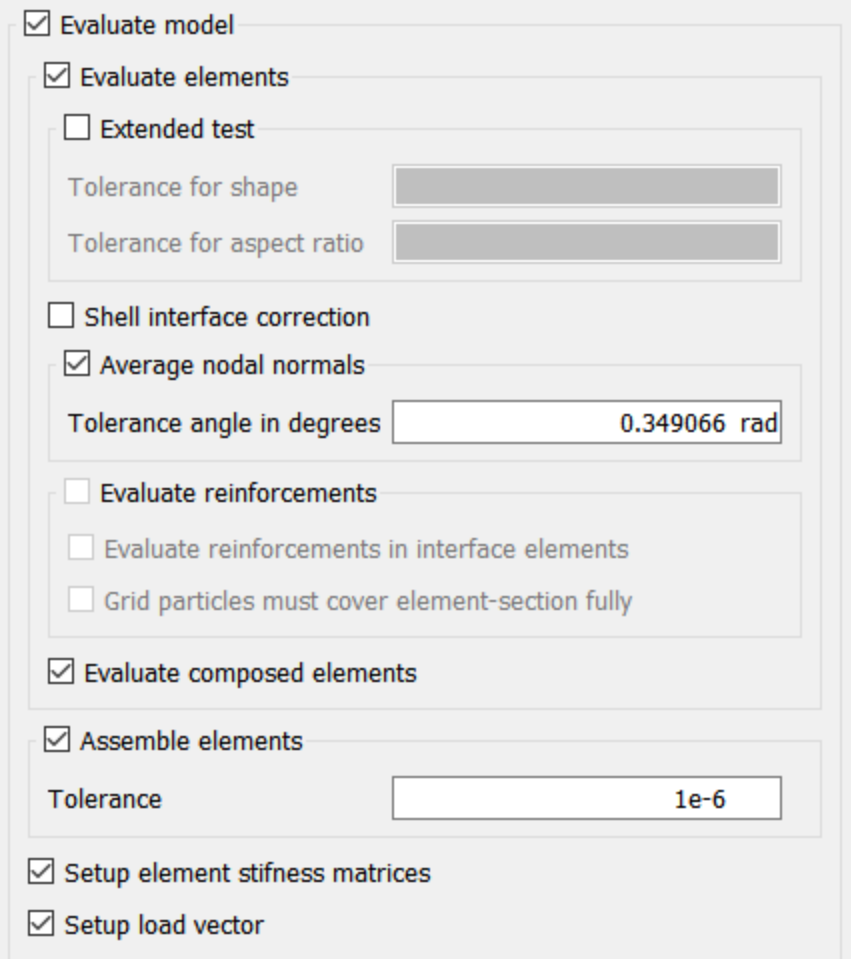

Figure 134: Model evaluation

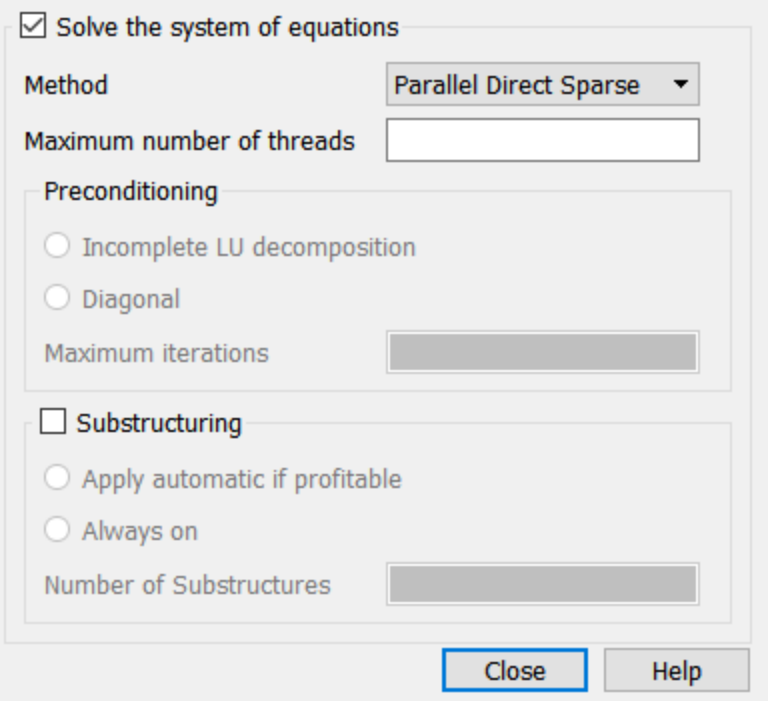

Figure 135: Solving specifications

13 Table of figures

14 Bibliography

1. **Ir. A.J. Breunese, Dr. Ir. C. Both, Ir. G.M. Wolsink (Rijkswaterstaat).** *Fire testing procedure for concrete tunnel linings.* 2008.

2. **Tim G. van der Waart van Gulik Arnoud J. Breunese Robert Jansson, Lars Boström, Emmanuel Annerel.** SPALLING BEHAVIOUR OF A NON-SPALLING QUALIFIED CONCRETE. Bleiswijk, The Netherlands : s.n., December 2014.

3. *Tunnels and Underground Cities. Engineering and Innovation Meet Archaeology, Architecture and Art:*. **Daniele Peila, Giulia Viggiani, Tarcisio Celestino.** Naples, Italy : s.n., 2019. Proceedings of the WTC 2019 ITA-AITES World Tunnel Congress (WTC 2019), May 3-9, 2019. p. 4470.

4. *Applications of Finite Element Analysis in Structural Engineering.* **Mahendran, M.** Chennai, India : s.n., 2007. International Conference on Computer Aided Engineering. pp. 38-46.

5. **Jansson, Robert.** Material properties related to fire spalling of concrete. s.l. : LTH, Lund University, 2008.

6. *Discussion on the article "The fire resistance of concrete beams" by Ashton and Bate.* **Z., Shorter G. W. & Harmathy T.** 1961. Proceedings, Institute of Civil Engineers Vol. 20. p. 313.

7. **Khoylou, N.** Modelling of moisture migration and spalling behaviour in non-uniformly heatedconcrete, PhD thesis. s.l. : University of London, 1997.

8. **Waubke., N.** Transportphänomene in Betonporen. s.l. : Technishe UniversitätBraunschweig, 1966.

9. **C. Both, TNO.** Brawat 3: onderzoek naar het afspatgedrag van een op druk belaste wand in afgezonken tunnels. *TNO-report 2001-CVB-R03264* . Delft, Zuid Holland, The Netherlands : s.n., May 10, 2001.

10. **Efectis.** *Leeswijzer brandproeven* . 2017.

11. *Arching Action In Reinforced Concrete Slabs.* **A. J. Ockleston, B.E., Ph.D., D.Sc.(Eng.), M.I.Struct.E., M.I.C.E.** 1958, The Structural Engineer, pp. 197-201.

12. **Amir, Sana.** Compressive Membrane Action in Prestressed Concrete Deck Slabs. *PhD Thesis.* s.l., Zuid Holland, The Netherlands : TU Delft Faculty of Civil Engineering and Geosciences, 2014.

13. **Coordinating National Wildfire Group.** *Glossary of Wildland Fire Terminology.* 2009.

14. **Ir. A.J. Breunese, Prof.dr.ir. J. Maljaars.** *Fire Safety Design CIE 5131.* Delft : TU Delft, 2015.

15. *Full-scale fire tests with a commuter train in a.* **Anders Lönnermark, Alexander Claesson, Johan Lindström, Ying Zhen Li, Mia Kumm, Haukur Ingason.** 2012, SP Technical Research Institute of Sweden.

16. **Y. Wang, Ian Burgess, František Wald, Martin Gillie.** *Performance-Based Fire Engineering of Structures.* s.l. : CRC Press, 2012.

17. **Richard Lunniss, Jonathan Baber.** *Immersed Tunnels.* Boca Raton : CRC Press, 2013.

18. —. *Immersed Tunnels.* Boca Raton : Taylor & Francis Group, LLC, 2013.

19. *How do polypropylene fibers improve the spalling behavior of in-situ concrete?* **Matthias Zeiml, David Leithner, Roman Lackner, Herbert A. Mang.** s.l. : Cement and Concrete Research, May 2006, Institute for Mechanics of Materials and Structures.

20. *Controlling Concrete Degradation.* **Dhir, Ravindra and Moray, Newlands.** 1999.

21. **Hendriks, M.A.N., A., de Boer and Belletti, B.** *Guidelines for Nonlinear Finite Element Analysis of Concrete Structures.* RTD:1016-1:2017. s.l. : Rijkswaterstaat Centre for Infrastructure, 2017.

22. *Residual stress–strain relationship for concrete after.* **Chang, Y.F, et al.** 10, Pergamon : Cement and Concrete Research, 2006, Vol. 36. 0008-8846.

23. **DIANA FEA BV.** DIANA – Finite Element Analysis Release Notes release 10.3. *DIANA.* Delft : s.n., 2019.

24. **Mier, van, J. G. M.** *Strain-softening of concrete under multiaxial loading.* Eindhoven : Technische Hogeschool Eindhoven, 1984. pp. 109-113, PhD Thesis.

25. **Long, Adrian E and Rankin, Barry.** *Arching action strength enhancement in laterally-restrained slab strips.* s.l. : Structures and Buildings, 1997.

26. *Brandbeständigkeit von Faser-, Stahl- und Spannbeton.* **Kusterle, Prof. Dipl.-Ing. Dr.Wolfgang.** 2004, Straßenforschungsauftrag Nr. 3.269 des Bundesministeriums für Verkehr, Innovation und Technologie.

27. **William L. Gamble, Robert Park.** *Reinforced Concrete Slabs.* s.l. : John Wiley & Sons, 1999.

28. **Civieltechnisch Centrum Uitvoering Research en Regelgeving (CUR).** *CUR 166: Damwandconstructies - deel 1 (richtlijn).* 2008.

29. **BRAAM, et al.** *Concrete Structures under Temperature and Shrinkage Deformations - Theory and Practice.* Delft : s.n., 1994.

30. **NEN-EN 1992-1-1.** Delft : s.n., 2006.

31. **European Committee for Standardization.** NEN 1992-1-2. *Eurocode 2: Ontwerp en berekening van betonconstructies - Deel 1-2: Algemene regels - Ontwerp en berekening van constructies bij brand.* p. 64.

32. *Shortcrete: More Engineering Developments.* **Bernard, Erik Stephan, [ed.].** 2004.

33. **Ir. AJ. Breunese, Dr. Ir. C. Both, Ir. G.M. Wolsink.** *Fire testing procedure for concrete tunnel linings.* 2008.